EVALUATING DIAGNOSTIC LOSS IN COMPRESSED MEDICAL IMAGES USING COMPUTER SIMULATION

by

ALPASLAN KOÇ

B.S., Physics, Boğaziçi, 2006

Submitted to the Institute of Biomedical Engineering
in partial fulfillment of the requirements
for the degree of
Master of Science
in
Biomedical Science

Boğaziçi University
September 2009

EVALUATING DIAGNOSTIC LOSS IN COMPRESSED MEDICAL IMAGES USING COMPUTER SIMULATION

APPROVED BY:

Assoc. Prof. Albert Güveniş .....
(Thesis Advisor)

Prof. Yekta Ülgen .....

Doç. Dr. Mahmut Ekşioğlu .....

DATE OF APPROVAL: 15.09.2009

ACKNOWLEDGMENTS

I would like to thank my thesis supervisor Assoc. Prof. Albert Güveniş. Without his patience, encouragement and guidance, I would not been able to finish this thesis. I would also like to thank the rest of my thesis committee - Prof. Yekta Ülgen, and Doç. Dr. Mahmut Ekşioğlu - for their precious time and valuable suggestions.

Most importantly, I thank my parents and my brother and sister for their unconditioned love and support. Without them, I would never have the chance to fulfill my dream. This study is dedicated to them.

ABSTRACT

EVALUATING DIAGNOSTIC LOSS IN COMPRESSED MEDICAL IMAGES USING COMPUTER SIMULATION

The objective of this thesis is to evaluate the diagnostic loss in compressed medical images using computer simulation. Compressing medical images is a necessity due to the cost of the storage medium as well as the low bandwidth available for telemedicine procedures.

Experimental studies conducted conventionally for this purpose use a set of real images for which a consensus is reached by a team of medical imaging specialists, on the presence or absence of a lesion. Then ROC (Receiver Operating Characteristic) curve analysis is carried out in order to determine the effect of compression at different ratios in terms of lesion detectability. The area under the curve (AUC) equals one when lesions can be detected perfectly well. If they can not be detected the area under the curve (AUC) equals 0.5 and this means that it is not better than arbitrary guessing. These experiments should be conducted by using many images and observers if it will be statistically significant. Therefore it is time consuming and expensive. Furthermore, this method has serious drawbacks since it does not include any analysis for small subtle lesions and is impossible to compare the errors due to other factors such as variation in equipment and data acquisition protocols.

This thesis has the objective of eliminating these drawbacks by using a computer simulation of the entire imaging chain that includes the organ, the imaging equipment and the human observer. A Monte Carlo simulation package (SIMIND) has been used to simulate the image formation process for a gamma camera acquiring data from a breast containing a lesion. The obtained images are then compressed using the JPEG and JPEG 2000 algorithms at different compression ratios. Lesion detectability is then

assessed by using a mathematical observer model named the channelized hotelling observer. Image quality is also assessed using quantitative image quality metrics.

The results showed that diagnostic loss occurs at all compression ratios for subtle lesions but this loss may be comparable to other losses such as the ones due to variation in equipment and data acquisition protocols. Eventually, the decision of which compression rate to adopt will not be different than any other engineering tradeoff decision made for balancing cost and performance. This is in contrast with experimental studies that determine the ideal compression ratio based on evident lesions only and therefore presents an alternative methodology.

Keywords: Breast Scintigraphy, Monte Carlo Simulation, Lossy Compression, Image Quality Metrics, Model Observer.

ÖZET

SIKIŞTIRILMIŞ TIBBİ GÖRÜNTÜLERDE BİLGİSAYAR SİMÜLASYONU KULLANARAK DİYAGNOSTİK KAYBIN HESAPLANMASI

Bellek kapasitesinin yanında teletıp merkezlerinin sahip olduğu düşük bant-genişliği medikal görüntülerin sıkıştırılmasını gerekli kılmaktadır. Bu çalışmanın hedefi sıkıştırılmış medikal medikal görüntülerdeki diyagnostik kaybın bilgisayar simülasyonu kullanarak hesaplamaktır.

Bu amaç için yapılan geleneksel çalışmalar, medikal görüntüleme uzman gruplarının lezyonun varlığı yada yokluğu hakkında görüş birliğine vardığı bir takım gerçek görüntüler kullanmaktadır. Daha sonra lezyonun farkedilebilirliği bakımından değişik oranlarda sıkıştırmanın etkisini belirlemek için ROC (Receiver Operating Characteristic) eğri analizleri uygulanmaktadır. Lezyonlar tamamiyle farkedilebiliyorsa eğrinin altında kalan alan (AUC) 1'e eşit olmaktadır. Lezyonun farkedilememesi sıradan bir tahminden daha iyi değildir ve eğrinin altında kalan alan (AUC) 0.5'e eşit olmaktadır. Bu çalışmalar istatiksel olarak geçerli olacaksa, çok sayıda görüntü ve gözlemci kullanılarak uygulanmalıdır. Bu nedenle bu oldukça fazla zaman alan ve masraflı bir metottur. Ayrıca bu metotun ciddi sakıncaları vardır. Çünkü küçük ve zor görünen lezyonlar için hiçbir inceleme içermiyor ve bu metotla cihazdaki ve bilgi işleme protokolündeki değişiklikler gibi diğer faktörlerden oluşan hataları karşılaştırmak mümkün değil.

Bu tezin amacı, bütün görüntüleme zincirinin içerdiği organ, görüntüleme cihazı ve gözlemciyi simüle ederek bu dezavantajları ortadan kaldırmaktır. Lezyon içeren memeden bilgi sağlayan gamma kamera için görüntü oluşturma işlemini simüle etmede Monte Carlo simülasyon paketi olan SIMIND kullanıldı. Elde edilen görüntüler sonra JPEG ve JPEG 2000 algoritmaları kullanılarak farklı oranlarda sıkıştırıldı. Matematiksel gözlem modeli olan Channelized Hotelling Observer (CHO) kullanılarak lezyon farkedilebilirliği incelendi. Ayrıca görüntü niteliği sayısal nitelik ölçevi kullanılarak

değerlendirildi.

Sonuçlar zor görünen lezyonlar için diyagnostik kaybın her sıkıştırma oranında olduğunu gösteriyor fakat bu kayıp cihazdaki ve bilgi işleme protokolündeki değişiklikler gibi diğer faktörlerden oluşan kayıplarla karşılaştırılabilmektedir. Neticede hangi sıkıştırma oranının kullanılacağı kararı maliyet ve performans dengesi için verilen herhangi bir mühendislik mübadele kararından farklı değildir. Bu sadece belirgin lezyonları kullanarak ideal sıkıştırma oranını belirleyen deneysel çalışmalara zıttır ve bu nedenle alternatif bir yöntem sunmaktadır.

Anahtar Sözcükler: Meme Sintigrafisi, Monte Carlo Simülasyon, Kayıplı Sıkıştırma, Imaj Nitelik Ölçevi, Model Observer

TABLE OF CONTENTS

LIST OF FIGURES

LIST OF TABLES

LIST OF SYMBOLS

$x_{interaction}$	x coordinate of the interaction side
σ	Statistical variations of the counts
N	Count number
R_e	Spatial resolution
d	Hole diameter
L	Hole length
z	Source to collimator distance
S	Total plane source sensitivity
ε	Efficiency of a monte carlo calculation
T	Calculation time
F(x)	Cumulative distribution function
f(x)	Frequency function
$F^{-1}(x)$	Inverse of the cumulative distribution function
R	Uniform random number
$f'(x)$	normalized function
f(x,y)	original image data
$f^*(x,y)$	Compressed image data
dB	decibel
bpp	bit per pixel
H_1	image with lesion
H_0	image without lesion
f	Normal, non-lesion portion of the anatomy
t	signal
n	noise
H	Operator that describes imaging system
g	Noisy image data
λ	Scalar test statistic
w	Hotelling template

$\mathbf{K}$	Data covariance matrix
$\langle g \rangle_1$	Mean signal present data vector
$\langle g \rangle_0$	Mean signal absent data vector
ν_n	Output of the nth channel
U_n	nth template
$\mathbf{w}_c$	Channelized hotelling template
$\mathbf{K}_c$	Covariance matrix of the channel output
$\mathbf{s}_c$	Signal seen through the channels
λ_c	Channelized hotelling test statistic
SNR_{λ_c}	Signal to noise ratio of the channelized hotelling test statistic
erf(.)	error function
Ci	Curie
$\mathrm{LG}_n(r)$	The nth order Laguerre-Gauss function
a	Width parameter of the Laguerre-Gauss function
L_n	nth order Laguerre polynomial

LIST OF ABBREVIATIONS

FNAB	Fine Needle Aspiration Biopsy
MX	Mammography
PMT	Photomultiplier Tube
RNG	Random Number Generators
IMC	Inverse Monte Carlo
MIRD	Medical Internal Radiation Dose
MCAT	Mathematical Cardiac Torso
ACR	American Collage of Radiology
NEMA	National Equipment Manufacturers Association
DICOM	Digital Imaging and Communications in Medicine
JPEG	Joint Photographic Experts Group
MCAT	Mathematical Cardiac Torso
DWT	Discrete Wavelet Transform
MSE	Mean Square Error
SNR	Signal to Noise Ratio
PSNR	Peak Signal to Noise Ratio
ROC	Receiver Operator Characteristic Curve
AUC	Area Under the Curve
CHO	Channelized Hotelling Observer
TPF	True Positive Fraction
FPF	False Positive Fraction
DCT	Discrete Cosine Transform
SKE	Signal Known Exactly
BKE	Background Known Exactly
CR	Compression Ratio
PAC	Picture Archiving and Communications
SG	Simple Geometry
SB	Shape Based

VB	Voxel Based

1. INTRODUCTION

Image compression is concerned with minimizing the number of bits required to represent an image. Any image compression method attempts to answer two fundamental questions, namely, what information should be stored or transmitted, and how should the "chosen information" be compressed. The answers to both questions are related to the requirements of the application and the properties of the images.

Medical images are different from other classes of images, e.g., natural scenes. They are different in the way they are taken, the variations of gray levels and colors, the dynamic range, the size, and the type of noise that corrupts them. Moreover, the way medical image compression algorithms are evaluated differs from the evaluation of compression algorithms for other classes of images. When compressing images of natural scenes, the compression algorithms are concerned with the visual perception of the resulting image. However, medical image compression algorithms should be concerned with preserving the diagnostic information in the image. Although lossless image compression preserves all the information in the image including the diagnostic information, it fails to reduce the number of bits representing the image significantly. Thus, to achieve high compression ratios, we must look at lossy compression algorithms that preserve diagnostic information.

The application of lossy compression in medical image archiving or interchange is problematic because of the possible damage to diagnostically important information in the distorted original image. It is said that an irreversible process loses something every time it is applied and therefore conditions of diagnosis must necessarily be worse after 'lossy' compression. The doubts are intensified by the concern that correct interpretation of image information protects the health and even the life of a patient. Popular opinion also has it that the application of irreversible, implied to be lossy, compression in medical imagery is limited by legal restrictions, because of the loss of diagnostic accuracy. The scientific community has not yet reached a consensus on ir-

reversible compression and medical image data alteration (i.e. the reduced diagnostic accuracy of reconstructed images).

However, the need for significantly increased efficacy of image compression in medical applications is great and unquestionable. Fully lossless image compression reconstruction offers only a modest reduction in data size. The limited efficiency of reversible compression technologies (mostly up to $3:1$) does not satisfy the current needs concerning image storage and transmission. The volume of data from medical imaging systems, growing at exponential rates, and the development of newer radiology diagnostic procedures and conditions (in Picture Archiving and Communications (PAC) and teleradiology systems) require much more effective tools for compression of image data files and streams. The only way to significantly improve performance is to apply irreversible methods which are safe in the context of image-based diagnosis. Substantially higher compression ratios are achievable with irreversible techniques even with no perceptible or diagnostic degradation in image quality. Various image exams can be irreversibly compressed without losing diagnostic accuracy in the opinion of experts participating in reliable evaluation tests (and many others). Furthermore, image quality enhancement is possible in an irreversible process, where compressed high quality information may be superior to the initial lower quality image [9].

Moreover, Digital Imaging and Communications in Medicine (DICOM) has incorporated lossy JPEG and JPEG2000 procedures but have not addressed the amount of compression acceptable to users (responsibility is directed with radiologists and medical centres applying medical imaging technologies). The Food and Drug Administration (FDA), in spite of previous restrictions, have found the use of irreversible compression acceptable [10]. Their final ruling has removed the restriction relating to irreversible compression and extended the exemption from premarket notification to all medical image storage and communications devices (the technique and ratio are left to the radiologist's discretion, although the use of irreversible compression must be noted). Labelling and promotional materials of devices that utilize irreversible compression should clearly state the compression ratios provided. Such devices should be supplied with instructions that explain the effects of compression and include examples

of the effects of information loss on image quality. A message stating that irreversible compression has been applied and the approximate compression ratio (CR) should accompany images that have been subjected to irreversible compression. Many vendors of medical software support irreversible compression (compressed image transfer syntax as specified in the DICOM standard, making it possible to both store and distribute irreversibly compressed clinical images) in medical imaging systems (GE RadWorks, Centricity PACS, PERS, PICTools Medical Compression Toolkit, MedXpress, LEADTOOLS Medical, Aware JPEG2000, FUJIFILM Medical Systems and others).

Nevertheless, the final decision to safely apply irreversible compression strongly depends on the preferences, experience and knowledge of the responsible radiologist. Practicing radiologists need to understand the visual effects of irreversibility and nature of the degradation that occurs in order to optimise their image-based diagnosis procedure.

1.1 Problem Statement and Objectives

Experimental studies conducted conventionally for applying lossy compression use a set of real images for which a consensus is reached by a team of medical imaging specialists, on the presence or absence of a lesion. Then ROC (Receiver Operating Curve) Analysis is carried out in order to determine the effect of compression at different ratios in terms of lesion delectability. The area under the curve AUC equals one when a lesion can be detected perfectly well. The experiment is conducted by having a number of specialists evaluating films in a random manner without having any knowledge on the presence of a lesion or the compression ratio. This method has serious drawbacks though since it is time consuming and expensive and does not include any analysis for small subtle lesions. Furthermore, it is impossible to compare the errors due to other factors such as variation in equipment and data acquisition protocol.

This thesis has the objective of eliminating these drawbacks by using a computer simulation of the entire imaging chain that includes the organ, the imaging equipment

and the human observer. A Monte Carlo simulation package (SIMIND) has been used to simulate the image formation process for a gamma camera acquiring data from a breast containing a lesion. The obtained images are then compressed using the JPEG and JPEG 2000 algorithms at different compression ratios. Lesion delectability is then assessed by using a mathematical observer named the channelized hotel observer. Image quality is also assessed using quantitative image quality metrics.

1.2 Outline

Chapter 1 introduces the differences between medical images and other class of images. It gives a brief introduction about the medical image compression types and conditions of acceptability on lossy medical image compression. The importance of compression is also included in this chapter. The problem statement, our approach and our objectives are given within this section. Finally the outline of this study are presented in this section.

Chapter 2 gives comprehensive information about the theory of this study. Breast cancer diagnosis techniques, theory and instrumentation of breast scintigraphy imaging. Monte Carlo Method and its applications in nuclear medicine imaging are explained. The simulation package SIMIND is presented. The role of compression, types of image compression, the compression standards, basic components of a compression system, and the selected compression software are described. Furthermore, this chapter also includes the image quality metrics (i.e. MSE, PSNR, and SNR) to compare JPEG and JPEG 2000 algorithms. Finally signal detection theory and mathematical observer model (Laguerre-Gauss Channelized Hotelling Observer) are explained for evaluating reconstructed images' quality comprehensively.

Chapter 3 gives a systematic description about the materials and methods used in the thesis.

Chapter 4 presents the results of the study.

The conclusions and future work are discussed in Chapter 5.

2. THEORY

2.1 Diagnosis of Breast Cancer

The diagnosis of breast cancer is based on the utilization of physical examination, mammography and/or ultrasonography, and fine needle aspiration biopsy (FNAB) or core biopsy in accordance with the palpability and characteristics of the lesion, the age of the patient, and the density of the mammary gland [11, 12].

Even though clinical examination (inspection and palpation) is not a very sensitive test and its specificity is low, in particular for small lumps (less than 1 cm), it should be stressed that it remains the first and fundamental approach in the diagnosis of palpable breast cancer. However, during the past two decades, mammography has been completely transformed into a sophisticated technological method, with greatly improved image quality; it not only allows the recognition of very small, frequently non-palpable lesions, but also has become the method of choice for identifying breast carcinomas. The increasing use of screening mammography has resulted in an increase in the rate of detection of non-palpable lesions, and consequently in an increased demand for needle localizations and biopsies. In fact, in some cases the presence of microcalcifications at mammography is the only sign of breast cancer. It is possible to localize the position of this type of lesion with various methods: generally, a needle is positioned under mammographic control, leaving either a colored substance or a hook wire that provides a guide for the surgeon. In this way, the surgeon is able to remove the portion of the mammary gland that includes the lesion; the specimen should be submitted to radiography for confirmation of the complete removal of microcalcifications [13, 14].

It is important to point out that ultrasonography has very good ability to differentiate between cystic and solid masses, but its sensitivity for the detection of small carcinomas is not high. Its ideal use is in young women with full glandular breasts,

owing to their intrinsic radiopacity, while it can also be used for guidance in obtaining aspiration material for cytology [15].

Cytology entails the microscopic examination of cells obtained from nipple secretion, cystic fluids or fine needle biopsy of solid nodules, guided by ultrasonography or mammography in the case of non-palpable lesions. Cytology is particularly useful for breast lesions that cannot be clinically and/or mammographically defined as benign or malignant. The positive predictive value of this examination is extremely high but, unfortunately, there is a possibility of false-negative diagnosis, especially for small tumors. In such cases cytology should not be considered if clinical and/or mammographic suspicion of malignancy exists, rather, a biopsy of the lesions should be performed [16].

Figure 2.1 presents a flow chart in respect of these standard procedures for the diagnosis of palpable or non-palpable lesions of the breast.(a) is patients without breast diseases and (b) is patients with breast diseases. Fine-needle aspiration biopsy (FNAB) is preferred to core biopsy, which is often adopted in other centres. The routinely performed imaging procedures are mammography (MX) and ultrasonography (US). Other techniques such as digital mammography, computed tomography and magnetic resonance imaging are under evaluation in limited specific clinical trials.

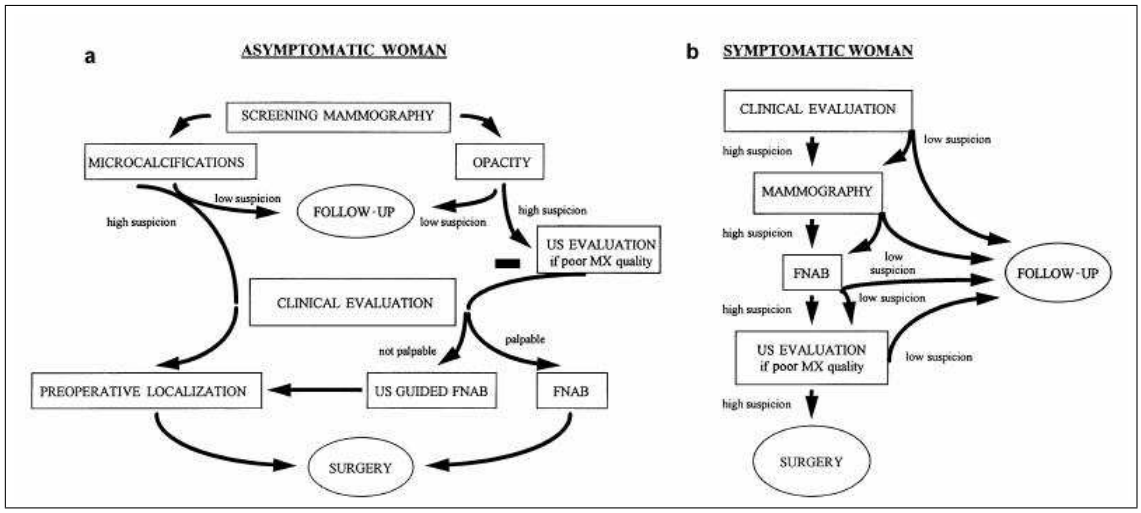

Figure 2.1 Flow chart of diagnostic procedures[1].

2.1.1 Radiological Techniques

Obviously, new radiological methods are under evaluation, such as digital mammography and magnetic resonance (MR) imaging. Considering the former, digital technology may provide several advantages over film/screen mammography, including wider variation in exposures, easier and more efficient storage of imaging on optical disks, and the possibility of transmitting these images over distances by the use of teleradiology. This evolution of the mammographic technique also significantly decreases the duration of needle localization procedures without reducing their accuracy. However, it seems that there are no differences between conventional and digital images with regard to the detectability of microcalcifications and masses [17, 18].

MR imaging provides an interesting advantage over conventional mammography in terms of three-dimensional imaging. Three-dimension imaging is suitable for thin-slice studies, allowing the detection of small enhancing lesions that might be missed if thicker slices were used. A number of potential roles for MR imaging in the study of breast cancer have been identified, including increasing the sensitivity and specificity of breast cancer detection by comparison with mammography, identifying recurrences, and monitoring response to chemotherapy. However, to date, MR imaging remains at the investigational stage and should not be used as a routine diagnostic tool [1].

2.1.2 Nuclear Medicine Techniques

Nuclear imaging involves the injection of pharmaceutical compounds that have been labeled with radioisotopes. The compounds are selected such that they couple to some sort of biological process such as blood flow, metabolic activity or enzyme production, or such, that they tend to accumulate at specific locations in the body, e.g. binding to certain cell receptor sites. Thus the relative concentration of these radiotracers in various areas of the body gives information about the relative degree to which these biological activities are occurring. Measurement of this concentration distribution therefore provides functional information very different from the structural

information supplied by modalities such as X-ray mammography and US. For this reason, nuclear medicine techniques are being explored as adjunct imaging approaches to the structurally oriented X-ray mammography [19].

The study of breast cancer is currently one of the most interesting areas of application of nuclear medicine. The reasons for this are (a) the recent technological progress that has occurred and (b) the introduction of new radiotracers which have not only allowed the production of images visualizing the site of the lesion, but also have provided biological and functional parameters that can characterize particular aspects of the tumor (vascularization, proliferative activity, metabolic activity, receptor status etc.). The importance of these parameters resides in the fact that they could be considered as prognostic indicators or as predictive indicators of the response to therapy, and thus be of great value in treatment planning and monitoring [1].

2.2 Breast Scintigraphy and Instrumentation

Within the past four decades, it has become evident that nuclear medicine imaging of cancerous lesions has specific merits in that it can image malignantly transformed tissues. The first nuclear medicine examination of the breast was published in 1946 using 32P-phosphorous [20]. In 1973, Berg et al first described the use of 99m-Tc-MDP for breast cancer detection [21]. In 1978, Hisada et al reported the first use of thallium- 201 for breast cancer imaging [22], and Goldenberg presented a trial using radiolabelled antibodies to detect breast cancer effectively[23]. In 1987, Muller et al. were the first to employ 99m-Tc-sestamibi for tumour detection[24]. Later in 1989, Kubota et al reported on a new technique using fluorodes oxyglucose to image malignant breast disease[25]. Aktolun in 1992 used sestamibi for breast cancer detection[26], and 3 years later, Rambaldi first described unintended imaging of breast cancer using 99m-Tc-tetrofosmin scintigraphy[27].

2.2.1 Breast Scintigraphy (Scintimammography)

Recent research has demonstrated that scintimammography with tumor-avid tracers (most commonly 99mTc-methoxyisobutylisonitrile, also known as sestamibi) and standard Anger gamma cameras can accurately diagnose primary breast cancer. Figure 2.2 depicts the basic scintimammography imaging situation. The patient is injected in with a quantity of radioactive tracer (typically 20 mCi of the aforementioned 99mTc-sestamibi) that will be returned to the heart through the venous system and then distributed throughout the body. The injection is typically made in the contralateral arm or leg to prevent radionuclide tracer near the injection site from appearing in the breast image. Because of their high metabolic activity and well-developed vascularization, tumors will tend to collect more of the tracer per volume than will healthy tissue. Thus when the radioactive tracer decays and emits gamma rays, a larger number of these gammas will originate from tumor sites than from equal volumes of healthy tissue. A scintillation camera equipped with a collimator is used to observe the gamma rays and generates a two-dimensional image of the tracer distribution in the breast, allowing visualization of any tumors present as "hot spots." The total body dose for a 20 mCi injection of 99mTc-sestamibi is about 330 mrem, but the effective dose calculated by using weighting factors for sensitive internal organs is closer to 500-600 mrem. Scintimammography obtained FDA approval in 1997.

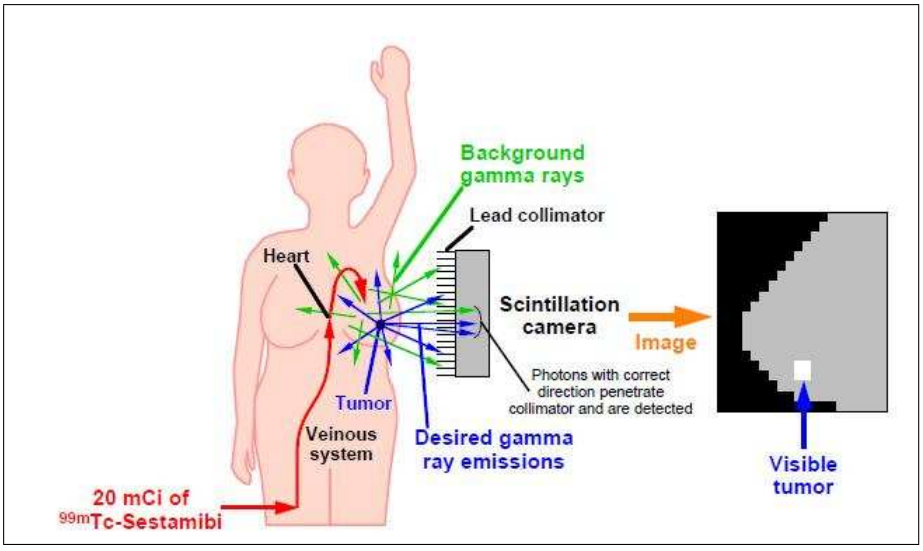

Figure 2.2 The basic scintimammography imaging situation

Early studies of 201Tl [28] and 99mTc-sestamibi [29, 30] have shown that these agents are frequently taken up by breast cancers, and to a lesser extent, by other mammographically detected abnormalities. 99mTc-sestamibi (MiralumaTM, DuPont Merck Pharmaceutical Company, North Billerica, MA), however, is currently the most promising tumor-avid tracer for scintimammography. It is a lipophilic cation originally developed as a cardiac perfusion agent and approved in the United States in December, 1990 for clinical use in the detection of coronary artery disease. Its chemical structure is given in Figure 2.3. The exact mechanism for cellular uptake of sestamibi by cancer cells is still uncertain, but sestamibi is known to be a P-glycoprotein transport substrate and this could be the tracer's means of uptake [31]. Sestamibi appears to accumulate in cells in relation both to perfusion and to the negative plasma and mitochondrial membrane potentials (which exert an electrostatic force on the positively-charged sestamibi) [32]. The accumulation of sestamibi in chick myocardial cells has been shown to depend heavily on the retention of the radionuclide by mitochondria [33]. Further, the mitochondrial retention of sestamibi does not appear to be organ-specific in human carcinoma cell cultures over 90% of the activity is concentrated in the mitochondria [34]. Studies suggest that the tumor-to-breast tissue uptake ratio in patient studies varies significantly but can be expected to be approximately 4-6 [35]. This contrast is substantially higher than that of X-ray mammography (where tumor tissue may only be 5% denser than normal tissue) and represents an important strength of scintimammography. Although 99mTc-sestamibi is presently the ligand most frequently used for scintimammography, other tracers such as 201Tl, 99mTc-MDP, 99mTc-tetrofosmin, radiolabeled antibodies, radiolabeled estrogen receptor ligands, radiolabeled somatostatin compounds, and radiolabeled chemotherapeutic agents are currently under active investigation [36, 28].

A number of investigators have demonstrated sensitivities of 83-94% and specificities of 88-93% for scintimammography imaging of suspected breast lesions using sestamibi and conventional Anger cameras [37]. Evidence further suggests that this modality performs equally as well when imaging radiographically dense and/or glandular breasts [38]. While all of this is indeed cause for optimism, caution must be exercised with scintimammography because the sensitivity can drop to as low as 62%

in patient populations with predominantly non-palpable lesions [32] and sensitivity for tumors less than 1 cm in diameter is often poor [39]. Finally, scintimammography has also shown some promise in evaluating the axillary lymph nodes, demonstrating sensitivities of 64-82% and specificities of 78-90% [37].

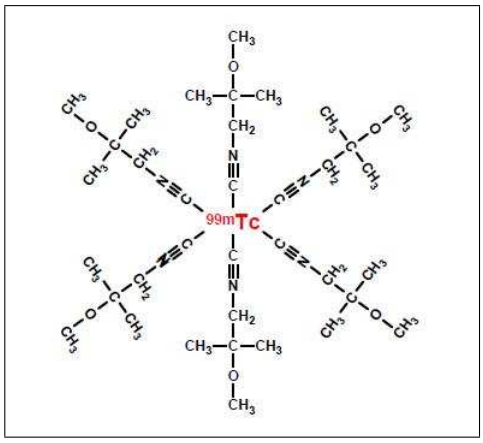

Figure 2.3 Chemical structure of 99mTc-sestamibi

It is believed that the number of false negatives (i.e., missed tumors) could be reduced if the limitations of contemporary gamma cameras were overcome. For example, reference [40] discovered that three of the four false negatives which occurred during the study involved tumors in the medial part of the breast in a volume that was out of close camera contact. Detection of breast lesions in the internal quadrants is especially important because these tumors may disseminate towards the internal mammary chain even when no axillary node is invaded [41]. This problem could be solved by compact, thin gamma cameras that eliminate the dead space and large size which are typical of traditional gamma cameras and which limit access to the breasts and axillary nodes. Easy access to all nodes and potential breast lesion sites will improve image quality and can be expected to improve the diagnostic accuracy of scintimammography.

While researchers agree that scintimammography is unlikely to replace Xray mammography as a mass screening tool, most believe that many patients can benefit from it. In brief, scintimammography is attractive when X-ray mammography is impaired, namely in women with dense or scarred breasts. Scintimammography may also be used to check for multicentric disease, to evaluate the effectiveness of chemother-

apy as treatment progresses, and, if its sensitivity can be improved, to noninvasively evaluate axillary lymph node involvement. Finally, any tumors visible only to scintimammography scans will require scintimammography-guided biopsy techniques.

2.2.2 Instrumentation of Breast Scintigraphy

A single- or multiple-head gamma camera is needed to acquire planar and/or tomographic (SPECT) images. This gamma camera should be equipped with a low energy, high-resolution collimator. An imaging table (mattress) with specially designed breast cutouts to allow the breast to be fully dependent or with a foam cushion with a lateral semicircular aperture is required. The energy window for image collection should be 10% (±5%) centered over the 140-keV photopeak of 99mTc [42].

2.2.3 Gamma Camera

The first instrumentation that could generate images of radionuclide distributions appeared in the late 1940s, but it was simplistic and of limited use. The 1950s saw the advent of Benedict Cassen's rectilinear scanner, wherein a single radiation detector element could be mechanically moved ("scanned") across the area of interest and, given enough time, generate an image from the data accumulated at different locations. Rectilinear scanners have been greatly improved over the years and still find some use in nuclear medicine today, but fill relatively small roles. A more decisive advance in nuclear medicine occurred in 1953 when Hal Anger first described a system capable of observing radioactivity at all points in an image simultaneously.This first configuration used a relatively thin block of NaI(Tl) scintillator to cover the target area and a sheet of X-ray film to record the resulting scintillation events. Unfortunately, this detector was so inefficient that prohibitively long imaging times and/or high levels of administered radionuclide were required.

The real breakthrough came in 1958 when Hal Anger invented his scintillation

camera (also known as a gamma camera or Anger camera), a device that has dominated radionuclide imaging ever since. This camera design uses a single block of NaI(Tl) scintillator large enough to cover the desired imaging area and thick enough to efficiently stop gamma rays. The major improvement over the previous incarnation,however, is the use of an array of photomultiplier tubes (PMTs) to detect the scintillation light produced by the NaI(Tl). This array of photosensitive devices provides reasonably efficient detection of the scintillation light, good spatial localization by means of Anger logic, and excellent pulse height (i.e., energy) resolution. Over the years the Anger scintillation camera has evolved and undergone significant improvements, but the basic concept has largely remained the same. No other nuclear medicine imaging system has yet to truly challenge the Anger camera for its combination of image quality, affordability, and ease of use in a hospital setting, but recent technological advances may change that in the future.

2.2.3.1 Basic Principles. A scintillation camera functions by converting individual gamma rays into thousands of visible light photons, detecting those photons with photosensitive elements that generate electric signals, and finally integrating the information carried by the electric signals into a coherent image. The basic components of an Anger scintillation camera include a collimator, a large NaI(Tl) scintillator crystal block, an array of PMTs (optically coupled to the scintillator), electronics which read out the electrical pulses generated by the PMTs, and a computer/image display system for presenting the data. Additionally, the NaI(Tl) is shielded from stray radiation with lead and hermetically encased to protect it from moisture in the air (because NaI(Tl) is very hygroscopic). The NaI(Tl) crystal block is typically cylindrical with a diameter of about 30-50 cm (though rectangular designs covering comparable area also exist) and a depth of about 1.25 cm. For cameras dedicated to imaging low energy sources such as 201Tl or 99mTc, a lesser NaI(Tl) thickness of only 6-8 mm is employed. The slight decrease in radiation detection efficiency is justified by the improved energy and spatial resolutions resulting from better light collection by the PMTs. Finally, the readout electronics consist of two subsystems. The first is the Anger logic circuitry, which estimates the 2-D location of the observed radiation event. The second is the

pulse height discriminator, which estimates the energy of the gamma ray based on the PMT pulse amplitudes and allows only events within the appropriate energy range to be incorporated into the image (energy discrimination). This rejects scattered gamma rays containing little useful information and improves the noise quality of the resulting images. The basic components of an Anger scintillation camera are summarized in Figure 2.4.

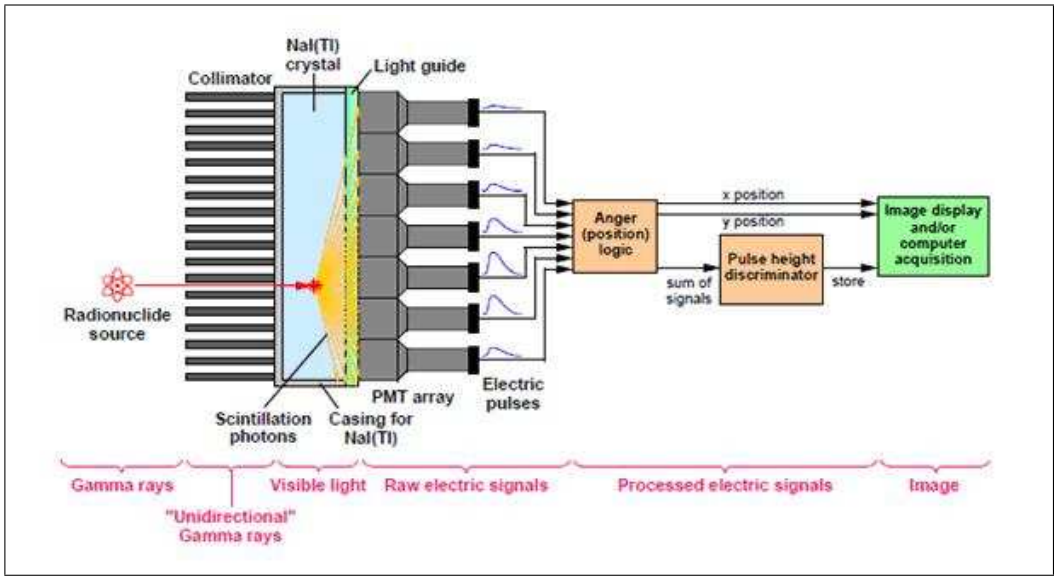

Figure 2.4 Basic components of the Anger scintillation camera.

PMTs are critical to the operation and performance of Anger scintillation cameras but present very significant requirements in terms of volume, component cost, and voltage supply. These devices are typically about 5-8 cm in diameter by about 12 cm in length, cost around \$150 to \$200 each, and operate off of a >1 kV supply. Higher quality cameras tend to use smaller PMTs, increasing accuracy but necessitating a greater number of devices and therefore increasing cost. PMT quantum efficiency for the 415 nm scintillation photons produced by NaI(Tl) is only about 20-25% (i.e., only about 1 in 4 or 5 photons striking the PMT face is actually detected).

The readout electronics (both the Anger logic and the pulse height analyzer) rely upon the fact that the height of an output pulse from a given PMT is linearly proportional to the number of scintillation photons striking its face. As a result, a reasonable measure for the total number of scintillation photons produced by a gamma

interaction is given by the sum of the pulse heights of all the PMT signals. Further, because the number of scintillation photons generated by the crystal is proportional to the energy of the incident gamma ray, the energy of observed gamma rays can be estimated as:

$$gamma\ energy \propto \sum_{i=1}^{n} (pulse\ height\ from\ PMT_i) \tag{2.1}$$

where n is the total number of PMTs in the array. Calibration can easily be performed using a source of known energy in the absence of scatter. The calibrated output from Equation2.1 can thus be used for purposes of energy discrimination.

The number of photons impinging upon each PMT depends heavily upon the location of the gamma ray interaction, and Anger logic exploits this dependency by weighting each PMT based upon the height of its output pulse. Figure 2.5 shows an array of 37 PMTs used to read out the scintillation light from a large NaI(Tl) crystal. It is straightforward to assign the center of each PMT an (x, y) coordinate and then compute the location of interaction as the centroid of the PMT signals:

$$x_{interaction} = \frac{\sum_{i=1}^{n} x_i(pulse\ height\ from\ PMT_i)}{\sum_{i=1}^{n} (pulse\ height\ from\ PMT_i)} \tag{2.2}$$

where x_i is the x coordinate of a given PMT and n is the total number of PMTs. The y coordinate of the interaction site is also computed using Equation 2.2, but naturally with the appropriate substitutions of y for x.

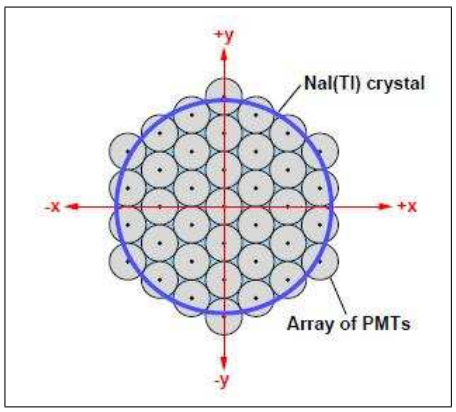

Figure 2.5 An example array of 37 PMTs used in an Anger scintillation camera

Measurement error in scintillation cameras has three predominant sources:

1. Light collection inhomogeneity
2. Electronic noise and
3. Limited counting statistics

Light collection inhomogeneity refers to the fact that the total number of visible light photons observed by the photodetector system (in the case of an Anger camera, the array of PMTs) varies depending on the site of gamma ray interaction. The farther the interaction is away from the face of the PMTs, for instance, the fewer scintillation photons tend to be detected. Location-dependent differences in light collection can also occur because of crystal defects, light guide aberrations, or variations in photodetector quantum efficiency. All of this contributes to error in energy resolution (as per Equation 2.1) because the total number of observed scintillation photons varies independently of gamma ray energy. Inhomogeneity also introduces variations into the terms in Equation 2.2, resulting in increased spatial localization error. Finally, near the edge of the scintillator crystal in an Anger camera, the reflection of photons off the side of the crystal is a significant source of error, worsening energy resolution and greatly skewing spatial localization.

Electronic noise increases the error in both the energy and location measurements by adding random fluctuations to the information-carrying electric signals. In the case of Anger cameras, however, this noise component is negligible because the PMT gain is large enough (around 10^6) that the resulting signals are immune to small noise variations.

Finally, limited counting statistics represent a significant source of error, especially in Anger logic. All of the pulse height terms in Equation 2.2 suffer Poisson fluctuations by

$$\sigma \approx \sqrt{N} (for\ Poisson\ distribution)$$

error which propagates into the final x and y coordinates. Counting statistics also contribute to error in energy resolution, but the effect is less pronounced because all of the PMT signals are summed together in Equation 2.1, resulting in a larger signal, N, and hence smaller relative noise, σ/N.

2.2.3.2 Collimators. The purpose of the collimator is to project an image of gamma rays onto the surface of the camera crystal. Holes are positioned in the collimator so that each point on the crystal's surface has a direct view only of one point on the surface of the target. In effect, each point of the crystal is able to see only the radiation originating from a corresponding point on the patient's body.

Collimators play a crucial role in defining a systems extrinsic imaging characteristics. The energy rating of a collimator indicates the maximum energy of photons that can be efficiently handled by the collimator. This is usually defined as the energy at which less than 5% of the off-axis photons pass through the collimator. Low energy collimators are designed for a maximum energy of 140 to 200 keV, while medium energy collimators are effective up to 300-400 keV. The energy rating of the collimator also dictates septal thickness. Although tungsten absorbs photons more efficiently, most collimators are made of lead due to its lower cost.

There are broadly four types of collimators: parallel hole, converging, diverging, and pinhole. We will be using parallel-hole collimator for imaging the breast. There are also slant hole and fan-beam collimator types [43].

A common arrangement is for the collimator holes to be parallel, as illustrated in figure 2.6. The FOV is determined by the size (diameter) of the crystal and remains the same at all source-to-camera distances. The size of the image at the crystal is the same as the actual size of the radioactive source being imaged. This relationship does not change with distance. Therefore, the parallel-hole collimator does not produce either magnification or minification of the image. The photons that pass through the parallel hole collimator are the ones moving in a direction parallel to the holes. Assuming there

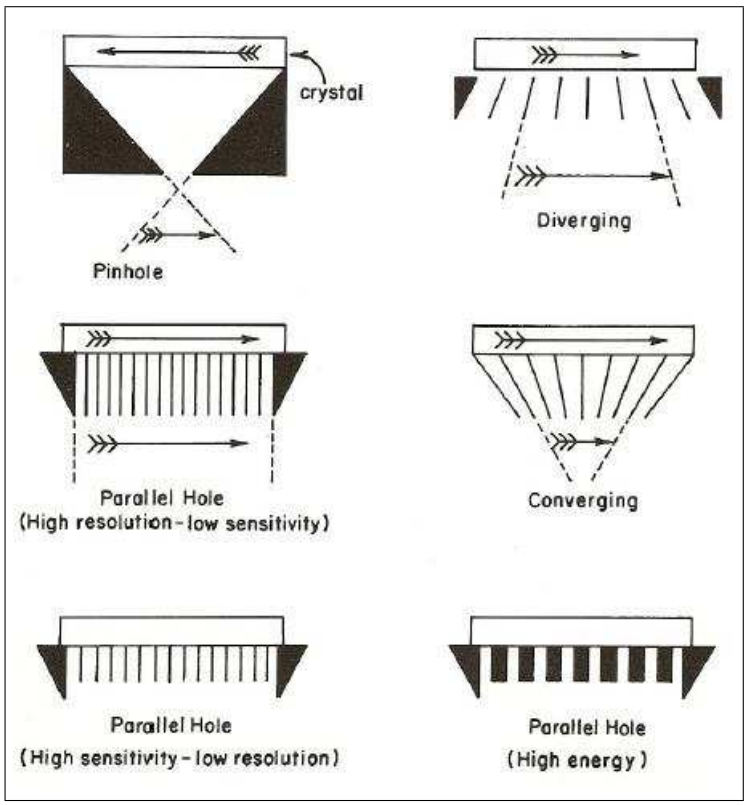

Figure 2.6 Types of gamma camera collimators [2].

is no photon absorption between the source and collimator, the number of these parallel photons does not change significantly with the source-to-camera distance. Therefore, camera sensitivity with a parallel-hole collimator is generally not affected by changing the distance between the source and camera [43, 44].

The thickness of the collimator, the orientation and size of the holes as well as the distance between source and collimator define the resolution and sensitivity of the camera.

For a parallel-hole collimator the spatial resolution R_e is determined by the hole length L, the hole diameter d, and the source to collimator distance z:

$$R_e = \frac{d \times (L + z)}{L} \tag{2.3}$$

Looking at the Equation 2.3 , we can see that a decrease in z and d, improves the spatial resolution, while the length of the collimator holes is less influential (typically

determined by the thickness of the collimator material necessary to absorb gamma radiation).

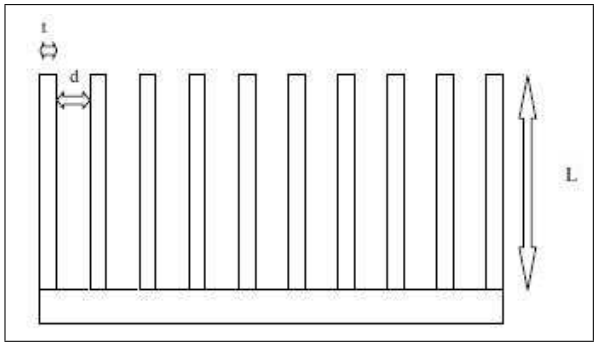

Figure 2.7 Parallel Hole Collimator where t is the septal thickness, d is the hole size, and L is the hole length

The collimator plane source sensitivity is defined as the response of the collimator to an infinite plane source of radioactivity located in the object plane. In the case of cylindrical parallel-hole multi-channel collimators used with a scintillation camera, the total plane source sensitivity S is given by:

$$S \approx d^4/L^2a^2 \tag{2.4}$$

Where d is the radius of the collimator hole, L is the hole length and a is the distance between centers of adjacent holes.

2.2.3.3 Resolution and Sensitivity. The differences among the collimators are the thickness, number, and size of the holes and the way they are oriented. This, in turn, has an effect on the camera sensitivity, FOV (Field of View) image magnification, and image blur.

Resolution and sensitivity of a collimator are inversely related. The best spatial resolution is achieved with collimators with long holes of a small diameter because the angle of acceptance is smaller and more scatter is rejected. Sensitivity, or efficiency, refers to the fraction of emitted photons, which actually pass through the collimator and reach the detector.

The sensitivity increases as the square of the hole size, and decreases as the square of the hole length. Thus, collimator resolution improves as:

- The diameter of the collimator holes decreases
- The effective length of the collimator holes increases
- The object to collimator distance decreases [43, 44].

Collimator septa play a crucial effect on the resolution and sensitivity of the camera. Longer septa in the collimator attenuate most photons, except those exactly perpendicular to the crystal face. This increase in selectivity increases the resolution and decreases the count rate detected. Shortening the length of the septa allows more photons to reach the crystal; thus, the count rate is higher. The spatial resolution is decreased because the photons coming through a hole in the collimator are from a larger area.

2.3 The Monte Carlo Method

Numerical methods that are known as Monte Carlo methods can be loosely described as statistical simulation methods, where statistical simulation is defined in quite general terms to be any method that utilizes sequences of random numbers to perform the simulation. Monte Carlo methods have been used for centuries but only in the past several decades has the technique gained the status of a full-edged numerical method capable of addressing the most complex applications. The name Monte Carlo was chosen during the World War II Manhattan Project because of the close connection to games based on chance and the location of a very famous casino in Monte Carlo [45].

Monte Carlo techniques have become one of the most popular tools in different areas of medical physics following the development and subsequent implementation of

powerful computing systems for clinical use. In particular, they have been extensively applied to simulate processes involving random behavior and to quantify physical parameters that are difficult or even impossible to calculate analytically or to determine by experimental measurements. The applications of the Monte Carlo method in medical physics cover almost all topics, including radiation protection, diagnostic radiology, radiotherapy and nuclear medicine, with an increasing interest in exotic and new applications, such as intravascular radiation therapy, boron neutron capture therapy and synovectomy [46].

2.3.1 Principles

The general idea of Monte Carlo analysis is to create a model, which is as similar as possible to the real physical system of interest, and to create interactions within that system based on known probabilities of occurrence, with random sampling of the probability density functions (PDF's). As the number of individual events (called histories) is increased, the quality of the reported average behavior of the system improves, meaning that the statistical uncertainty decreases. Assuming that the behavior of the imaging system can be described by probability density functions pdf's, then the Monte Carlo simulation can proceed by sampling from these pdf's, which necessitates a fast and effective way to generate random numbers uniformly distributed on the interval. Photon emissions are generated within the phantom and are transported by sampling from pdf's through the scattering medium and detection system until they are absorbed or escape the volume of interest without hitting the crystal. The outcomes of these random samplings, or trials, must be accumulated or tallied in an appropriate manner to produce the desired result, but the essential characteristic of Monte Carlo is the use of random sampling techniques to arrive at a solution of the physical problem [47, 3].

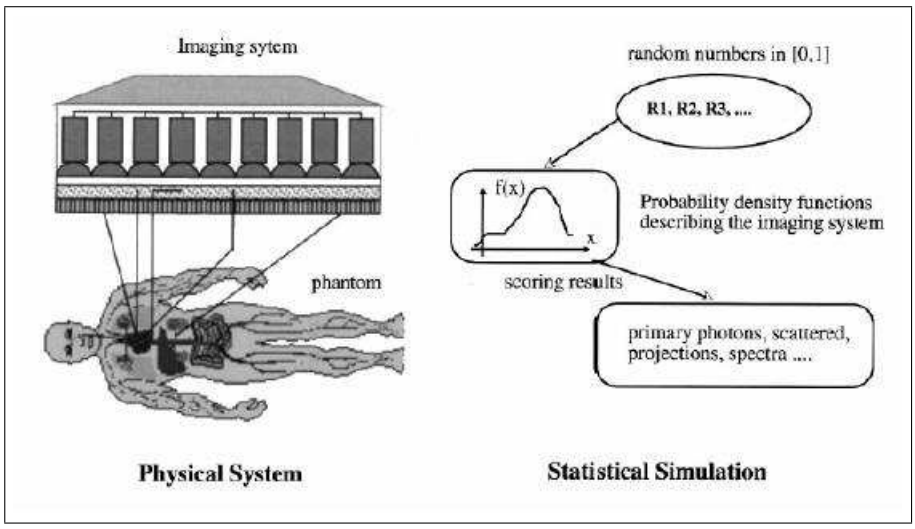

Figure 2.8 Principles of Monte Carlo simulation of an imaging system [3]

The primary components of a Monte Carlo simulation method include the following;

1. Probability density functions (pdf's) : the physical system must be described by a set of pdf's.

2. Random number generator: a source of random numbers uniformly distributed on the unit interval must be available.

3. Sampling rule: a prescription for sampling from the specified pdf's.

4. Scoring: the outcomes must be accumulated into overall tallies or scores for the quantities of interest.

5. Error estimation: an estimate of the statistical error (variance) as a function of the number of trials and other quantities must be determined.

6. Variance reduction techniques: methods for reducing the variance in the estimated solution to reduce the computational time for Monte Carlo simulation.

7. Parallelization and vectorization algorithms to allow Monte Carlo methods to be implemented efficiently on advanced computer architectures [3].

2.3.1.1 Random Number Generation. Random number generation is a key issue for the Monte Carlo Method, which is used to estimate true random events. Monte Carlo methods make extensive use of random numbers to control the decision-making when a physical event has a number of possible results.

Random number generators (RNG) are based upon specific mathematical algorithms so that they have the appearance of randomness but nevertheless exhibit a specific repeatable pattern. A large number of generators are readily available, and many of these are suitable for the implementation on any computer system. A typical simulation uses from 107 to 1012 random numbers, and subtle correlations between these numbers could lead to significant errors. The largest uncertainties are typically due more to approximations arising in the formulation of the model than those caused by the lack of randomness in the RNG.

The sequence of random numbers used to affect a Monte Carlo model should possess some properties. The sequences of random numbers should be serially uncorrelated. The generator should not repeat; practically, the repetition should occur only after the generation of a very large set of random numbers. The sequence of random numbers should be uniform, and unbiased. The generation of the random numbers should be fast and reproducible. Linear congruential and Lagged-Fibonacci generators are the most commonly used generators[3].

2.3.1.2 Analog Sampling. Analog Monte Carlo attempts to simulate the full statistic development of the electromagnetic cascade. If we assume that a large number of particle histories, N, are included in a batch, the individual batch estimates can be considered as drawn from a normal distribution. For a given calculation, the estimated uncertainty is proportional to the inverse of the square root of the number of histories simulated. The efficiency ε of a Monte Carlo calculation can therefore be defined as;

$$\varepsilon = \frac{1}{\sigma^2 \, T^2} \tag{2.5}$$

where T is the calculation time to obtain a variance estimate σ^2 For large N, ε should be constant as long as the calculation technique remains the same. As described earlier, the imaging system can be described in terms of pdf's. These pdf's, supplemented by additional computations; describe the evolution of the overall system, whether in space, energy, time or even some higher dimensional phase space. The goal of the Monte Carlo method is to simulate the imaging system by random sampling from these pdf's and by performing the necessary supplementary computations needed to describe the system evolution. In essence, the physics and mathematics are replaced by random sampling of possible states from pdf's that describe the system. Thus, it is frequently necessary to sample some physical event, the probability of which is described by a known pdf. Let x be the physical quantity to be selected and f(x) the pdf. Among the properties of the pdf is that it is integrable and non-negative. Assume that the domain of f(x) is the interval [xmin ,xmax] and that it is normalized to unit area. The cumulative distribution function F(x) of the frequency function f(x) is defined as;

$$F(x) \equiv probability(\tau \leq x) = \int_{x_{min}}^{x} f(\tau) d\tau \tag{2.6}$$

A stochastic variable can be sampled by the use of uniformly distributed random numbers R in the range [0-1] using one of the techniques described below [47, 3].

1. Direct Method.

   This method can be used if the inverse of the cumulative distribution function F^{-1}(x) is easily obtainable. Since $F(x)$ is uniformly distributed in [0-1], the sampled value of x could be obtained by substituting $F(x)$ in equation 2.6 by a uniform random number R, that is, $x = F^{-1}(R)$. A practical example of using this technique is the calculation of the distance to the next interaction vertex. The inversion is not always possible, but in many important cases the inverse is readily obtained [3].

2. Rejection Method.

   Another method of performing this when it is too complicated to obtain the inverse of the distribution function is to use the rejection technique, which follows the following steps: (i) Define a normalized function $f'(x) = f(x)/fmax(x)$,

where $fmax(x)$ is the maximum value of $f(x)$;

(ii) Sample two uniformly distributed random numbers R_1 and R_2;

(iii) Calculate x using the equation $x = x_{min} + R_1 \times (x_{max} - x_{min})$; and

(iv) If R_2 is less than or equal to $f^{'}(x)$, then x is accepted as a sampled value; otherwise a new value of x is sampled.

Over a large number of samples, this technique will yield a set of values of x within the required distribution. It does, however, require two random numbers per trial and many trials may be required depending on the area under of the curve of $f(x)$. A typical example of using this technique is the photon energy and scattering angle resulting from incoherent scattering[3].

3. Mixed Methods.

When the previous two methods are impractical, the mixed method that combines the two may be used. Assume that the pdf can be factored as follows:

$f(x) = h(x)g(x)$,

where $h(x)$ is an invertible function and $g(x)$ is relatively flat but contains most of the mathematical complexity.

The method consists of the following steps:

(i) Normalize $h(x)$ producing $h^{'}(x)$ such that$\int_{x_{min}}^{x_{max}} h^{'}(x)dx = 1$;

(ii) Normalize $g(x)$ producing $g^{'}(x)$ such that $g^{'}(x) \leq 1$ for x in $[x_{min}, x_{max}]$;

(iii) Use the direct method to select an x using $h^{'}(x)$ as the pdf;

(iv) Use x and apply the rejection method using $g^{'}(x)$, i.e., choose a random number R, if $g^{'}(x) \leq R$, accept x; otherwise go back to step (iii)[3].

2.3.1.3 Non-analog Sampling (Variance Reduction Techniques). A direct Monte Carlo simulation using true probability functions may require an unacceptable long time to produce statistically relevant results. Photons emission is isotropic, so directional parameters may be sampled uniformly within their individual ranges. The geometrical efficiency of a low-energy, general purpose collimator is of the order of

10^{-4}. When direct Monte Carlo simulations were applied in this case, then 9999 photons, on the average, would be rejected for each photon passing through a collimator hole, because of the small solid angle defined by the collimator holes. Therefore, the calculation would be very ineffective in terms of required computing time. It is thus desirable to bias the sampling (non-analog sampling) by introducing different types of importance sampling and other variance reduction techniques to improve the computational efficiency of the Monte Carlo method. The results obtained by nonanalog simulation are, however, biased by the variance reduction technique and a correction for this is required. A particle history weight, W, is introduced, which describes the probability of the particle following the current path. This weight is calculated for each particle history, and used in the calculation of the results. If an event occurs, the weight W is added to the counter rather than incrementing the counter by one unit. There are many different variance reduction techniques in nuclear medicine[3, 48].

2.3.2 Monte Carlo Techniques in Nuclear Medicine

There has been an enormous increase and interest in the use of Monte Carlo techniques in all aspects of nuclear imaging, including planar imaging, SPECT, PET and multimodality imaging devices. However, due to computer limitations, the method has not yet fully lived up to its potential. With the advent of high-speed supercomputers, the field has received increased attention, particularly with parallel algorithms, which have much higher execution rates.

The Monte Carlo method is a widely used research tool for different areas of diagnostic nuclear imaging, such as detector modeling and systems design, image correction and reconstruction techniques, internal dosimetry and pharmacokinetic modeling. The method has proven to be very useful for solving complex problems that cannot be modeled by computer codes using deterministic methods or when experimental measurements may be impracticable. The design of SPECT and PET systems using the Monte Carlo method has received considerable attention, and a large number of applications were the result of such investigations. During the past two decades, the

simulation of scintillation camera imaging using both deterministic and Monte Carlo methods has been developed to assess qualitatively and quantitatively the image formation process and interpretation and to assist in the development of collimators. Several researchers have also used Monte Carlo simulation methods to study potential designs of dedicated small animal positron tomographs.

Another promising application of Monte Carlo calculations is the development and evaluation of image reconstruction algorithms and correction methods for photon attenuation and scattering in nuclear medicine imaging, since the user has the ability to separate the detected photons into their components: primary events scatter events, contribution of down scatter events, etc. Monte Carlo modeling thus allows a detailed investigation of the spatial and energy distribution of Compton scatter, which would be difficult to perform using present experimental techniques, even with very good energy resolution detectors.

Monte Carlo simulations have been shown to be very useful for the validation and comparative evaluation of image reconstruction techniques. Smith et al. used Monte Carlo modeling to study photon detection kernels, which characterize the probabilities that photons emitted by radioisotopes in different parts of the source region will be detected at particular projection pixels of the projection images for the case of parallel hole collimators. The authors also proposed a reconstruction method using 3-D kernels, in which projection measurements in three adjacent planes are used simultaneously to estimate the source activity of the centre plane. The search for unified reconstruction algorithms led to the development of Inverse Monte Carlo (IMC) reconstruction techniques. The principal merits of IMC are that, like direct Monte Carlo methods, the method can be applied to complex and multivariable problems, and variance reduction procedures can be applied [45, 46, 3].

2.3.2.1 Detector Modeling. Monte Carlo simulation of detector responses and efficiencies is one of the areas, which has received considerable attention. The critical component of emission tomography is the scintillation detector. Increased light

per gamma ray interaction, faster rise and decay times, greater stopping power and improved energy resolution are the desired characteristics. Improvements in these characteristics enable detectors to be divided into smaller elements, thus increasing resolution and minimizing dead-time losses [3].

2.3.2.2 Imaging Systems and Collimators Design. Simulations of gamma camera imaging to assess qualitatively and quantitatively the image formation process and interpretation and to assist development of collimators using deterministic methods and simplifying approximations have been developed mainly to improve speed of operation.

In gamma camera imaging, there is a compromise between sensitivity and spatial resolution in collimator selection. In 1988, Hahn et al. evaluated the properties of a cone beam (CB) collimator and three dimensional filtered back projection algorithms. For this purpose, the noise characteristics of this collimator configuration were determined and comparisons with a parallel hole (PH) collimator were made. They have used Monte Carlo simulation to gather the data used for the measurements [98]. Dye (1988) highlighted the need for an improved strategy for decision-making in equipment design and other practical issues in nuclear medicine [49, 50].

In 1990, Gantet et al. presented a computer simulation of photon interaction with collimator septa, which allows the point spread function of scintillation camera collimators to be calculated. The method simulates photon attenuation along their propagation direction in a determinist way. Using this simulation, the spatial resolution, geometric efficiency and penetration index of collimators may be easily assessed [51].

To that end, in addition to its quantitative clinical applications, Monte Carlo simulation may be a useful research tool for tasks such as evaluating collimator design and optimizing gamma camera motion [3].

2.3.2.3 Image Reconstruction Algorithms. Monte Carlo simulations have been shown to be very useful for validation and comparative evaluation of image reconstruction techniques since it is possible to obtain a reference image to which reconstructed images should be compared [3].

2.3.2.4 Attenuation and Scatter Correction Techniques. The presence of scatter and attenuation in the images limits the accuracy of quantification of activity [52]. With no corrections, the uncertainty could be as high as 50-100% [53].

Scatter does not produce major artifacts comparable to attenuation but reduces image contrast by including a low frequency blur in the image. The impact of scatter generally depends on the photon energy, camera energy resolution, and energy window settings, besides the object shape and the source distribution [54]. Many of these parameters are nonstationary, which implies a potential difficulty when developing proper scatter and attenuation correction techniques. However, correction for scatter remains essential, not only for quantification, but also for lesion detection and image segmentation.

Monte Carlo simulations have been found to be powerful tools to quantify and correct for photon attenuation and scattering in nuclear medicine imaging since the user has the ability to separate the detected photons into their components: primary events, scatter events, contribution of down-scatter events, etc. Monte Carlo modeling thus allows a detailed investigation of the spatial and energy distribution of Compton scatter which would be difficult to perform using present experimental techniques, even with very good energy resolution detectors [55].

In gamma camera imaging and SPECT, simulation programs have been used to obtain information on the different processes occurring within the phantom and the detectors. For example, energy pulse-height distribution, point-spread function and the scatter fraction can be obtained [4]. The scattered events in the energy-pulse-height distribution can be separated according to the number of scattering events in

the phantom (Figure 2.9). It is clearly shown that a significant number of scattered events will be accepted by the photopeak energy window. The scatter fraction which is defined as the ratio between the number of scattered photons and the total number of photons (scattered and unscattered), is of great importance for quantitative estimation of the scattering contribution.

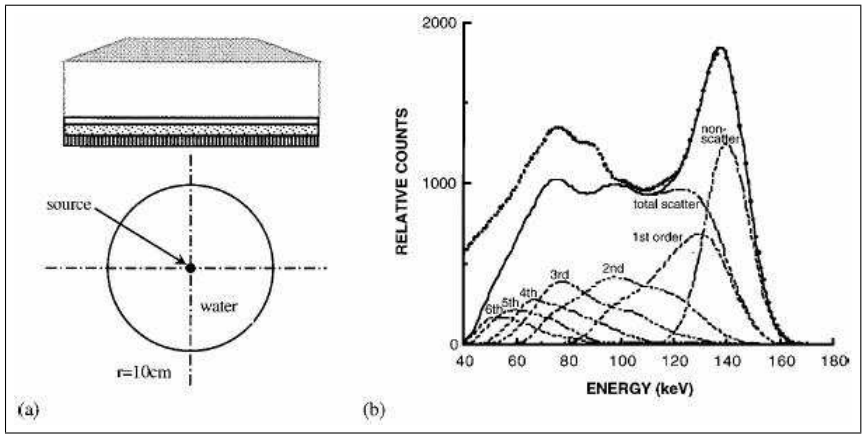

Figure 2.9 (a) Schematic view of a 99mTc line source placed at the centre of a water-filled cylinder to a scintillation camera. (b) A comparison between calculated (solid line) and experimental (dots) energy spectra for a line source on the axis of a water-filled cylinder. Distribution of the various orders of scattered and non-scattered photons is shown by broken lines [4].

2.3.2.5 Dosimetry and Treatment Planning. The area where early Monte Carlo simulations in the field have been performed is dosimetry modeling and computations [56]. The approach adopted by the Medical Internal Radiation Dose (MIRD) committee was first proposed in 1968 and published in a series of supplements to the Journal of Nuclear Medicine as different pamphlets [57, 58]. Some of these pamphlets made extensive use of Monte Carlo calculations to derive specific absorbed fractions for electron and photon sources uniformly distributed in organs of mathematical phantoms [3].

2.3.2.6 Pharmacokinetic modeling. Pharmacokinetic modeling is a useful component for the estimation of cumulated activity in various source organs in the body. A few applications of Monte Carlo techniques have been reported in the field of pharmacokinetic modeling [3].

2.3.3 Object Model and Software Phantoms

Mathematical descriptions of human bodies and anthropomorphic phantoms are useful in radiation transport calculations. They are widely used in computer calculations of doses delivered to the entire body and to specific organs, and are valuable tools in the design and assessment of image reconstruction algorithms.

Software phantoms modeled in imaging situations were historically limited to simple point, rod, and slab shapes of sources and attenuating media. Such simple geometries are useful in studying fundamental issues of scatter and attenuation, but clinically realistic distributions can not be evaluated by such simple geometries. A precise modeling of the human body requires appropriate information on the location, shape, density and elemental composition of the organs or tissues [3].

2.3.3.1 Object modeling. Object modeling is fundamental for performing photon and electron transport efficiently by means of a Monte Carlo method. It consists of a description of the geometry and material characteristics for an object. The material characteristics of interest include density and energy-dependent cross-sections. The modeling includes simple geometry (SG), shape-based (SB), and voxel-based (VB) approaches. The three approaches use a piecewise uniform distribution of object characteristics to model an object.

With the SG model, an object is composed of a simple combination of primitives such as cylinders and spheres. The SB approach represents the boundaries of shapes by mathematical equations. Regular shapes such as sphere, cylinder, rectangular solid, etc. have been used to approximate irregularly-shaped regions. The VB approach discretizes an object into tiny cubes (voxels) with uniform characteristics. An object is thus represented by a union of voxels of the same size.

Extensions of SG and SB models such as the solid geometry-based (SGB) approach [59] includes more primitives (ellipsoids, elliptic cylinders, tapered elliptic cylin-

ders, rectangular solids, and their subsets: half, quarter, and eighth) and uses an inclusion tree data structure to provide relationships between primitives. These extensions provide simple irregular shape modeling. To allow anthropomorphic modeling the composite model which is an extension to the SGB approach adds to the primitives a voxelized rectangular solid primitive [60].

2.3.3.2 Anthropomorphic phantoms. Modeling of imaging and other medical applications is best done with phantom models that match the gross parameters of an individual patient. Computerized anthropomorphic phantoms can either be defined by mathematical (analytical) functions, or digital volume arrays.

The mathematical specifications for phantoms that are available assume a specific age, height and weight. However, people exhibit a variety of shapes a. In the first MIRD pamphlets, several organs including the skeletal system were represented schematically using geometric forms (cylinders, cones and ellipsoids). The representation of internal organs with this mathematical phantom is very crude since the simple equations can only capture the most general description of the organ's position and geometry. The most studied phantom is defined as the reference man weighing 70 kg.

Mathematical phantoms are still evolving and are being constantly improved. The heterogeneity of the body has been taken into account by including soft tissues, bone and lungs with different compositions and densities. For certain organs such as the stomach and the bladder, a distinction should be made between the organ contents and the organ wall. A revised head and brain model in which the neck and head are treated as two separate compartments was developed by Bouchet in 1996. The trunk region of the Snyder-Fisher phantom without its internal organs is incorporated into the model. Based on the atlas of sectional human anatomy, a 3D computer model of a human torso, including four cavities of the heart, two lobes of the lung and the body surface and a 3D model of the myocardium was developed by Sui and Shen in 1990.

The Mathematical Cardiac Torso (MCAT) phantom is an anthropomorphic

phantom, developed at the University of North Carolina at Chapel Hill, that has been used in emission computed tomography imaging research. Using mathematical formulas, the size, shape and configurations of the major thoracic structures and organs such as the heart, liver, breasts and rib cage are realistically modeled for imaging purposes [3].

2.3.4 Monte Carlo Computer Codes

Many Monte Carlo programs have been in use in the field of nuclear imaging and internal dosimetry with many of them available as open source codes in the public domain. Basically there are two categories of software packages: general purposes Monte Carlo codes developed for high-energy or general medical physics applications and dedicated software packages developed mainly and optimized for nuclear medicine imaging applications. These are highly sophisticated tools requiring advanced computer skills and familiarity with radiation transport theory. Each category has its own advantages and drawbacks; the motivations for the choice of a particular code being mainly dictated by availability of code and documentation, the user's needs, experience and computer skills.

2.3.4.1 General-purpose Monte Carlo Programs. Figure 2.10 lists widely used public domain Monte Carlo codes together with a short description of their key features. Most of the packages mentioned below run virtually on different platforms and operating systems and are available either directly from the developers or through the official channels (RSIC or NEA). The most popular computer codes developed specifically for medical physics applications are EGS4[61]/EGSnrc[62], ITS including (TIGER, CYLTRAN, ACCEPT)[63], MCNP[64]/MCNPX[65], GEANT[66], PENELOPE[67], FLUKA[68].

MC code	General description	Example references
EGS4[11]/EGSnrc[12]	Coupled photons/electrons transport in any material through user specified geometries. Simulation of nuclear imaging systems not specifically included and requires an extensive amount of user programming in Mortran.	13-22
ITS including TIGER CYLTRAN and ACCEPT[23]	Coupled photons/electrons transport in any material through slabs, cylinders or combinatorial. Simulation of nuclear imaging systems not specifically included and requires an extensive amount of user programming in Fortran.	
MCNP[24]/ MCNPX[25]	Coupled neutrons/photons/electrons transport in any material through user-generalised geometry. Simulation of nuclear imaging systems not specifically included and requires an extensive amount of user manipulation of input date files to model complex geometries.	26-29
GEANT[30,31]	Coupled photons/electrons transport in any material through combinatorial geometry. Simulation of nuclear imaging systems not specifically included and requires an extensive amount of user programming in C/C++.	32-34
PENELOPE[35,36]	Coupled photons/electrons transport in any material through combinatorial geometry. Simulation of nuclear imaging systems not specifically included and requires an extensive amount of user programming in C/C++.	37-39
FLUKA[40]	Coupled photons/electrons transport in any material through combinatorial geometry. Simulation of nuclear imaging systems not specifically included and requires an extensive amount of user programming in C/C++.	41

Figure 2.10 Key features of general purpose public domain Monte Carlo codes used in modelling nuclear medicine imaging systems[5].

2.3.4.2 Dedicated Monte Carlo Simulation Packages. Figure 2.11 lists popular and widely used dedicated Monte Carlo codes together with a short description of their key features. The computer codes developed by Dresser[69] and Beck[70] are among the oldest Monte Carlo programs developed specifically for modelling scintillation cameras. The latter was extensively used by the group of Duke University for scatter modelling, correction and image reconstruction through inverse Monte Carlo in SPECT[71]. Likewise, Keller and Lupton pioneered the modelling of cylindrical and multi-ring PET systems using the Monte Carlo method[72, 73]. SIMSET[74], SIMIND[75], MCMATV[76], PETSIM[77], EIDOLON[78], PET-SORTEO[79] are some of the Monte Carlo simulation packages widely used. Since SIMIND is utilized in this study, it will be described in more detail.

MC code	General description
SIMSET[51,52]	Photons transport in any material through voxel-based phantoms. Simulation of SPECT and PET imaging systems included. User modules written in C could be linked.
SIMIND[53,54]	Photons transport in any material through shape- or voxel-based phantoms. Simulation of SPECT imaging systems included. User modules written in Fortran could be linked.
Unnamed[55,56]	Photons transport in any material through shape-based phantoms. Simulation of SPECT imaging systems included. User modules written in Fortran/C could be linked.
MCMATV[57,58]	Photons transport in any material through voxel-based phantoms. Simulation of SPECT imaging systems included. User modules written in Fortran could be linked.
PETSIM[59,60]	Photons transport in any material through shape-based phantoms. Simulation of PET imaging systems included. User modules written in Fortran could be linked.
EIDOLON[49,50]	Photons transport in any material through shape-or voxel-based phantoms. Simulation of 3D PET imaging systems included. User modules written in C/ Objective-C could be linked.
PET-SORTEO[61]	Photons transport in any material through shape-or voxel-based phantoms. Simulation of 3D PET and transmission imaging systems included.

Figure 2.11 Key features of dedicated Monte Carlo codes used to simulate nuclear medical imaging systems.[5].

2.3.5 SIMIND

The Monte Carlo simulation code, SIMIND, describes a standard clinical SPECT camera and can easily be modified for almost any type of calculation or measurement encountered in SPECT imaging. SIMIND has been developed by Professor Michael Ljungberg.

The entire code has been written in FORTRAN-90 and includes versions that are fully operational on VAX-VMS, most UNIX platforms and on MS-DOS (Lahey LF90 compiler). The Monte Carlo program SIMIND is based on the use of uniformly distributed random numbers for modelling the random process of the different photon interactions. In short, the code works as follows: **photons emitted from simulated decay in the phantom are followed step by step towards the scintillation camera. SIMIND includes an accurate treatment of photon interaction in the phantom, a protecting layer and in the crystal of the detector. The simulation of back-scattering from light guides and photomultipliers is also included. Different types of collimators can be selected.** SIMIND can take

advantage of anthropomorphic voxel-based phantoms developed for simulating realistic imaging situations.

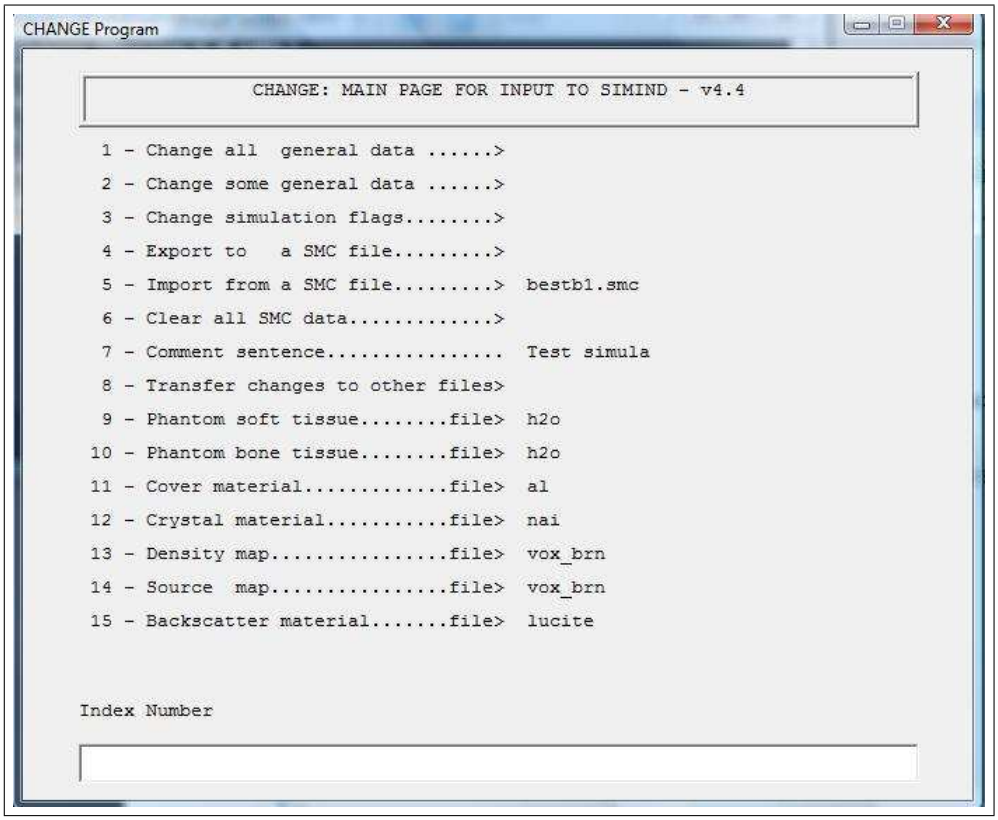

Figure 2.12 The **change** program [6].

The SIMIND system has two main programs, named **change** and **simind**. The **change** program enables the user to easily define the desired imaging system. **change** contains a series of menus that prompt the user to input parameters specific to the description of the system as shown in Figure 2.12. The actual Monte Carlo simulation is made by the program **simind** that reads input files created by **change** and outputs results to the screen or to different data files [6].

2.4 Compression in Medical Imaging

A mathematical model of an image is a positive function on a plane. The value of this function specifies the luminance or brightness at every point. For instance for nuclear medicine images the brightness is reflected by the number of counts of

quantum of gamma radiation, where as, for radiological or ultrasonic images, the grey levels estimate it. The digital image is the sampled version of such a function, where the values of the function are specified only at discrete locations on the image plane, known as pixels. In the meaning of linear algebra terms a digital image is a NxN matrix l(r,c). l(r,c) is the brightness of the image at the point (r,c) where r is an index of the row and c is an index of the column.

The value of the brightness at each pixel is represented by a pre-defined precision M. A typical value of precision equals 8 bits per pixel, but other values are admissible as well. The compression enables the prominent reduction of the image data bit rate. Furthermore, compression ratio is defined as:
(*bit rate for the original image*) / (*bit rate for the compressed image*).
Higher compression ratios indicate more compression [80].

2.4.1 The Role of Compression in Medical Imaging Systems

Digital image is represented by the large number of bits. Despite the advances in storage and transmission technology, useful and cost-effective systems require methods for reducing the amount of data associated with digital images. The goal of image compression is to find efficient representations in order to minimize the storage capacity and/or transmission times for a given application.

Decreasing transmission times achieve faster treatment of patient's critical needs and reduces the frustration level of the physician, as there is no longer substantial delay while an image is being sent [7].

2.4.2 Types of Image Compression

Image compression is largely a process of discarding information. Medical images often contain a significant amount of information that is redundant and/or irrel-

evant. Redundancy arises from the statistical properties of an image, and identified by:

- Spatial(between neighboring pixels) redundancy,
- Spectral(between color planes) redundancy, and
- Temporal(between adjacent frames in a sequence) redundancy

Redundant information may be removed from an image without affecting the ability to fully recover the original image data. Compression methods that allow exact recovery of the original image are termed **lossless compression**. It is the obvious choice for medical imaging applications because it does not affect image quality.

Irrelevancy refers to the limitations and sensitivity variations of the human visual system with respect to:

- Spatial frequency,
- Wavelength,
- Signal orientation, and
- Surrounding signals(i.e:masking effects)

Whether or not image information is irrelevant depends on the specific diagnostic task, viewing conditions, and individual observer sensitivity variations.

Compression methods that discard relevant information make it impossible to exactly recover the original image data, and the result is **lossy compression.** In this study I interested on this compression method. The advantage of lossy compression is that significantly higher compression ratios can be achieved as compared to lossless compression.

Lossy compression potentially affects the image quality. In this study I observed the loss of image quality with some metrics and so mathematical model observer is used for this purpose. In addition to that percebtible compression error are also crucial and it is a complex interaction of:

- Diagnostic task,
- Viewing conditions, and
- Physician preference.

For example small changes in anatomic structures or overall image sharpness may not affect the diagnostic utility of an image, but it may erode physician confidence in the diagnosis. For this reason it is easy to claim that to place hard limits on achievable compression ratios with lossy techniques is extremely difficult[7].

2.4.3 The Compression Standards

The first international compression standards were the Group3 / Group4 (G3/G4) facsimile standards, developed in 1980 and 1984 [81]. The American Collage of Radiology (ACR) and the National Equipment Manufacturers Association (NEMA) formed the Digital Imaging and Communications in Medicine (DICOM) committee. This committee and associated subcommittees have defined various protocols for exchanging medical image data and associated information, with compressed image data being an important part of this process. Working Group IV (WG IV) is the DICOM subcommittee that is responsible for evaluating and recommending image compression techniques to the main DICOM committee.

The Joint Photographic Experts Group (JPEG) standard is the primary technology within DICOM. A newly defined JPEG 2000 is another standard. In this study I compared these two techniques and observed that JPEG 2000 provide higher compression efficiency than the existing lossy JPEG technique.

Besides this a new lossless technique called JPEG-LS has been defined because of relatively poor compression efficiency of JPEG lossless method [7].

2.4.4 Basic Components of a Compression System

At the most fundamental level, a compression system consists of an **encoder**, which converts the original image to a compressed data representation, and a **decoder**, which reconstructs an image from the compressed data. In the case of lossless compression, the reconstructed image is identical to the original image, while in lossy compression the reconstructed image is an approximation to the original. Figure 2.13 shows general components in a compression system.

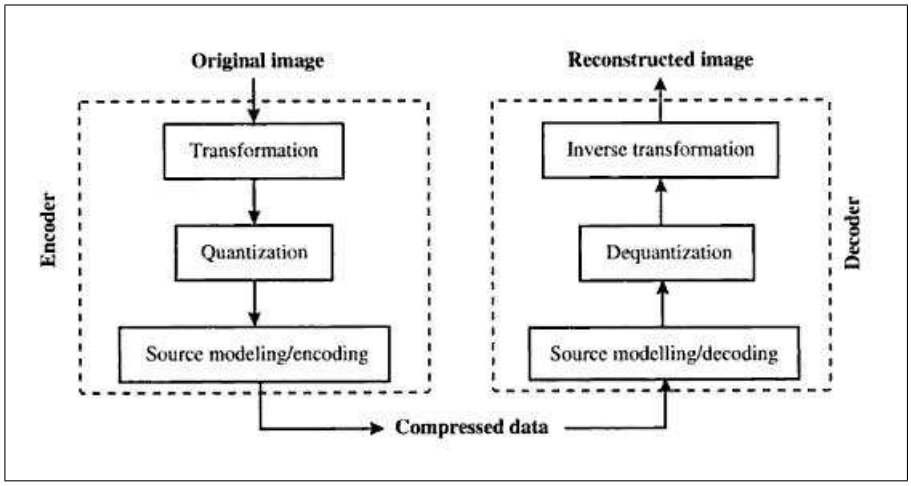

Figure 2.13 General components in a compression system[7].

2.4.4.1 Transformation. The task of the transformation is to map original pixel values into a representation that reduces redundancy and/or allows the limitations of the visual system to be incorporated in the compression process.

The S-transform was first described in 1977 as a decomposition method for lossless compression, and full-frame discrete cosine transforms were proposed in 1985 for lossy compression methods [82, 83]. These techniques have since given way to integer wavelet transforms and block-based discrete cosine transforms in the various

JPEG standards.

2.4.4.2 Quantization. The role of quantization is to map multiple input values into a single output value. It is the fundamental source of errors introduced during lossy compression and can be viewed as a control knob that trades image quality for compression ratio. In image compression systems, the process of quantization is often broken down into two parts: an encoder operation (the *quantization rule*), and decoder operation (the *dequantization rule*). The quantization rule specifies the partitioning of the input set, while the dequantization rule specifies the set of quantized output values. For a given input value, the quantization rule determines which bin of the partition it belongs to, while the dequantization rule determines the actual quantized value represented by that bin.

Different compression techniques have different quantization strategies such as *scalar quantization* and *vector quantization*. In scalar quantization, each input value is quantized seperately, while vector quantization jointly quantizes more than one input value. Scalar quantization is computationally more efficient than vector quantization and it is used in all current compression standards.

2.4.4.3 Source modeling/encoding. Transformation and quantization produce a sequence of symbols. The actually store or transmit the symbol sequence, it must be encoded into a binary representation, and this process is known as "source encoding"

The proper allocation of the bits requires accurate estimates for the symbol probabilities and this is the task of "source modeling"

2.4.5 JPEG standard

The JPEG standard for image compression is comprised of a toolkit that has three distinct components: baseline lossy, extended lossy, and lossless. Baseline lossy JPEG, the most widely implemented of the three, utilizes the discrete cosine transform (DCT) to decompose an image into sets of spatial frequency coefficients. The DCT is done on an 8 x 8 pixel block-adaptive basis. Baseline lossy JPEG supports 8 bits-per-pixel (per color) source imagery, offers a simple quantization scheme that enables users of the algorithm to trade off the degree of file size reduction, i.e., compression ratio, with image quality, and utilizes sequential Huffman entropy coding. Extended lossy JPEG is also based on the 8 x 8 pixel block-adaptive DCT. A feature available in extended JPEG that is critical for medical-imaging applications is the ability to handle source images with 12 bits-per-pixel. Other features available in extended JPEG include progressive and hierarchical encoding, variable quantization, and arithmetic entropy coding, however, these features are not widely supported. Lossless JPEG is an entirely separate system for image compression that is based on simple DPCM (differential pulse code modulation). A prediction value is formed for each pixel based on the values of neighboring pixels. The difference between the pixel value and the prediction value is then entropy coded using Huffman coding. Lossless JPEG can handle source images with up to 16 bits-per-pixel. The JPEG committee introduced an improved standard for lossless compression in 1997 that is known as JPEG-LS. JPEG-LS uses a more sophisticated context-based prediction algorithm and run-length encoding and has been shown to yield greater than 25% improvement in compression efficiency over lossless JPEG. JPEG-LS also provides a near-lossless feature that allows the a priori specification of a reconstruction error tolerance, i.e., $\pm$ 1, 2, 3, etc. maximum absolute code value difference between compressed-reconstructed version and the original. The near-lossless mode provides an intuitive option for trading off compression ratio with image quality degradation that may be appealing for some medical imaging applications [84].

2.4.6 JPEG 2000

JPEG 2000 is based on the two-dimensional DWT (discrete wavelet transform). The wavelet transform decomposes image signals based on scale or resolution, rather than the frequency content based decomposition resulting from the discrete cosine transform used in today's JPEG algorithm [85]. The signal is decomposed into a lower resolution signal together with a detail signal as shown in Figure 2.14 and is calculated using the steps below:

- Low-pass filter both image rows and image columns,
- Low-pass filter image rows and band pass filter image columns,
- Band-pass filter image rows and low pass filter image columns,
- Band-pass filter both image rows and image columns, and
- Down-sample by a factor of two in both image row and image column dimensions

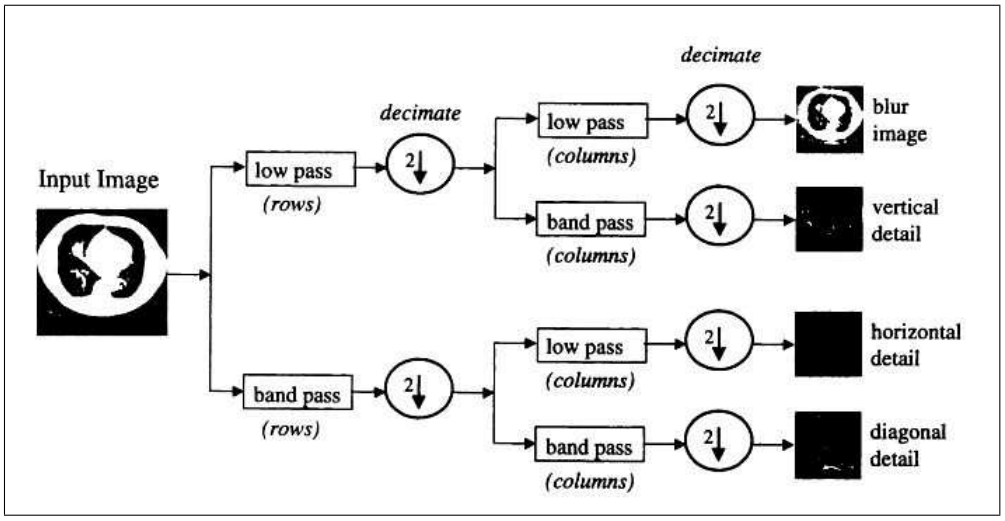

Figure 2.14 Steps in a one-level wavelet decomposition along the x and y axes of a chest CT scan[8].

The first image, which is obtained by applying the low-pass filter to the rows and columns in the original data set, is essentially a blurred representation of the original image. The remaining "detail" images contain directionally sensitive information that

is missing from the "blur" image. To perform higher level decompositions, the filtering procedure is repeated by using the previously generated blur image as input for the next level of decomposition [8]. Figure 2.15 provides a block diagram of this process, and Figure 2.16 is an example of a three-level decomposition applied to a simulated nuclear medicine image.

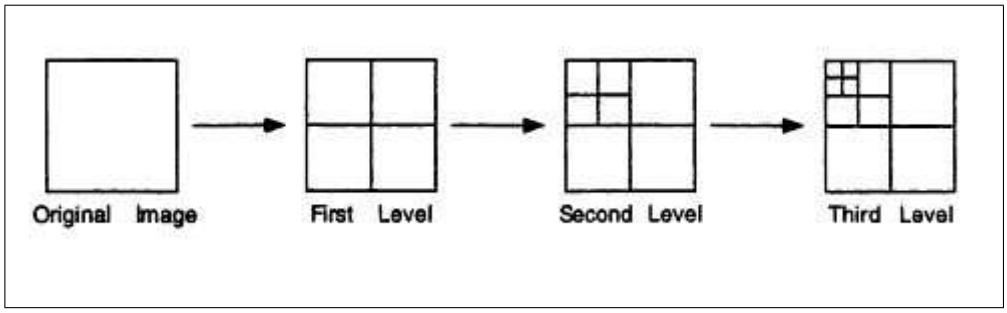

Figure 2.15 Block diagram depicts a three-level wavelet decomposition of an image[8].

Figure 2.16 Wavelet decomposition applied to simulated nuclear medicine image.

Like the DCT, the DWT effectively concentrates the image energy into relatively few coefficients in the transform domain. The JPEG 2000 base standard offers two choices of wavelet filters, the Daubechies 9/7 floating point filter because of its superior image quality performance, and the Integer 5/3 for low complexity and lossless applications[85]. JPEG 2000 (Part 1) quantization is performed using a scalar quantization strategy. The coefficients contained within each subband are scaled by a specified constant value, i.e., quantizer step size. The quantizer step sizes can be inde-

pendently optimized (weighted) for each subband, based on image viewing conditions and contrast sensitivity considerations. The quantized coefficients are progressively coded from the most significant to least significant bit. This coding strategy enables progressive transmission-by-quality, also known as signal-to-noise-ratio (SNR) scalability. A property of SNR scalability is that the bit-stream can be terminated at any point and the image that is produced is identical to the image that would have been produced had the image been compressed to the bit rate corresponding to the truncated bit stream. For an image that has been lossless compressed, the SNR scalability represents a progressive lossy to fully lossless decompression capability from a single code stream. In fact, JPEG 2000 allows for a reconstructed version of the image to be generated from the lossless compressed version at any specified spatial resolution or image quality level [84].

Other capabilities, which are included as part of JPEG 2000, include region-of-interest decoding and handling of source images with bit depth of up to 16 bits-per-pixel. Extended JPEG is limited to source images with 12 bits-per-pixel. Perhaps the key advantage of JPEG 2000 compression over JPEG is the flexibility afforded by the data representation resulting from the wavelet transform and embedded coding [84].

2.4.7 Selected Compression Software

The Vc image and video compression learning tool is a fully menu-driven package. It is operated by selecting compression techniques and parameters using buttons. In most cases we can run Vc without any further explanations starting from the main application window.

The purpose of Vc is to be able to experiment with different (sometimes very complex) image compression algorithms without bothering about their actual implementation. For this reason Vc is menu driven, and allows the user to experiment with different parameters that define the specific compression operations. On one hand visualization of image compression results will help to gain insight in "how good" a

compression algorithm performs. On the other hand the compression results will stimulate a problem-solving attitude. A generally effective attitude toward using Vc is asking yourself all the time the questions what will happen given a certain combination of parameters, what is the cause of a certain compression artifacts, and how do compression techniques compare visually and numerically.

Vc is a tool assisting the learning process, but does in itself not explain the compression techniques. The Vc software, including sample images and sequences, can be downloaded from *http : //ict.ewi.tudelft.nl/vcdemo* [86]. The program has the below modules;

- SS Subsampling of images,
- PCM Pulse-coded modulation coding of images,
- DPCM Differential pulse-coded modulation coding of images,
- VQ Vector quantization of images,
- FRAC Fractal image coding,
- DCT DCT-based transform coding of images,
- JPEG JPEG image compression standard,
- SBC Subband (wavelet) coding of images,
- EZW Embedded zero-tree wavelet coding of images,
- SPIHT Set partitioning in hierarchical trees coding of images,
- JPEG2000 JPEG-2000 image compression standard,

2.5 The Evaluation of Image Quality with Classical Metrics

It is natural to raise the question of how much an image can be compressed and still preserve sufficient information for a given clinical application. This section

discusses some parameters used to measure the trade-off between image quality and compression ratio.

Compression ratio is defined as the nominal bit depth of the original image in bits per pixel (bpp) divided by the bpp necessary to store the compressed image. For each compressed and reconstructed image, an error image was calculated. From the error data, mean square error (MSE), signal to noise ratio (SNR), and peak signal to noise ratio (PSNR) were calculated.

MSE is the cumulative squared error between the compressed and the original image and defined by

$$MSE = \frac{1}{MN} \sum_{x=1}^{M} \sum_{y=1}^{N} \Big[f(x,y) - f^*(x,y) \Big]^2 \tag{2.7}$$

where f(x,y) is the original image data and $f^*(x,y)$ is the compressed value. M and N are the matrix dimensions in x and y respectively.

SNR is the measure of the error and the mathematical formula is defined by

$$SNR = 20 \ \log \left\{ \frac{\sum_{x=1}^{M} \sum_{y=1}^{N} f(x,y)^2}{\sum_{x=1}^{M} \sum_{y=1}^{N} \Big[f(x,y) - f^*(x,y) \Big]^2} \right\} \tag{2.8}$$

Here, the "signal" is the original image, and the "noise" is the error in reconstruction.

Finally From the MSE, the Peak Signal-to-Noise Ratio (PSNR) is computed from the PSNR image in decibels (dB), as follows:

$$PSNR = 10 \ \log \left\{ \frac{MAXp^2}{MSE} \right\} \tag{2.9}$$

where $MAXp = (2^B - 1)$ and B is the image bitdepth. For example MAXp is defined as 255 for image with 8 bpp. Typical PSNR values are between 20 dB and 40 dB. The absolute value is not significant, but the comparison between two values for several compressed images gives a relative quality measure [87, 88, 89, 90].

A lower value of MSE means lesser error, and as MSE and SNR have an inverse relationship this translates to a higher value of SNR. Logically, a higher value of SNR is good because it means that the ratio of original image to error in reconstruction (noise) is higher. So if you find a compression scheme having a lower MSE (and a high PSNR) you can recognize that is a better one.

In the first part of my study, I compared the JPEG and the JPEG 2000 compression algorithms on simulated smallest lesion in breast that is modelled as a sphere in the centre of the cylinder. The simulated 8bpp images are then compressed to different bitrates and for each compressed condition MSE, SNR, and PSNR are measured and compared in terms of different compression algorithms.

2.6 Detection of Simulated Lesions on Simulated Compressed Breast Scintigraphic Images

The most commonly used measurements of image quality, such as MSE or PSNR are not adequate for medical images.

Medical image quality can better be measured by human performance in visual tasks that are relevant to clinical diagnosis. The standard method of evaluating diagnostic methods is a receiver operating characteristic (ROC) study, which is time consuming and costly because it requires a large number of human observations.

Computer model observers are algorithms that attempt to predict human visual performance in noisy images and might represent the desired metric of image quality when the diagnostic decision involves a human observer and a visual task. Among all the model observers, the ideal observer sets an upper bound to the performance of any observer.

In the second part of my study we presented a general methodology for evaluat-

ing the signal detection capabilities on compressed scintigraphic images and discussed the effect of detected total count rates on these simulated compressed images. To illustrate the technique, a study was performed of a monte carlo simulation package SIMIND for the task of detecting different lesion types within human breasts.

2.6.1 Signal Detection Theory

Signal-detection theory is a form of hypothesis testing in which the hypothesis H_1 is that a signal is present and the alternative hypothesis H_0 is that it is absent. Using the available data, an observer decides, with some degree of error, whether H_1 or H_0 is true. For example, in tumor detection, the H_0 hypothesis is that the image data was taken of a patient who does not have a tumor, while H_1 is that the image data was taken of a patient who does have a tumor. Under this framework, the imaging chain is mathematically represented as,

$$\begin{aligned} H_1 &: g = H(f + t) + n \\ H_0 &: g = Hf + n \end{aligned} \tag{2.10}$$

In these equation f represents the normal, non-tumor portion of the anatomy while t represents the signal, or tumor portion of the object, n is the noise in the system (which may depend on f), H is an operator that describes how the imaging system maps the continuous object to discrete data, and g is the noisy image data returned by the imaging system. In general, both of these functions are stochastic, i.e., they vary randomly from one patient to the next. The observer's performance depends on the signal, the background, and the detector system. A more knowledgeable observer, or an observer that has a priori knowledge of one or more of these factors, can be expected to make decisions with a lower rate of error.

Signal-detection theory may be applied in a wide variety of situations that involve the task of determining whether or not a signal is present in a noisy background. For example, in clinical nuclear medical imaging, the signal could be represented by a

lesion within a patient's body, the data could be a set of medical images of the patient, the observer could be the attending physician, and the decision could be the physician's diagnosis as to whether the lesion is present or not. The physical shape, histology, and location of the lesion as well as the nature of the surrounding tissue add complexity to the detection task. In this study we simulate the aforementioned example. The signal is a simulated radioactive lesion in a homogenious background with different radioactive ratio, the data are original and reconstructed compressed images. Original images are simulated background images with lesion and without lesion and the reconstructed images are the irreversibly compressed version of the original images. The observer is a machine (namely, a computer executing a data analysis program), and the decision as to whether or not the signal is present is based on the calculated value of a test statistic relative to a specified threshold.

2.6.2 Data

In this study the data consist of a set of simulated original and reconstructed images (irreversibly compressed to different bitrates), each of which contains a random noise background and a possible signal. Each simulated image consists of a set of pixel values $\{g_m, m = 1, ..., M\}$ that are ordered as an M x 1 vector g. The noise in the pixel values is Poisson in nature and, hence, dependent on the object. The signal, however, has very low contrast with respect to the background and only slightly perturbs the mean background pixel values, so the noise is assumed to be independent of the signal.

2.6.3 Observer

An observer that can perform the task is needed. This can be a human or a model observer. It is the human observer (radiologist) that is the final decision maker. Therefore, measures of image quality should always take the human observer into account. Yet, clinical trials involving human observers are costly and time demanding. Model observers may then be used to give insights into how image quality depends on

the physical and technical image acquisition parameters [91].

The observer used in this study is a channelized version of the ideal linear observer. An ideal observer is one who optimally uses all of the information in the data and is therefore one whose performance cannot be surpassed. The ideal linear observer, also known as the Hotelling observer [92, 93, 94], is one that is constrained to perform only linear operations on the data but is otherwise optimal in the sense of maximizing a detectability measure. A channelized Hotelling observer is one that performs optimal linear operations on data that have been processed by a relatively small number of linear operators called channels. The channels serve to greatly reduce the dimensionality of the data set and make it much more feasible to find the optimal linear discriminant.

The original motivation for the channelized Hotelling observer was to mimic the spatial frequency-selective channels in the human visual system and thereby provide a mathematic model observer that accurately predicted human detection performance, even when the human could not perform as well as the true Hotelling observer. We have recently recognized, however, that with proper choice of channels a channelized Hotelling observer can give an accurate estimate of the performance of the ideal linear observer, in spite of the channels [95]. The key is to make use of prior knowledge of the signal and the background statistics in choosing the channels. In particular, we may know the signal location and know that both the signal and the background correlations are rotationally symmetric, and we can build that knowledge into the channels.

2.6.3.1 Laguerre-Gauss Channelized Hotelling Observer Model. To explain the mathematic form of the channelized observer used in this study, we begin with the ordinary Hotelling observer. This observer computes a linear functional of the data, often referred to as the Hotelling test statistic, that accounts for randomness in the signal or the background. This scalar test statistic λ can be written as:

$$\lambda = \sum_{m-1}^{M} w_m g_m = \mathbf{w}^t \mathbf{g} \tag{2.11}$$

where **w**, called the Hotelling template, is an M x 1 vector of weights and the superscript t denotes transpose. For signal-known-exactly (SKE) studies in which the noise is considered to be independent of the signal, the Hotelling template is:

$$\mathbf{w} = \mathbf{K}^{-1}\Big(\langle g\rangle_1 - \langle g\rangle_0\Big) = \mathbf{K}^{-1}\mathbf{s} \tag{2.12}$$

where **K** is an M x M matrix containing the data covariances, $\langle g\rangle_1$ and $\langle g\rangle_0$ are the mean signal-present and signal-absent data vectors, respectively, and **s** is an M x 1 vector containing the expected signal. In our model **K** includes the effects of both measurement noise (i.e., Poisson noise), compression noise and randomness in the background (i.e., anatomic variations).

A channelized observer is often used when the dimensions of the sample images necessitate inverting a very large **K** or the number of available sample images is too small to reasonably estimate **K**. Suppose that a sample image has dimensions of N x N. Then $M = N^2$ and **K** has dimensions N^2 x N^2. The process of forming a sample **K** would require a minimum of N^2 sample images to ensure that the matrix is not singular and about 10-100 times N^2 sample images to ensure that the matrix elements are stable. The problem of performing calculations with an N^2 x N^2 matrix and collecting 10-100 times N^2 sample images quickly leads to rather impractical computational situations.

Channels offer a solution to the problems outlined above by providing a means of reducing the size of the sample **K**. In essence, instead of working with the original image pixel values, one works with some functions of the pixel values. By definition, a channel is any template U_n of the same size as an image. Analogous to linear features in the field of pattern recognition, a channel output is any linear functional of the data **g** in the form:

$$\nu_n = U_n^t\mathbf{g} = \sum_{m=1}^{M} U_{nm}g_m \tag{2.13}$$

where ν_n is the output of the nth channel. If 5 channels are used, then each image **g** produces a set of 5 channels outputs that, when expressed as a 5 x 1 may be written

as:

$$\nu = \mathbf{U}\mathbf{g} \tag{2.14}$$

where **U** is a 5 x M matrix with elements U_{nm}. A diagram of the channelized observer is shown in Figure 2.17. The channelized observer does not interpret the image vector **g** directly, but though a series (U_1, U_2,..., U_n) of channels as shown in the diagram.

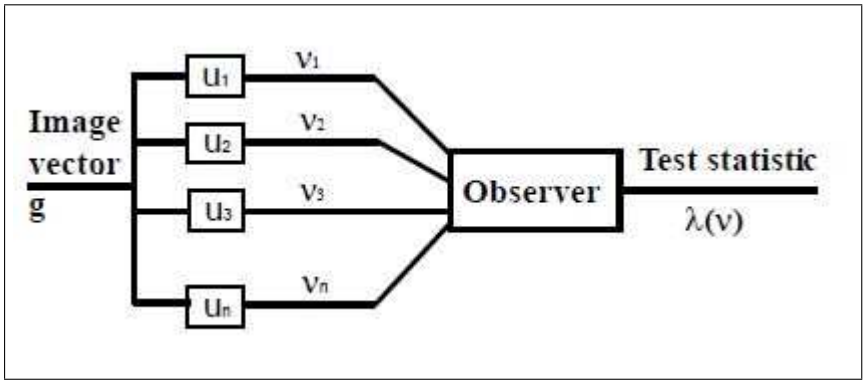

Figure 2.17 Diagram illustrating the channelized observer.

We would like to choose channels such that ν is a sufficient statistic for the signal-detection task, meaning that the channel outputs will serve as well as the original image pixel values for performing the signal-detection task. In this study we know specifically (a) that the signal is rotationally symmetric and (b) the exact location of the signal. So we would like the channels to be a set of functions that are rotationally symmetric and have a known location.

We have chosen channels were the 0th - 4th orders of the Laguerre-Gauss family of functions centered on the signal location. A Laguerre-Gauss function is a Laguerre polynomial times a gaussian envelope. As required, the Laguerre- Gauss functions possess 2 features-rotational symmetry and a known location-that are also features of the signal. Gallas et al. provided the detailed validation of Laguerre-Gauss channels as an estimate of Hotelling observer performance[96]. Ullman et al. developed methods for assessment of image quality in simulations of projection radiography by using Monte Carlo (MC) simulation methods. In his study the measures of image quality derived from the Laguerre-Gauss (LG) Hotelling observer are found to correlate relatively well

with the radiologist's assessment of image quality[91]. we use the individual Laguerre-Gauss functions as rotationally symmetric basis functions to synthesize a Hotelling template that is rotationally symmetric, is centered at the signal location, and has a width approximately equal to that of the signal. The channelized Hotelling template is:

$$\mathbf{w_c} = \mathbf{K_c^{-1}} \mathbf{s_c} \tag{2.15}$$

where, if you use H channels, $\mathbf{K_c}$ is the H x H covariance matrix of the channel outputs and $\mathbf{s_c}$ is the signal as seen through the channels. Then finally the corresponding channelized Hotelling test statistic is:

$$\lambda_c = \sum_{m=1}^{M} w_{c,m} \nu_m = \mathbf{w_c^t} \nu \tag{2.16}$$

where, as noted earlier, ν is a sample image as seen through the channels.

Thus, given the channelized template $\mathbf{w_c}$ and channelized sample images ν, the channelized observer makes a decision by computing the scalar test statistic λ_c and comparing it to a threshold $\lambda_{c,th}$, deciding that H_1 is true if $\lambda_c > \lambda_{c,th}$ or that H_0 is true if $\lambda_c \leq \lambda_{c,th}$.

2.6.3.2 Figures of Merit. One means of specifying how well an observer can distinguish between H_1 and H_0 is to calculate a signal-to-noise ratio (SNR) defined by:

$$SNR^2_{\lambda_c} \equiv \frac{\left[\langle \lambda_c \rangle_1 - \langle \lambda_c \rangle_0\right]^2}{\left[1/2\ var_1(\lambda_c) + 1/2\ var_0(\lambda_c)\right]} \tag{2.17}$$

where $\langle \lambda_c \rangle_i$ and $var_i(\lambda_c)$ are the mean and variance of the test statistic for group i and where subscript 1 indicates signal present, and subscript 0, signal absent. When plotted in a histogram the channelized hotelling test statistics fall into two groups (signal-present and signal-absent). The differentiability of the two groups is a measure of the system's ability to detect the tumor [95].

This $SNR^2_{\lambda_c}$ is a figure of merit which determines how well imaging systems discriminate between normal and abnormal subjects.

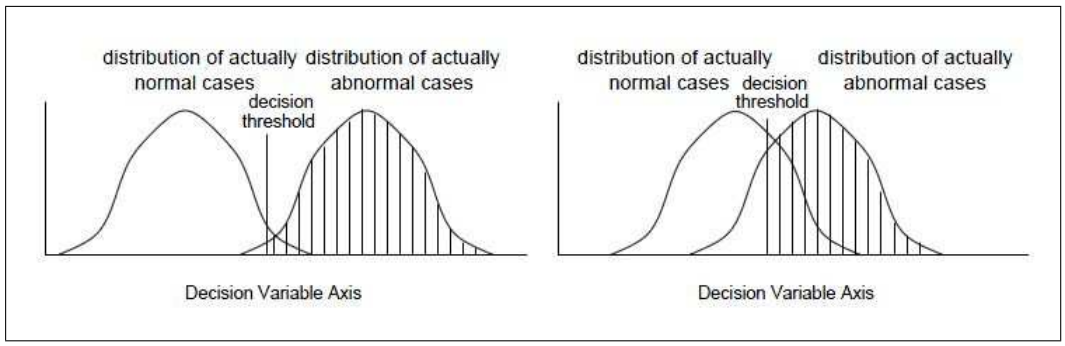

Figure 2.18 Distribution of a test statistic.

Figure 2.18 is an example of the distribution of test statistics for two compression conditions. For each compression ratios, distributions of actually normal and abnormal cases are plotted against the decision variable axis. The system on the left has a higher SNR_{λ_c} because it is easier to separate abnormal from normal cases. The system on the right produces two populations with a high degree of overlap. Therefore, it is more difficult to make an accurate decision. The SNR_{λ_c} is low [97].

The quantity SNR_{λ_c} is also referred to as the detectability index and is denoted by d'. Another means is to measure the area under the receiver-operator-characteristic (ROC) curve. If λ_c is normally distributed under both hypotheses, then $SNR^2_{\lambda_c}$ is related to the area under the curve, denoted as AUC, by:

$$AUC = \frac{1}{2} + \frac{1}{2}\, erf(\frac{1}{2}\, SNR_{\lambda_c}) \tag{2.18}$$

where $erf(.)$ is the error function. As we mentioned above another means of specifying an observer's performance is the detectability index and it is equivalent to SNR_{λ_c} if the test statistics λ_c is normally distributed[98]. This study presents the observer performance in terms of AUC which is calculated from SNR_{λ_c} or detectability index for original and several compressed images. The AUC is in the range [0.5, 1], where higher values of the AUC indicate better CHO performance for the lesion detection task. If the AUC = 1, then the CHO always detects the lesion, regardless of the decision threshold. On the other hand, if the AUC=0.5, then for any threshold, TPF=FPF, and the CHO

performs no better than arbitrary guessing.

3. MATERIALS AND METHODS

This thesis consists of two main parts. In the first part, the JPEG and the JPEG 2000 compression algorithms are compared on simulated subtle lesion in breast that is modelled as a sphere in the centre of the cylinder. The simulated 8bpp images are then compressed to different bitrates and for each compressed condition MSE, SNR, and PSNR are measured and compared in terms of different compression algorithms. In addition to that the effect of higher and lower total detected count rate on image is compared in terms of their different compression standards.

The methodology of the first part of study as shown in the Figure 3.1 and it works as follows:

- A planar gamma camera system is simulated via SIMIND with collimator parameters are selected in according to the values that are found on robust design of breast scintigraphy collimator[99]. The given radioactivity rates are determined according to the total detected counts on the image. Two different simulations are made; one for the background and one for the lesion. A binary matrix image is created by the output of SIMIND (*.bim file).

- The output of each simulation is created by superimposing the two separate *.bim files. A written MATLAB code generates a resultant image, then high and low detected counts are calculated per image. These generated images are then converted to the 8-bit gray level image in tiff format.

- After that the two compression standards JPEG and JPEG 2000 are employed to these original images by means of Vc compression software. The reconstructed images are saved in terms of different compressed bitrate or compression ratio for higher and lower number of detected counts.

- Then finally the image quality metrics (MSE, PSNR, SNR) are calculated between the original and reconstructed images and the effect of detected total counts

are discussed.

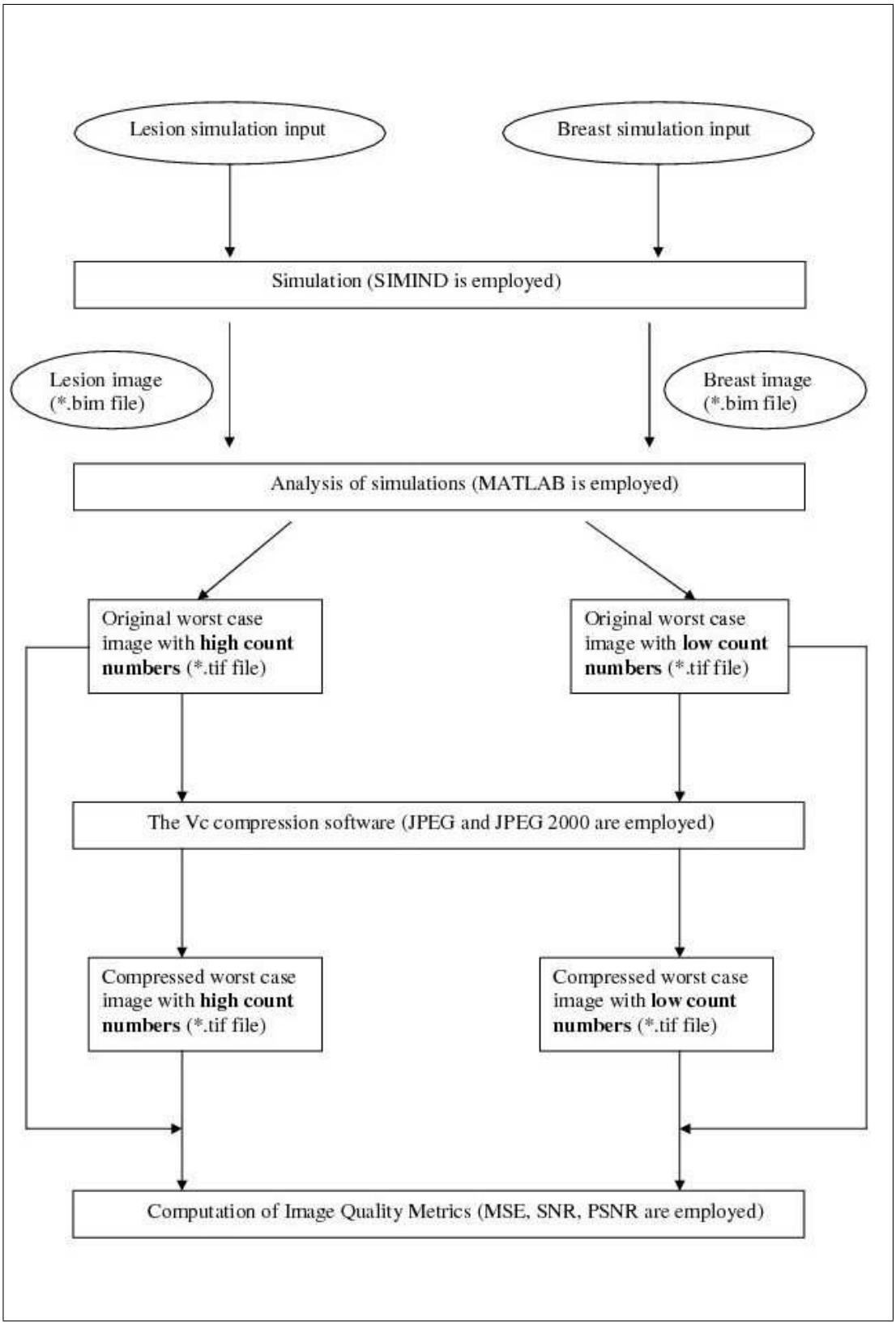

Figure 3.1 the methodology for the first part of study.

In the second part of the study we presented a general methodology for evaluating the signal detection capabilities of compressed scintigraphic images and discussed the effect of higher and lower number of total detected counts on these simulated compressed images. To illustrate the technique, a study was performed of a monte carlo simulation package SIMIND for the task of detecting different lesion types within human breasts.

The methodology of the second part of study as shown in the Figure 3.2 and it works as follows:

- A planar gamma camera system is simulated via SIMIND with collimator parameters are selected in according to the values that are found on robust design of breast scintigraphy collimator[99]. The total detected counts on the image can be determined according to the given radioactivity rates. 100 different lesion simulation inputs are given to the SIMIND for each best case, typical case, and worst case conditions. In addition to that 100 different background simulation inputs are given to the SIMIND for each best case, typical case, and worst case conditions. Binary matrix images is created by the output of SIMIND (*.bim file).

- The output of each simulation is one for lesion present image and the other is lesion absent image. The lesion present images are created by superimposing the two separate *.bim files. 100 different simulated lesion absent and lesion present images are created with adding poisson noise on 8-bit gray level in tiff format for each best case, typical case, and worst case conditions. In addition to that all generated images are grouped in terms of detected counts on images.

- After that the compression standard JPEG 2000 are employed to these lesion present and lesion absent images by means of Vc compression software for each best case, typical case, and worst case conditions. The reconstructed images are saved in terms of different compressed bitrate or compression ratio for higher and lower number of detected counts.

- Then mathematical model observer calculates AUC on each compression ratio for each case. Finally the effect of total detected counts on image with respect to different compression ratio for the same case is calculated and compared.

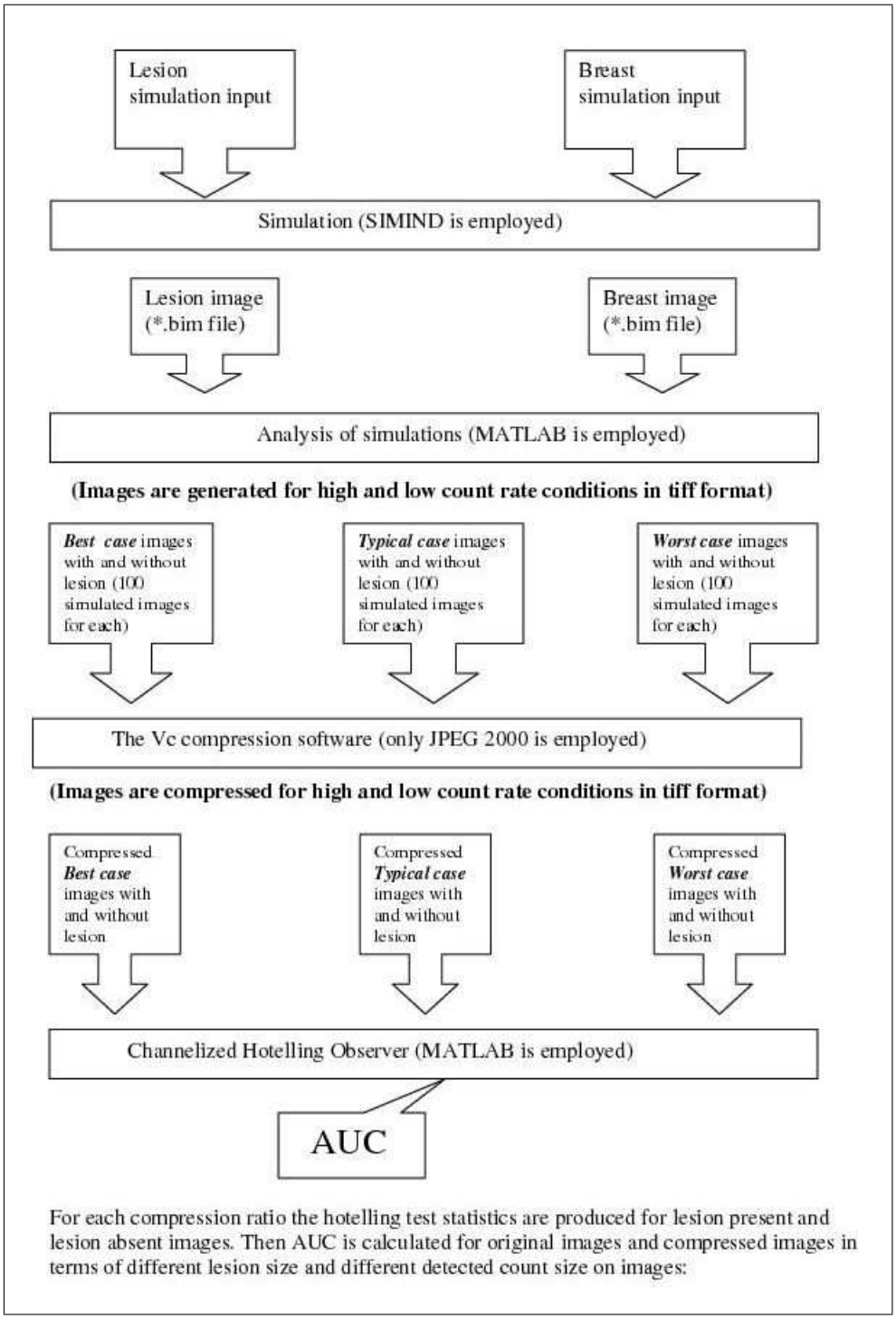

Figure 3.2 the methodology for the second part of study.

3.1 Model of the Breast and Lesion

The gamma camera for breast scintigraphy should be equipped with a low-energy, high-resolution collimator. In literature, there is an interesting study about designing a new collimator for breast scintigraphy. In this study a robust parallel hole collimator is designed for the improvement of the system's lesion detection capability especially for the diagnosis of lesion smaller than 1cm [99]. The configuration of the collimator is described by three variables(hole length, hole size, and septal thickness). Sinem et al optimized these three variables for better lesion detection. A hole length of 1.74cm, a hole size of 0.14cm and a septal thickness of 0.02cm were obtained as the robust collimator parameters. I used these collimator parameters in my study because the robust collimator enables us to better lesion detectability with respect to other commercial collimators. Sinem et al showed that the resultant image of the SIMIND simulation with robust collimator gives the clearest image.

In this study three different patient parameter sets including the hardest, the easiest, and the moderate situations of lesion detectability are used. In the first part of experiment only one patient parameter is sufficient for simulation to obtain image since this part includes only to compare the JPEG and JPEG 2000 compression standards and the effect of detected counts on compression algorithms. The second part of experiment depends on the compression with subtle lesion so size and detection of lesion is crucial for this study.

3.2 The First Set of Experiments

In the first part of experiment the breast is modeled as a cylinder filled with ^{99m}Tc with a density of 100μCi/cc and water. It has the dimensions of 7cm height and 12cm diameter. The volume of the breast is 791.28cc. The lesion is modeled as a sphere located at the center of the cylinder breast model. The lesion is assumed to be composed of water and ^{99m}Tc with a density of 564μCi/cc and have a diameter

of 0.5cm. The volume of the lesion is 0.065417cc. The reason why this ^{99m}Tc concentration ratio (5.64:1) is used for the breast and the lesion models is, the studies showing that the typical radioactivity ratio of malignant lesion to the radioactivity of the breast tissue is of this measure [100]. The experiment (simulations) is achieved by a Monte Carlo Simulation program called SIMIND. Two different simulations are accomplished; one for lesion, and one for breast source. Then, these two simulated images are superimposed by MATLAB.

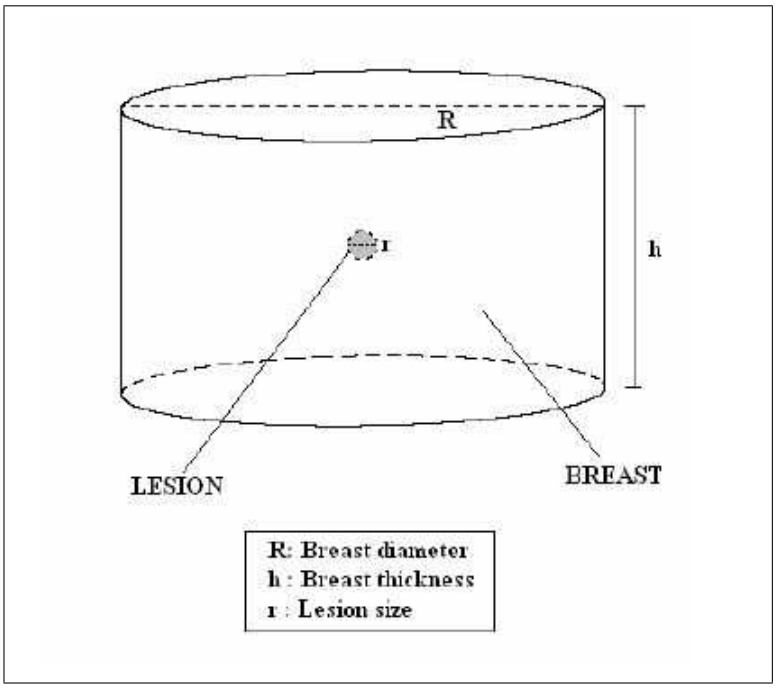

Figure 3.3 Model of the phantom

Simulation parameters of breast and lesion are shown in Table 3.1 and in Table 3.2 respectively.

Table 3.1
Simulation parameters of breast

Photon energy	140 keV (^{99m}Tc)
Energy resolution	10.6% at 140 keV
Intrinsic resolution	0.380cm
Crystal length	40cm
Crystal width	50cm
Crystal thickness	0.935cm
Source dimensions	12x12x7cm (Cylinder)
Phantom dimensions	12x12x7cm (Cylinder)
Source activity	2927.7 MBq
Source to camera distance	4 cm (from the center of the phantom)
Energy window	10% (126 keV-154 keV)
Pixel size	0.1cm
Image matrix size	128x128
Collimator Hole Shape	Hexagonal
Simulated photons	1000000

Table 3.2
Simulation parameters of lesion

Photon energy	140 keV (^{99m}Tc)
Energy resolution	10.6% at 140 keV
Intrinsic resolution	0.380cm
Crystal length	40cm
Crystal width	50cm
Crystal thickness	0.935cm
Source dimensions	0.5x0.5x0.5cm (Sphere)
Phantom dimensions	12x12x7cm (Cylinder)
Source activity	1.365 MBq
Source to camera distance	4 cm (from the center of the phantom)
Energy window	10% (126 keV-154 keV)
Pixel size	0.1cm
Image matrix size	128x128
Collimator Hole Shape	Hexagonal
Simulated photons	1000000

The collimator parameters that are entered the SIMIND program is shown in figure 3.4

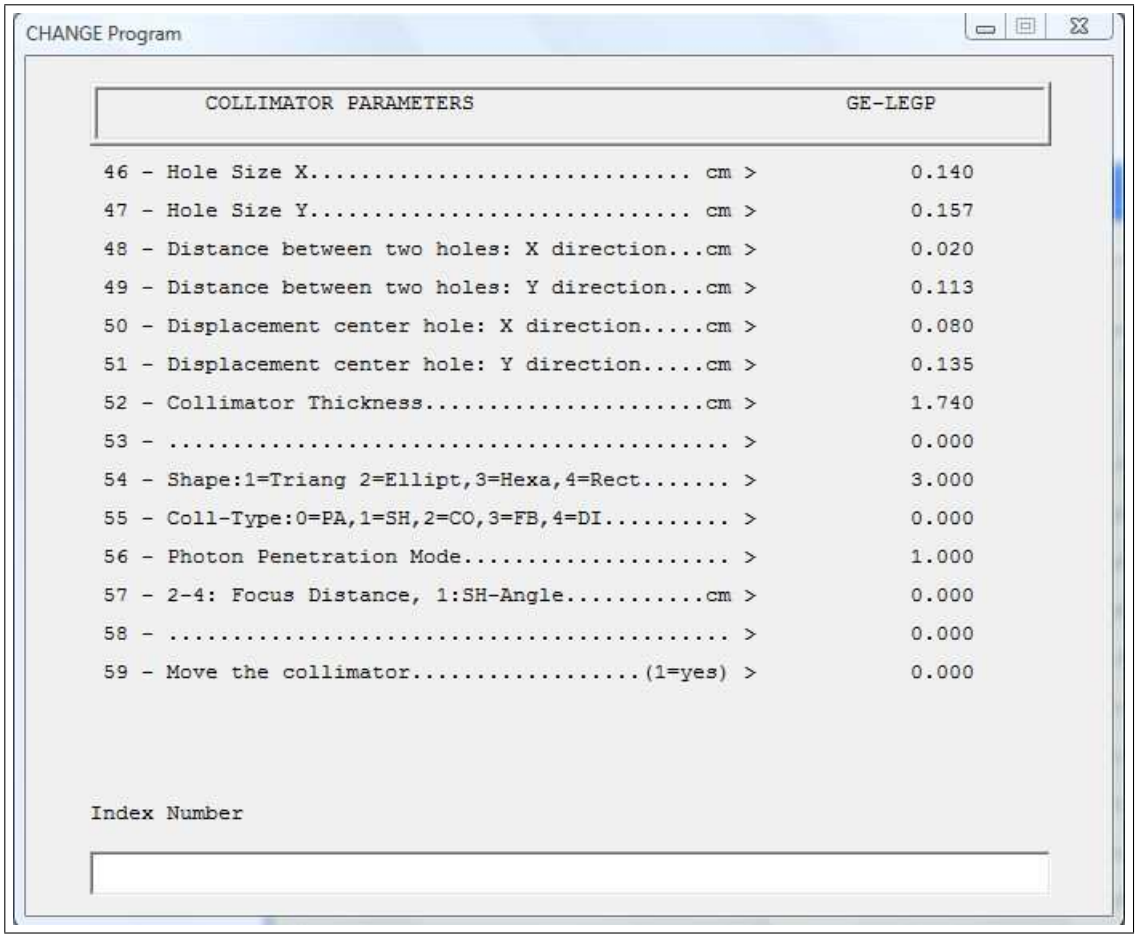

Figure 3.4 A screenshot from the SIMIND program

After MATLAB is employed two types of images are generated, one for higher detected counts and the other lower detected counts. The total detected counts are approximately 580.000 for maximum condition and 115.000 for minimum condition. The generated images original images are shown in Figure 3.5. The total detected counts are lower on the left side image, however are higher on the right side image. The information density for higher detected counts image is about 51.2833 counts per pixel and for lower detected counts image it is 10.1682 counts per pixel.

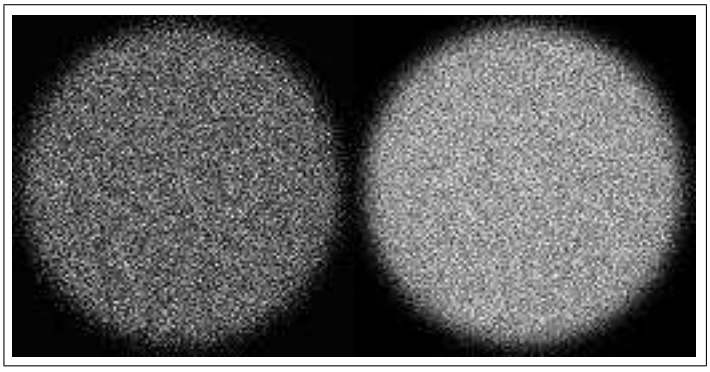

Figure 3.5 Simulated images with high detected counts (the right one) and low detected counts (the left one).

3.2.1 JPEG Compression

From the point of view of interoperability, lossy JPEG compression and lossy JPEG 2000 compression are desirable compressions at the moment. Lossy JPEG compression based on the discrete cosine transform (DCT) is the past and current still image compression standard. On the other hand, lossy JPEG 2000 compression based on the discrete wavelet transform (DWT) is the current and future still image compression standard.

Compression Algorithm: The JPEG compression module implements the full JPEG compression standard. Several optimization options can be selected. The module writes a jpeg file to disk (in the user output directory), which can be viewed with any JPEG viewer.

Bit rate: The JPEG quality factor Q can be set here. By selecting the quality factor, the bit rate is implicitly defined, but the bit rate is not known beforehand. Instead of setting the quality factor, a bit rate can be selected. The quality setting corresponding with this bit rate will be determined by a simple search procedure.

The images are compressed from 8bpp to 0.1bpp irreversibly and they are shown in Figure 3.6 as compressed images with low information density. The original image is named as uint8 and the compressed images are placed with increasing bit rate from

top left to bottom right. These are also same for image which has high information density as shown in Figure 3.7.

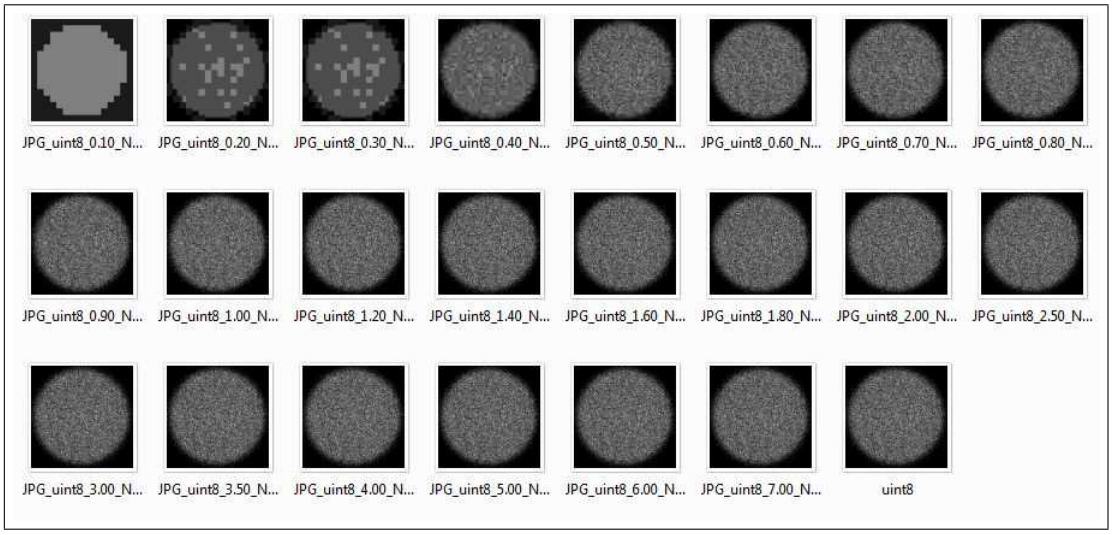

Figure 3.6 Compressed images with low detected counts by means of JPEG

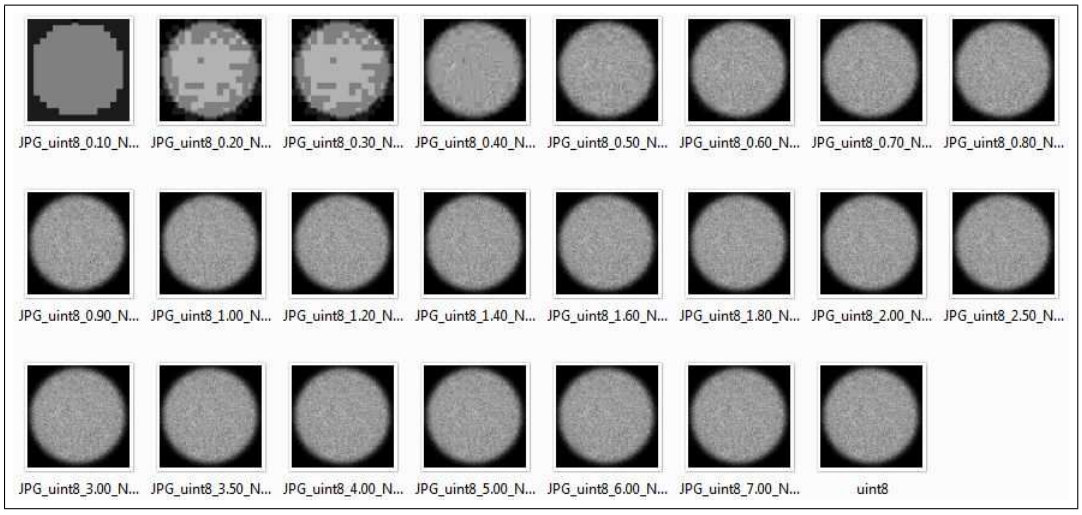

Figure 3.7 Compressed images with high detected counts by means of JPEG

3.2.2 JPEG 2000 Compression

The JPEG2000 compression module implements the JPEG2000 image compression standard. The implementation is based on JPEG2000 verification model 7.1. The bit stream is continuously scalable, which means that the decoder can read the first N bits to decode the image at rate $N/(rows \times columns)$ bit per pixel.

Encode: The encoder bit rate can be selected. Depending on the selected encoding bit rate, a range of decoding bit rates becomes available.

Decode: The decoder bit rate can be selected. Depending on the selected encoding bit rate, a range of decoding bit rates is available.

SNR layering: The compressed data is organized such that the bits (i.e. wavelet coefficient/bit planes) that contribute most to the quality of the image (expressed in SNR) are included first in the bit stream. Therefore, truncating the stream will give a larger SNR than without SNR layering. Number of resolution levels determines how often the low frequency band of wavelet coefficients is split.

The lossy JPEG 2000 compressed images that have low information density as shown in Figure 3.8 and high information density as shown in Figure 3.9. All images are placed with increasing bitrate from 0.1bpp to 8bpp

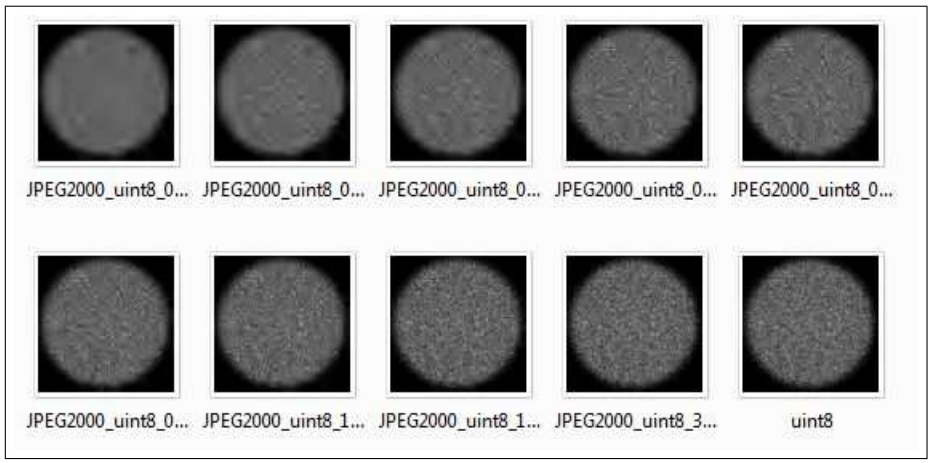

Figure 3.8 Compressed images with low detected counts by means of JPEG2000

All in all these lossy JPEG and JPEG2000 compressed images are compared with the original images in terms of their count size on the pixels by means of MSE, PSNR, and SNR.

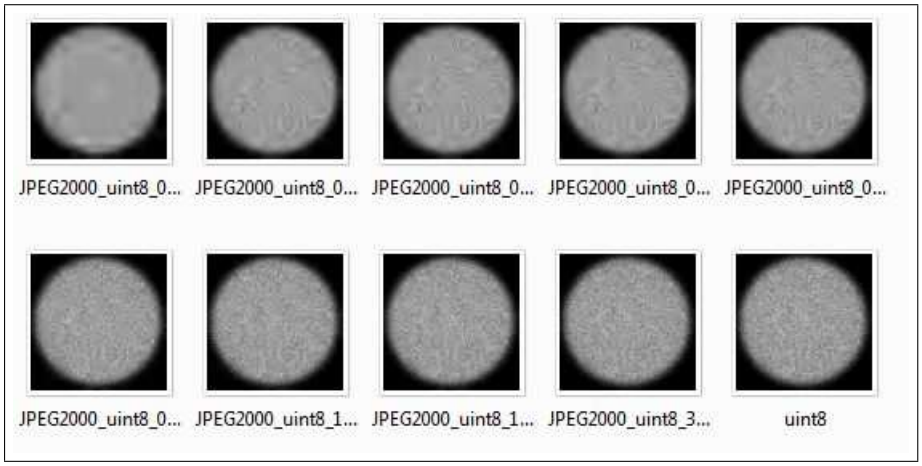

Figure 3.9 Compressed images with high detected counts by means of JPEG2000

3.3 The Second Set of Experiments

The second part of the experiment depends on three different cases (best case, typical case, and worst case) since this study is especially related with the effect of compression on subtle lesion. If the compression process is applied to the images which have subtle lesions the diagnostic task is the most straightforward therefore the study included the different lesion detectability rate on subtle lesion.

3.3.1 Best case study

For the easiest situations of lesion detectability the breast was modeled as smallest size and lesion was modeled as biggest size. The breast is modeled a cylinder filled with ^{99m}Tc and water. It has the dimensions of 5cm height and 8cm diameter. The volume of the breast is 251.2cc. The lesion is assumed to be composed of water and ^{99m}Tc and have a diameter of 0.7cm. The volume of the lesion is 0.179503cc. The collimator parameters are the same as the first part of the experiment. The simulation parameters of breast are shown in Table 3.3 and for lesion are shown in Table 3.4.

Table 3.3
Simulation parameters of breast

Photon energy	140 keV (^{99m}Tc)
Energy resolution	10.6% at 140 keV
Intrinsic resolution	0.380cm
Crystal length	40cm
Crystal width	50cm
Crystal thickness	0.935cm
Source dimensions	8x8x5cm (Cylinder) [best case] 10x10x6cm (Cylinder) [typical case] 12x12x7cm (Cylinder) [worst case]
Phantom dimensions	8x8x5cm (Cylinder) [best case] 10x10x6cm (Cylinder) [typical case] 12x12x7cm (Cylinder) [worst case]
Source activity	929.44 MBq [best case] 1742.7 MBq [typical case] 2927.7 MBq [worst case]
Source to camera distance	4 cm (from the center of the phantom)
Energy window	10% (126 keV-154 keV)
Pixel size	0.1cm
Image matrix size	128x128
Collimator Hole Shape	Hexagonal
Simulated photons	1000000

Table 3.4
Simulation parameters of lesion

Photon energy	140 keV (^{99m}Tc)
Energy resolution	10.6% at 140 keV
Intrinsic resolution	0.380cm
Crystal length	40cm
Crystal width	50cm
Crystal thickness	0.935cm
Source dimensions	0.7x0.7x0.7cm (Sphere) [best case] 0.6x0.6x0.6cm (Sphere) [typical case] 0.5x0.5x0.5cm (Sphere) [worst case]
Phantom dimensions	8x8x5cm (Cylinder) [best case] 10x10x6cm (Cylinder) [typical case] 12x12x7cm (Cylinder) [worst case]
Source activity	3.745 MBq [best case] 2.358 MBq [typical case] 1.365 MBq [worst case]
Source to camera distance	4 cm (from the center of the phantom)
Energy window	10% (126 keV-154 keV)
Pixel size	0.1cm
Image matrix size	128x128
Collimator Hole Shape	Hexagonal
Simulated photons	1000000

The SIMIND simulation program has simulation flags settings in its **change** execution command. Flag 8 is responsible for simulating randomly different simulation images so I produced randomly 100 different lesion present images and lesion absent images with high information density and low information density. As in the first part of this study better lesion detection is obtained with higher total detected counts image. High information density of lesion present and absent images is approximately 50 counts per pixel and low information density is approximately is 10 counts per pixel. The Lesion present (left side) and the lesion absent (right side) images with higher information density (bottom) and lower information density (top) can be seen in Figure 3.10.

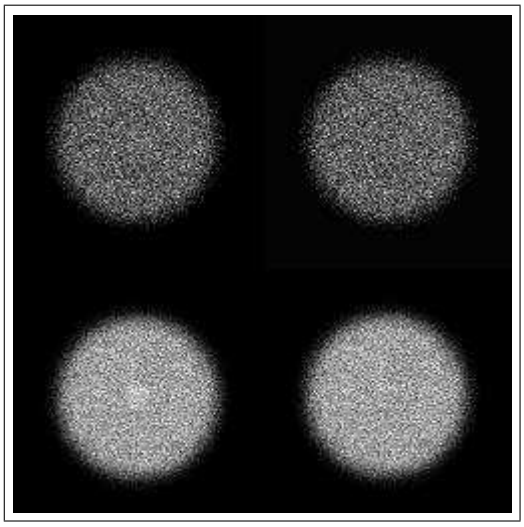

Figure 3.10 Simulated best case images with high detected counts (bottom) and low detected counts (top).

After the generation of original lesion present and absent images they are compressed with JPEG2000 codec and irreversibly compressed 100 lesion present and 100 lesion absent images are generated. The compression procedure is the same as the one in the first part of the experiment.

3.3.2 Typical case study

For the moderate situations of lesion detectability the breast has the dimensions of 6cm height and 10cm diameter. The volume of the breast is 471cc. The lesion is

assumed to be composed of water and ^{99m}Tc and have a diameter of 0.6cm. The volume of the lesion is 0.11304cc. The collimator parameters are the same as the first part of the experiment. The simulation parameters of breast are shown in Table 3.3 and for lesion are shown in Table 3.4.

100 different lesion present images and 100 lesion absent images with high information density and low information density are produced. High information density of lesion present and absent images is approximately 50 counts per pixel and low information density is approximately is 10 counts per pixel. The Lesion present (left side) and the lesion absent (right side) images with higher information density (bottom) and lower information density (top) can be seen in Figure 3.11.

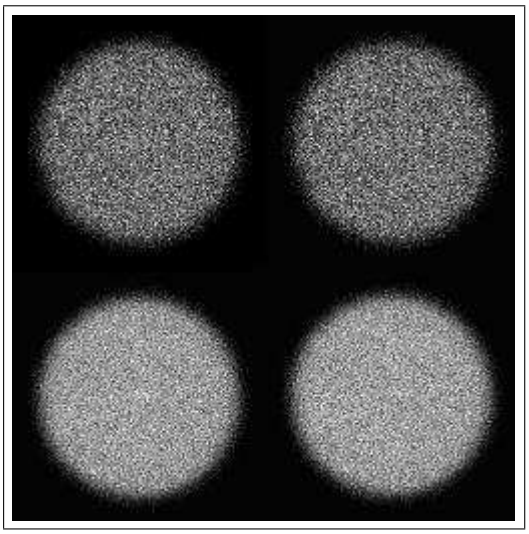

Figure 3.11 Simulated typical case images with high detected counts (bottom) and low detected counts (top).

After the generation of original lesion present and absent images they are compressed with JPEG2000 codec and lossy compressed 100 lesion present and 100 lesion absent images are generated. The compression procedure is the same as the one in the first part of the experiment.

3.3.3 Worst case study

For the hardest situations of lesion detectability the breast was modeled as biggest size and lesion was modeled as smallest size. The breast is modeled a cylinder filled with ^{99m}Tc and water. It has the dimensions of 7cm height and 12cm diameter. The volume of the breast is 791.28cc. The lesion is assumed to be composed of water and ^{99m}Tc and have a diameter of 0.5cm. The volume of the lesion is 0.065417cc. The collimator parameters are the same as the first part of the experiment. The simulation parameters of breast are shown in Table 3.3 and for lesion are shown in Table 3.4.

100 different lesion present images and 100 lesion absent images with high information density and low information density are produced. As in the first part of this study better lesion detection is obtained with higher total detected counts image. High information density of lesion present and absent images is approximately 51 counts per pixel and low information density is approximately is 10 counts per pixel. The Lesion present (left side) and the lesion absent (right side) images with higher information density (bottom) and lower information density (top) can be seen in Figure 3.12.

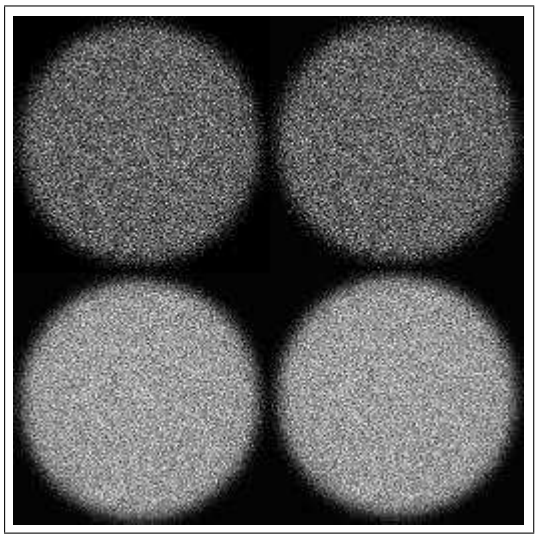

Figure 3.12 Simulated worst case images with high detected counts (bottom) and low detected counts (top).

After the generation of original lesion present and absent images they are compressed with JPEG2000 codec and lossy compressed 100 lesion present and 100 lesion

absent images are generated. The compression procedure is the same as the one in the first part of the experiment.

3.3.4 JPEG 2000 Compression

To sum up the output of each simulation is one for lesion present image and the other is lesion absent image. The lesion present images are created by superimposing the two separate *.bim files. 100 different simulated lesion absent and lesion present images are created with adding poisson noise on 8-bit gray level in tiff format for each best case, typical case, and worst case conditions. In addition to that all generated images are grouped in terms of detected counts on images.

After that the compression standard JPEG 2000 are employed to these lesion present and lesion absent images by means of Vc compression software for each best case, typical case, and worst case conditions. The reconstructed images are saved in terms of different compressed bit rate or compression ratio for higher and lower number of detected counts. Figure 3.13 shows that the one data of the compressed lesion present and lesion absent images with high detected counts and low detected counts from 200 pairs of simulated images. The first two rows are high information density images and the last two rows are low information density images. In each group the first row indicates compressed lesion present images and the last row indicates lesion absent images.

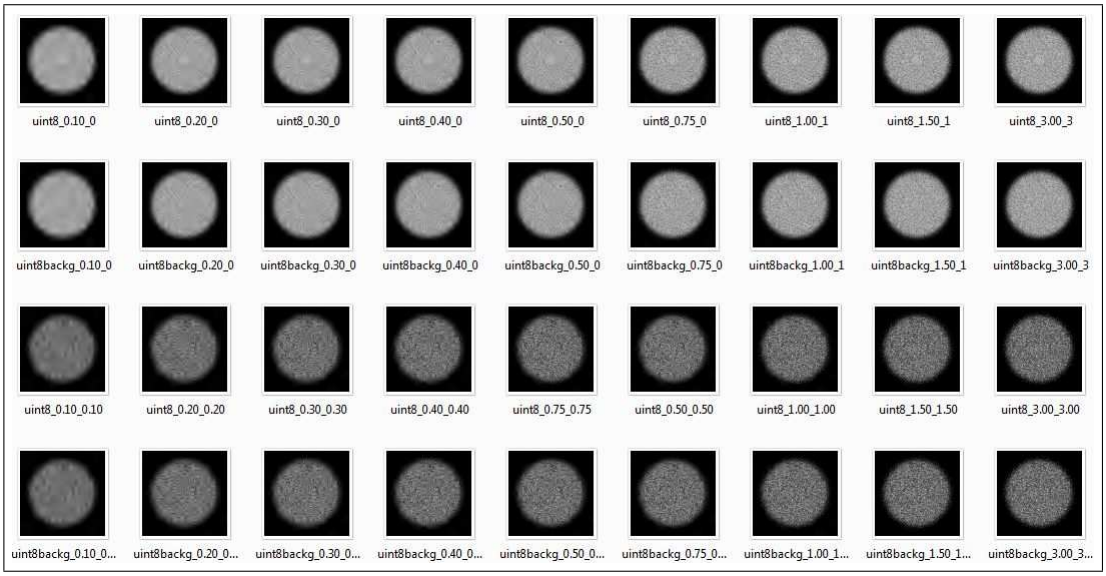

Figure 3.13 compressed one set of typical image pairs by using JPEG 2000

3.3.5 Laguerre-Gauss channelized Hotelling Observer

The final step in my study is the calculation of lesion detection against to the degradation of image quality by compression ratio. The AUC is a figure of merit is used by this reason so channelized hotelling observer model is applied with Laguerre-Gauss functions. The Laguerre-Gauss functions used to synthesize the channelized hotelling template w_c were Laguerre polynomials multiplied by a gaussian envelope. The nth order Laguerre-Gauss functions are defined as:

$$LG_n(r) \;=\; 2\sqrt{\frac{\pi}{a^2}}\exp(\frac{-\pi r^2}{a^2})\;L_n(\frac{2\pi r^2}{a^2}) \tag{3.1}$$

where a is width parameter. Specifically, the values of a used for the spheres of diameter 7, 6, and 5 mm were 26, 21.5, and 15 mm, respectively. L_n is nth-order Laguerre polynomial, defined as:

$$L_n(x) \;=\; \sum_{m=0}^{n}(-1)^m \begin{pmatrix} n \\ m \end{pmatrix} \frac{x^m}{m!} \tag{3.2}$$

From left to right of Figure 3.14 shows first five 128x128 Laguerre-Gauss templates that are used in the simulation. The channel matrix U is constructed by putting the 5

templates into column vectors and combining, yielding a 16384x5 matrix for U.

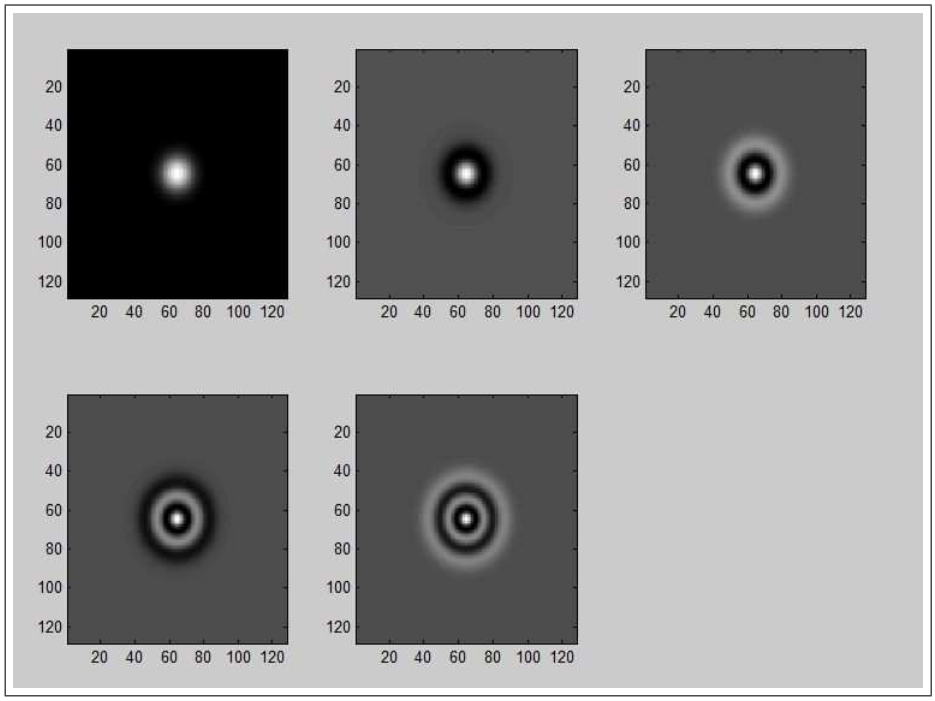

Figure 3.14 Laguerre-Gauss Channel Profile

4. RESULTS AND DISCUSSIONS

In the first part of the study simulated breast scintigraphy image was compressed for various values of the compression bit rate ranging from 8bpp to 0.1bpp. By using the Equations 2.7, 2.8, 2.9 from the previous section, the evaluation of the reconstructed image was calculated. The results included two different concepts. The first one is to compare JPEG and JPEG 2000 between the original and reconstructed images having the same information density. The second one is to compare the effect of total detected count size on images within the same compression standard.

The second part of the experiment depends on three different cases (best case, typical case, and worst case) which are created with different image pixel density since this study is especially related with the effect of compression on lesion sizes and image information density. If the compression process is applied to the images which have subtle lesions the diagnostic task is the most straightforward therefore the study included the different lesion detectability rate on subtle lesion. The another straightforward concept this part of study includes is the observation of diagnostic loss due to compression is comparable with other sources of imaging chain (same order or magnitude with variation in equipment / data acquisition protocols).

4.1 Image Quality Using Classical Metrics

MSE, SNR, and PSNR calculated the difference between the reconstructed images and original images. Firstly these metrics is calculated for different compression standards within the images having higher detected counts.

4.1.1 The Results of compressions on higher count rate

In this study it was found that for JPEG compression, the PSNR was between 17.3dB to 53.5dB, where as for JPEG2000 it was between 21.6dB to 38.2dB. The actual value of PSNR is not meaningful, but the comparison between the two values of different reconstructed images gives a measure of quality. Table 4.1 shows the range of objective quality measures between the reconstructed images and original images. Measures marked with asterisk (*) grow up as the value of bit rate decreases. Table 4.2 represents the results for MSE, SNR, and PSNR for breast scintigraphy image. These results illustrate that, as compression ratio increases the MSE increases whereas the PSNR and the SNR decreases. These results were also plotted in Figure 4.1 and Figure 4.2 to show the changes for MSE, SNR, and the PSNR as compression ratio changes for JPEG compression and JPEG2000 compression.

Table 4.1
Results of image quality metrics for high information density image

Symbol	**Measure description**	**Range of values** JPEG / JPEG2000
MSE	Mean Square Error (Eq.2.7)	[0.3 : 1199.5]* / [9.8 : 453.2]*
PSNR	Peak Signal to Noise Ratio (Eq.2.9)	[53.5 : 17.3] / [38.2 : 21.6]
SNR	Signal to Noise Ratio (Eq.2.8)	[42 : 5.8] / [26.9 : 10.3]

From all tables and figures we can conclude that decrease in the quality means increase in the compression ratio. A small decrease in the number of bits results a big decay in MSE is exponential. Compression with JPEG2000 gives satisfactory results than JPEG at the same compression rates. For example compressing the images to 0.2bpp JPEG MSE takes the value 768.3 but on the other hand JPEG2000 MSE takes the value 406.5. In addition to that there is the same differences between the SNR and PSNR values. The JPEG PSNR takes the value 19.3 however the JPEG2000 PSNR takes the value 22. All in all lower value of MSE indicated the high similarity which is required situation and higher PSNR is equivalent to lower distortion in the image.

Table 4.2
Objective measures vs bit rates for JPEG and JPEG2000 compression on high information density image

Bit Rate	Compression Ratio	MSE JPEG/JPEG2000	PSNR JPEG/JPEG2000	SNR JPEG/JPEG2000
3bpp	2.66:1	31.9 / 9.8	33.1 / 38.2	21.6 / 26.9
1.6bpp	5:1	183.2 / 100.3	25.5 / 28.1	14 / 16.8
1bpp	8:1	273.1 / 172.3	23.8 / 25.8	12.3 / 14.5
0.8bpp	10:1	308.4 / 236.5	23.2 / 24.4	11.7 /13.1
0.5bpp	16:1	373.3 / 305.4	22.4 /23.3	10.9 / 12
0.4bpp	20:1	404.7 / 346.3	22.1 / 22.7	10.6 / 11.4
0.3bpp	26.6:1	768.3 / 368.3	19.3 / 22.5	7.8 / 11.2
0.2bpp	40:1	768.3 / 406.5	19.3 / 22	7.8 / 10.8
0.1bpp	80:1	1199.5 / 453.2	17.3 / 21.6	5.8 / 10.3

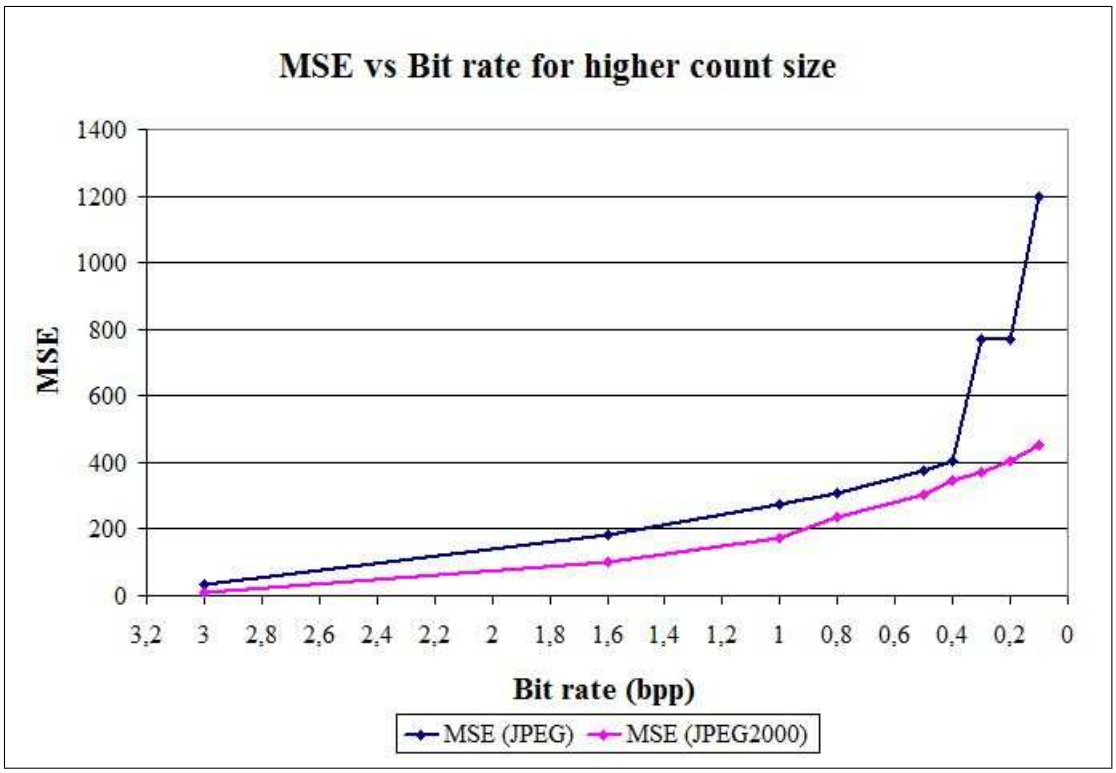

Figure 4.1 MSE values against bit rates for JPEG and JPEG2000 on image with higher count size

The shown figures and tables support our thoughts that JPEG2000 is a more efficient way to compress images for the same compression ratios.

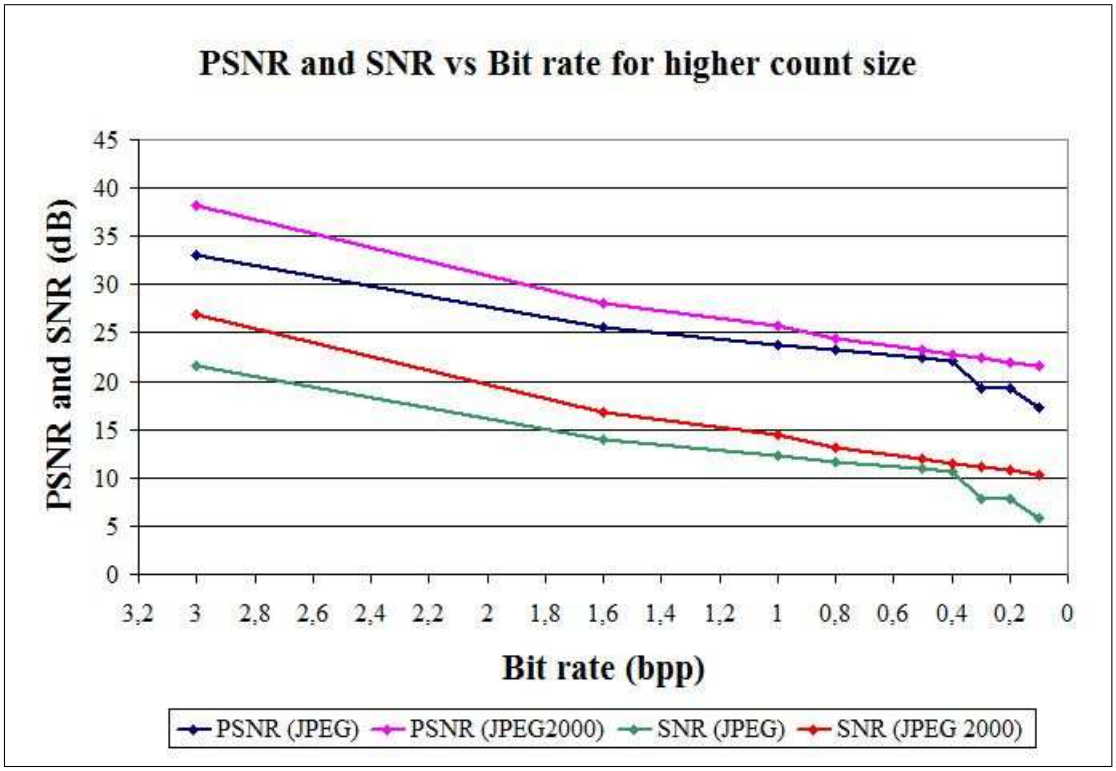

Figure 4.2 PSNR and SNR values against bit rate for JPEG and JPEG2000 on image with higher count size

4.1.2 The Results of compressions on lower count rate

Table 4.3
Results of image quality metrics for low information density image

Symbol	**Measure description**	**Range of values** JPEG / JPEG2000
MSE	Mean Square Error (Eq.2.7)	[0.7 : 1581.5]* / [13.1 : 673.3]*
PSNR	Peak Signal to Noise Ratio (Eq.2.9)	[49.9 : 16.1] / [37 : 19.8]
SNR	Signal to Noise Ratio (Eq.2.8)	[35.5 : 1.8] / [22.6 : 5.5]

The MSE should be equal to 0 and PSNR should be infinity for identical images. For example lossless compression reduces the size of the image around a factor of 2 however it generates an identical images. As the encoding rate increases the MSE values also increase accordingly implying that the distortion in the image increases as the compressed image get smaller in size.

Table 4.4
Objective measures vs bit rates for JPEG and JPEG2000 compression on low information density image

Bit Rate	**Compression Ratio**	**MSE** JPEG/JPEG2000	**PSNR** JPEG/JPEG2000	**SNR** JPEG/JPEG2000
3bpp	2.66:1	48 / 13.1	31.3 / 37	17 / 22.6
1.6bpp	5:1	305 / 145.7	23.3 / 26.5	9 / 12.2
1bpp	8:1	456.7 / 265.5	21.5 / 23.9	7.2 / 9.6
0.8bpp	10:1	502.5 / 372	21.1 / 22.4	6.8 / 8.1
0.5bpp	16:1	601 / 473.4	20.3 /21.4	6 / 7.1
0.4bpp	20:1	657.1 / 517	20 / 21	5.6 / 6.7
0.3bpp	26.6:1	974.5 / 571	18.2 / 20.6	3.9 / 6.2
0.2bpp	40:1	974.5 / 625.6	18.2 / 20.2	3.9 / 5.9
0.1bpp	80:1	1581.5 / 673.3	16.1 / 19.8	1.8 / 5.5

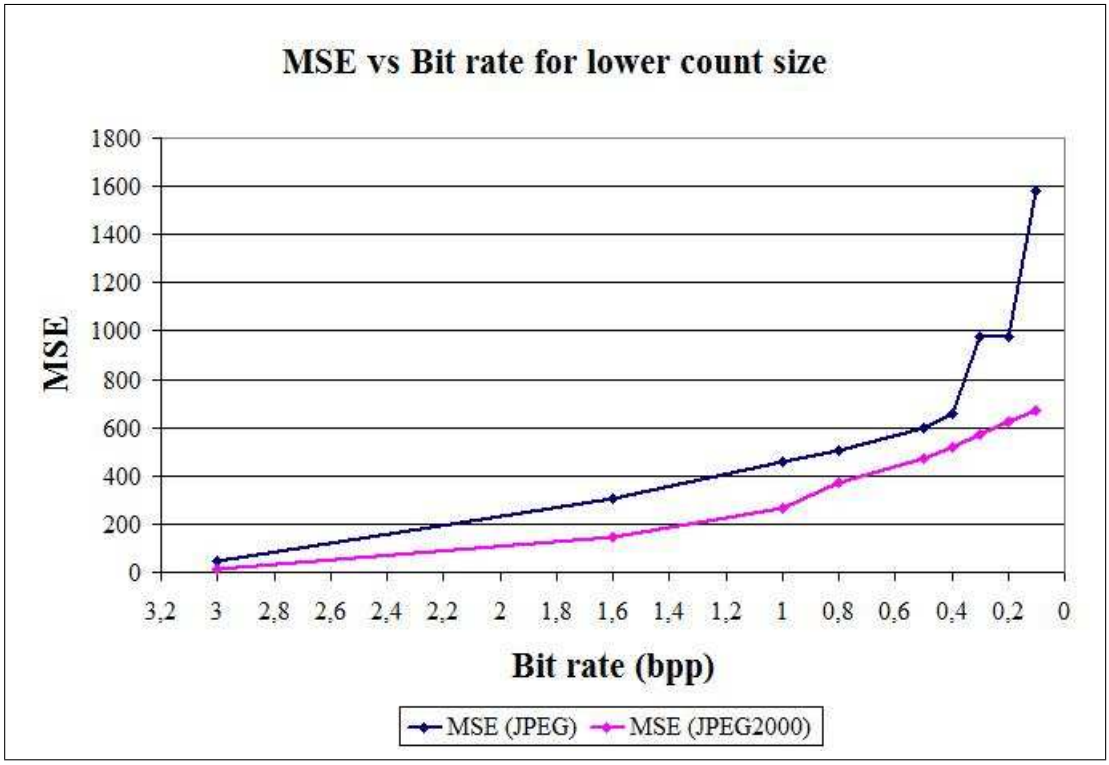

Figure 4.3 MSE values against bit rates for JPEG and JPEG2000 on image with lower count size

The results showed that JPEG2000 is more efficient than JPEG especially in higher compressed bit rate. The MSE value of low information density image is higher

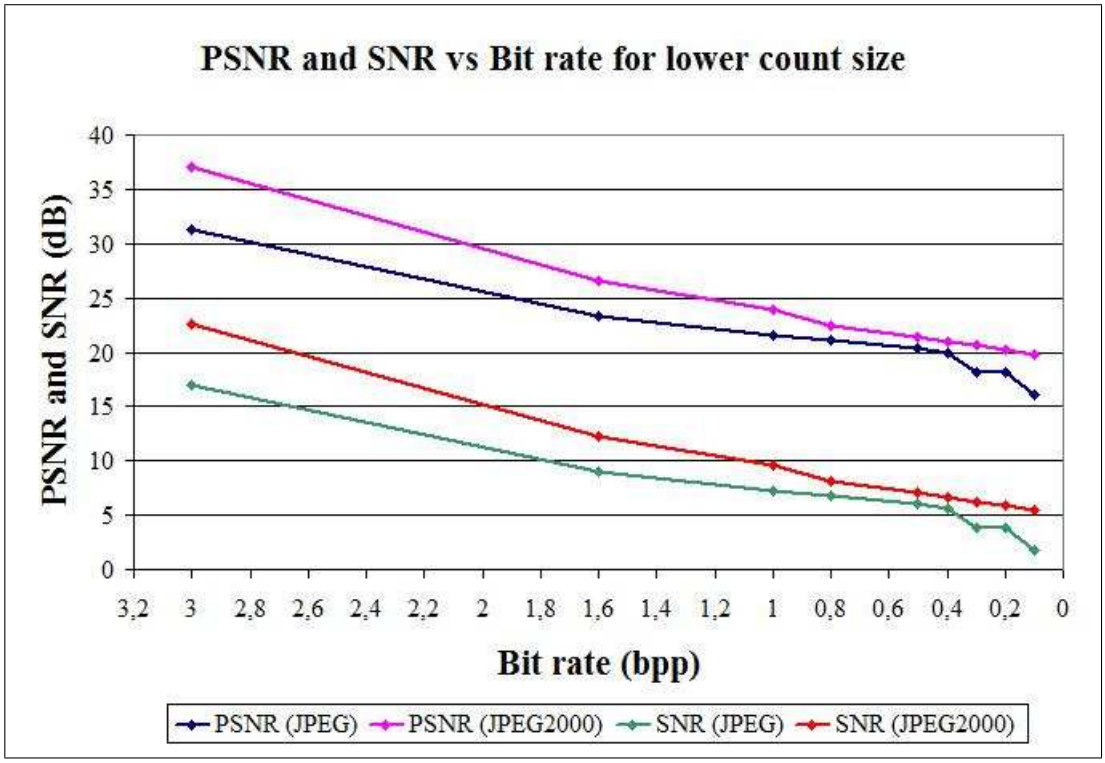

Figure 4.4 PSNR and SNR values against bit rate for JPEG and JPEG2000 on image with lower count size

than the one in high information density image. For instance compressing the images to 0.2bpp JPEG MSE takes the value 974.5 but on the other hand JPEG2000 MSE takes the value 625.6. In addition to that there is the same differences between the SNR and PSNR values. The JPEG PSNR takes the value 18.2 however the JPEG2000 PSNR takes the value 20.2. The differences of the metric values between the JPEG and JPEG2000 compression are approximately same as the high information density images. However the degradation of image quality is higher in low information density image.

4.1.3 The Effects of detected counts on JPEG compressed images

It is clear that increasing number of detected counts improves the performance of the breast scintigraphy and hence image quality. If image quality of one image is higher than the other one, the degradation of quality becomes smaller due to compression noise. The quality of an image depends on the number of photons it contains. If

we use too few photons, the image will be noisy and it will make it difficult or even impossible for the radiologist to give a correct diagnosis. It may also take longer time for the radiologist to give a diagnosis using a noisy image. A minimum value for the noise in the image can be the Poisson error $\sqrt{N}$ on the measured counts N. If the photon count is low so the noise is higher in the image. In this part of the study low information density image has more noise than the high information density image. In Figure 4.5 and 4.6 we can conclude that MSE at low count density image is higher than the MSE at high count density image. However PSNR and SNR at low count density image is smaller than the one at high count density image. These results stems from the image quality of the original image since signal to noise ratio is higher at high information density image because of decreasing noise.

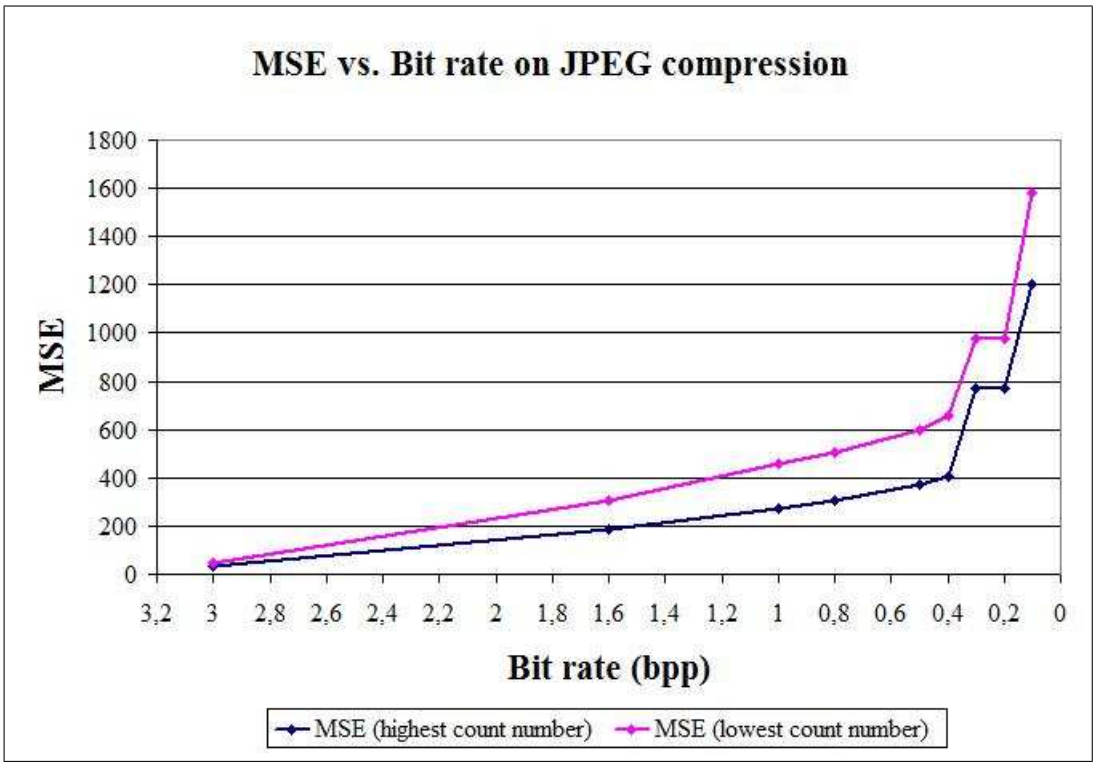

Figure 4.5 MSE values against bit rate for low and high detected count images on JPEG compression

An interesting fact was observed that comparable values of MSE, from a compressed bitrate 3bpp to 0.4bpp its value ranges from 48 to 657.1 in lower count size with JPEG compressed image, which shows a range of 609.1. Similarly MSE value ranges from 31.9 to 404.7 in higher count size with JPEG compressed image, which

shows a range of 372.8. This means that MSE increases most in lower count size image for JPEG compression.

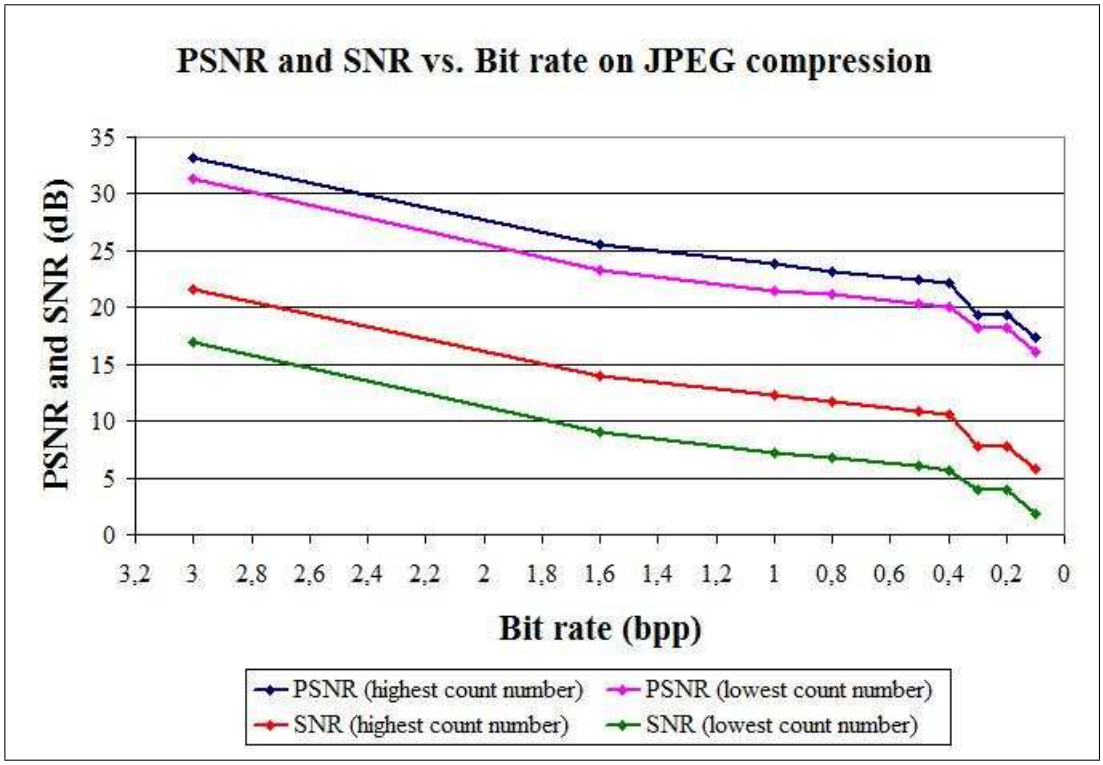

Figure 4.6 PSNR and SNR values against bit rate for low and high detected count images on JPEG compression

Another interesting fact was observed that PSNR values were decreased with decreasing bitrates. For comparable values of PSNR, from a compressed bitrate 3bpp to 0.4bpp its value ranges from 31.3dB to 20dB in lower count size with JPEG compressed image, which shows a range of 11.3dB. Similarly for JPEG compressed high count size image its value ranges from 33.1dB to 22.1dB, which shows a range of 11dB. This results showed that PSNR value decreases most in lower count size image.

4.1.4 The Effects of detected counts on JPEG 2000 compressed images

Similarly, the effects of count size in JPEG 2000 compressed images are shown in terms of MSE and PSNR respectively in Figures 4.7 and 4.8 . The results showed that in Figure 4.7 comparable values of MSE, from a compressed bitrate 3bpp to 0.4bpp its

value ranges from 13.1 to 517 in lower count size with JPEG 2000 compressed image, which shows a range of 503.9. However its value ranges from 9.8 to 346.3 in higher count size with JPEG 2000 compressed image, which shows a range of 336.5. This means that MSE increases most in lower count size image for JPEG 2000 compression as in JPEG compression.

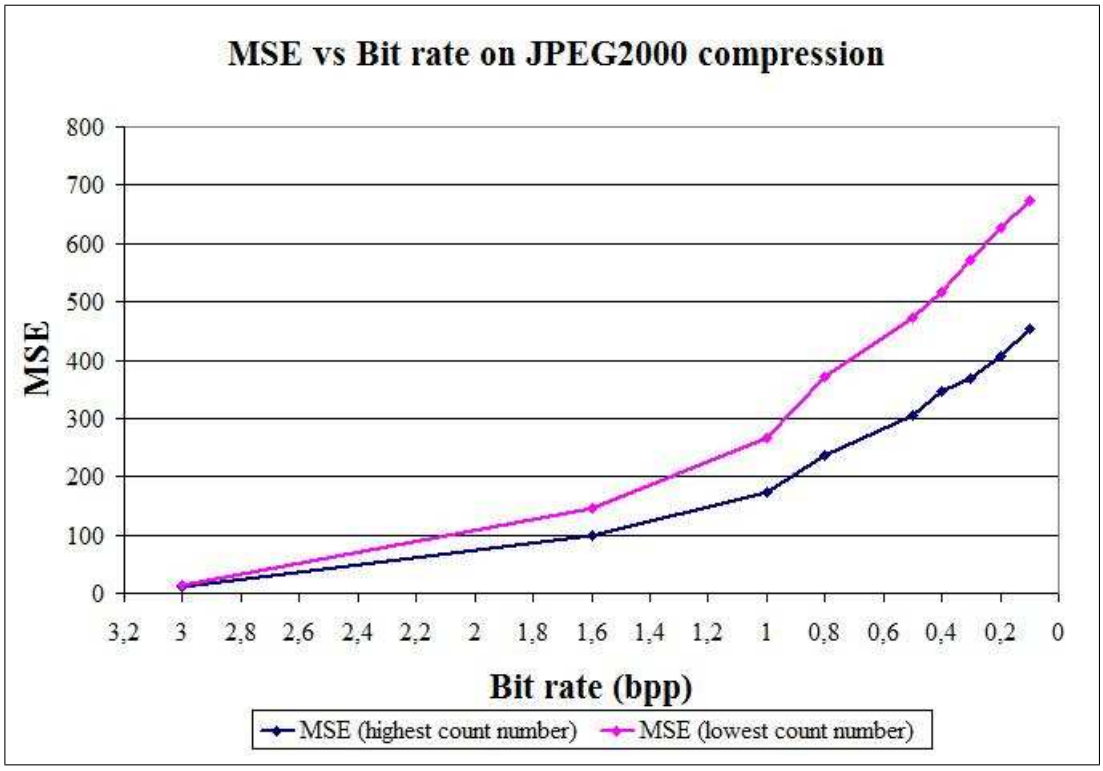

Figure 4.7 MSE values against bit rate for low and high detected count images on JPEG 2000 compression

The other result was observed that for comparable values of PSNR, from a compressed bitrate 3bpp to 0.4bpp its value ranges from 37dB to 21dB in lower count size with JPEG 2000 compressed image, which shows a range of 16dB. Similarly for JPEG 2000 compressed high count size image its value ranges from 38.2dB to 22.7dB, which shows a range of 15.5dB. This means that PSNR value decreases most in lower count size image as in JPEG compression.

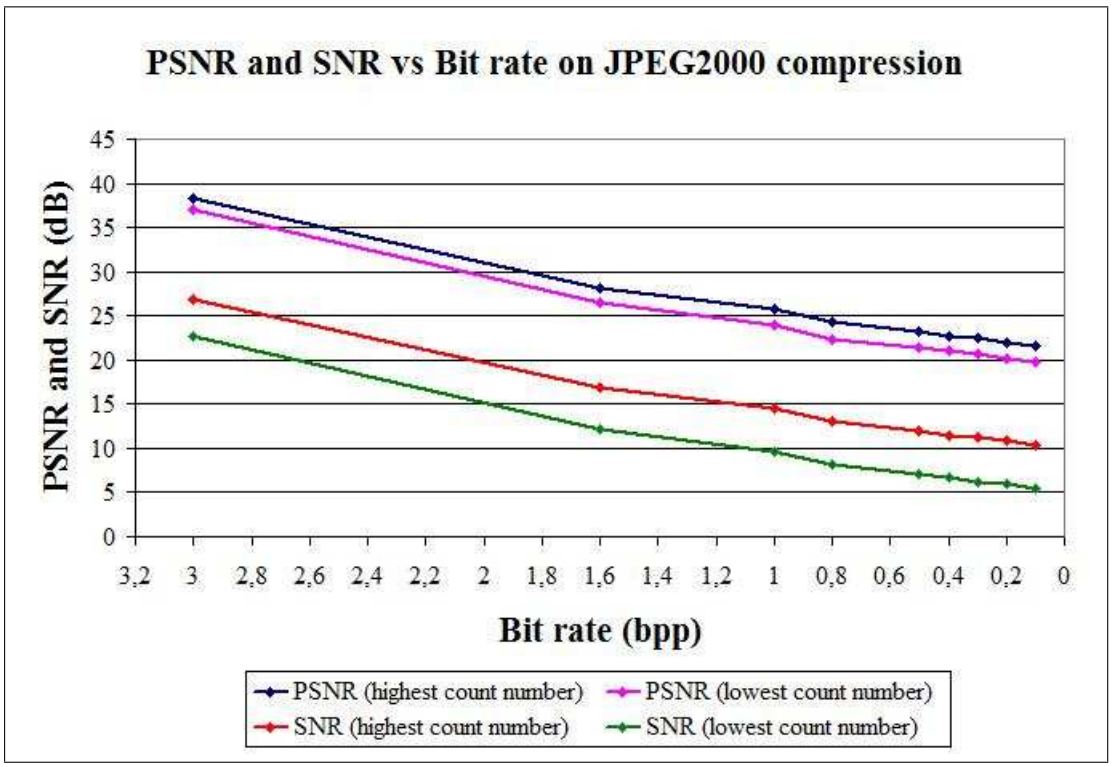

Figure 4.8 PSNR and SNR values against bit rate for low and high detected count images on JPEG 2000 compression

4.2 Analysis of The Compression Ratio and Lesion Detectability of Model Observer

Previous experiment has shown that JPEG2000 compression algorithm is better than JPEG algorithm for compressing simulated scintigraphic images. In the second part of the experiment mathematical observer model was used to show the effect of image compression on lesion detection. Furthermore, the compression ratio and diagnostic loss were analyzed by model observer. In this case, the task is to observe the noisy compressed images and decide whether or not a lesion (tumor) is present.

Our task is a simple binary decision task. In breast scintigraphy the most interesting task is to detect the abnormality (the evidence of a tumor in the breast). The determination of whether a lesion or tumor is present in an image is a signal detection task. The observer is the entity that will make use of the images to perform the task. In the binary decision task, the observer determines which of two states the image belongs to. In this study the observer was a computer program.

The detection task involves detecting a signal in a background. We consider signal known exactly/background known exactly (SKE/BKE) class of signals and backgrounds. In SKE tasks, the signal is assumed to be a known deterministic entity, i.e. all parameters characterizing the signal location, size, shape, amplitude, etc. are assumed to be known to the observer. The signal function is completely specified and the only uncertainty is whether or not it is present. The SKE detection tasks are convenient to analyze because their simplicity sometimes allows for analytical computation of figures of merit. In BKE tasks, one may assume the underlying object (the attenuation coefficients) or background is known to the observer and fixed. There is thus no object variability or object randomness. In SKE/BKE task, an error in detection could be due to the effects of radiation Poisson noise, compression noise or other image artifacts. Such simplified tasks are not clinically realistic, however it is sufficient to compare the diagnostic loss for subtle lesion and visible lesion at all compression ratios.

Table 4.5
Values of the observer model for highest detected counts

Bit Rate	Best Case	Typical Case	Worst Case
8bpp	1	0.9998	0.9288
3bpp	1	0.9998	0.9272
1.5bpp	1	0.9998	0.9116
1bpp	1	0.9998	0.9095
0.75bpp	1	0.9994	0.8825
0.5bpp	1	0.9987	0.8715
0.4bpp	1	0.9986	0.8752
0.3bpp	1	0.9986	0.8636
0.2bpp	1	0.9985	0.8624
0.1bpp	1	0.9702	0.7533

Table 4.6
Values of the observer model for lowest detected counts

Bit Rate	Best Case	Typical Case	Worst Case
8bpp	0.9920	0.9551	0.6888
3bpp	0.9921	0.9549	0.6910
1.5bpp	0.9927	0.9458	0.6873
1bpp	0.9892	0.93	0.6667
0.75bpp	0.9885	0.9285	0.6672
0.5bpp	0.9878	0.9229	0.6713
0.4bpp	0.9884	0.9160	0.6277
0.3bpp	0.9881	0.9081	0.6037
0.2bpp	0.9839	0.9032	0.5727
0.1bpp	0.9819	0.8804	0.5721

Table 4.5 and 4.6 show the values of AUCs calculated with Laguerre-Gauss Channelized Hotelling observer in values bit rates from 8bpp to 0.1bpp. AUC shows the detection capability of the model observer and it is in the range [0.5, 1], where higher values of the AUC indicate better model observer performance for the lesion detection task. If the AUC = 1, then the model observer always detects the lesion,

regardless of the decision threshold. On the other hand, if the AUC = 0.5, then for any threshold, TPF=FPF, and the model observer performs no better than arbitrary guessing.

According to the high information density images the detection capability of the observer model experiences no changes for all bit rate values on visible lesion (best case). In addition to that for moderate situation of lesion size (typical case) a slight loss such as 2.96% can be seen from 8bpp (original image) to 0.1bpp. However for hardest situation of lesion detectability (worst case) percentage change is increased to 18.9%. Figure 4.9 showed that as bit rates values decrease below 0.2bpp level of compression, the capability of the observer to correctly classify a lesion begins to fall more rapidly to 0.7533 (i.e. only 3 of 4 lesions are being correctly classified). However compression did not affect the detectability for other cases.

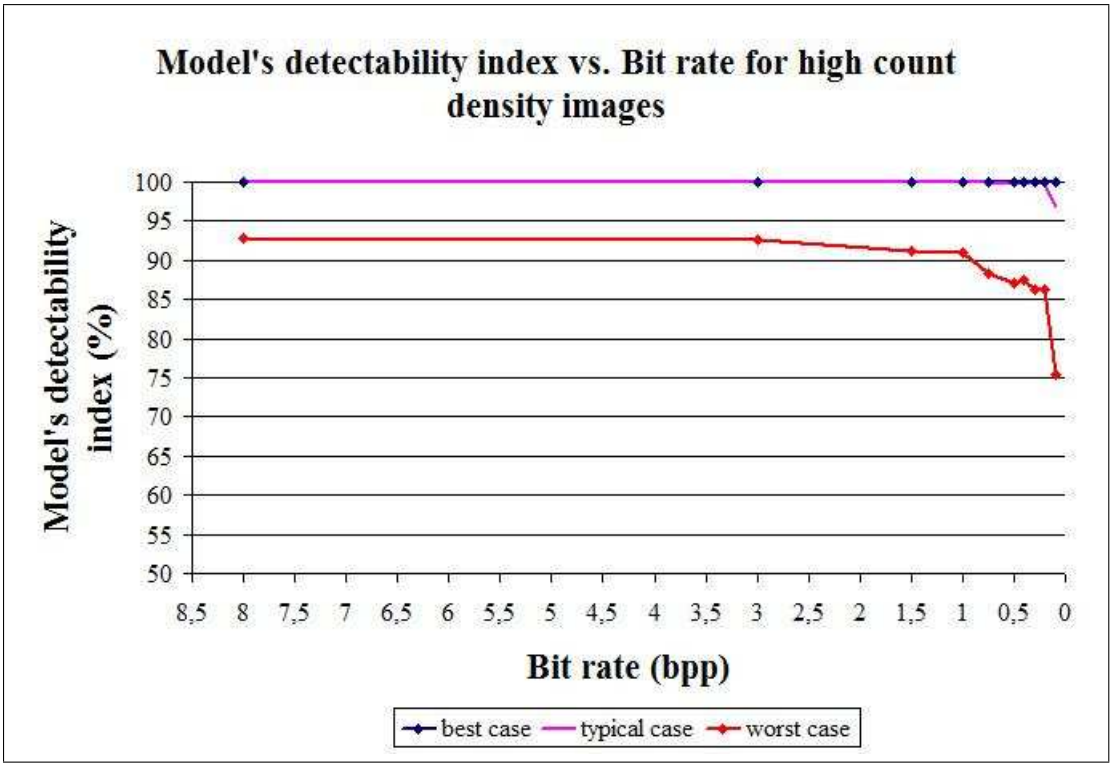

Figure 4.9 The observer model behaviour in the interval of bit rates from 8bpp to 0.1bpp for highest count size

The other interesting result was observed with decreasing the total detected counts on the images. The settings on total detected counts on images can be made by

changing the amount of radiation dose or the acquisition time. These all are the cost-effective process and they also affect the diagnostic decision by compression. According to the low information density images the detection capability of the observer model experiences less variances (such as 1.02%) for all bit rate values on visible lesion (best case). In addition to that for moderate situation of lesion size (typical case) a slight loss (such as 7.82%) can be seen from 8bpp (original image) to 0.1bpp. However for hardest situation of lesion detectability (worst case) percentage change is increased to 17%. These values are comparable for the values of high count density images. For best case and typical case condition the diagnostic loss after compression on low count density images are bigger than the ones on high count density images. Furthermore, for the worst case condition this difference is nearly same but the lesion detectability is extremely small due to lower detected counts. Figure 4.10 summarizes these results and the lower detection capability shown by model observer in worst case condition that falls under 60% (i.e. only 3 of 5 lesions are being correctly classified).

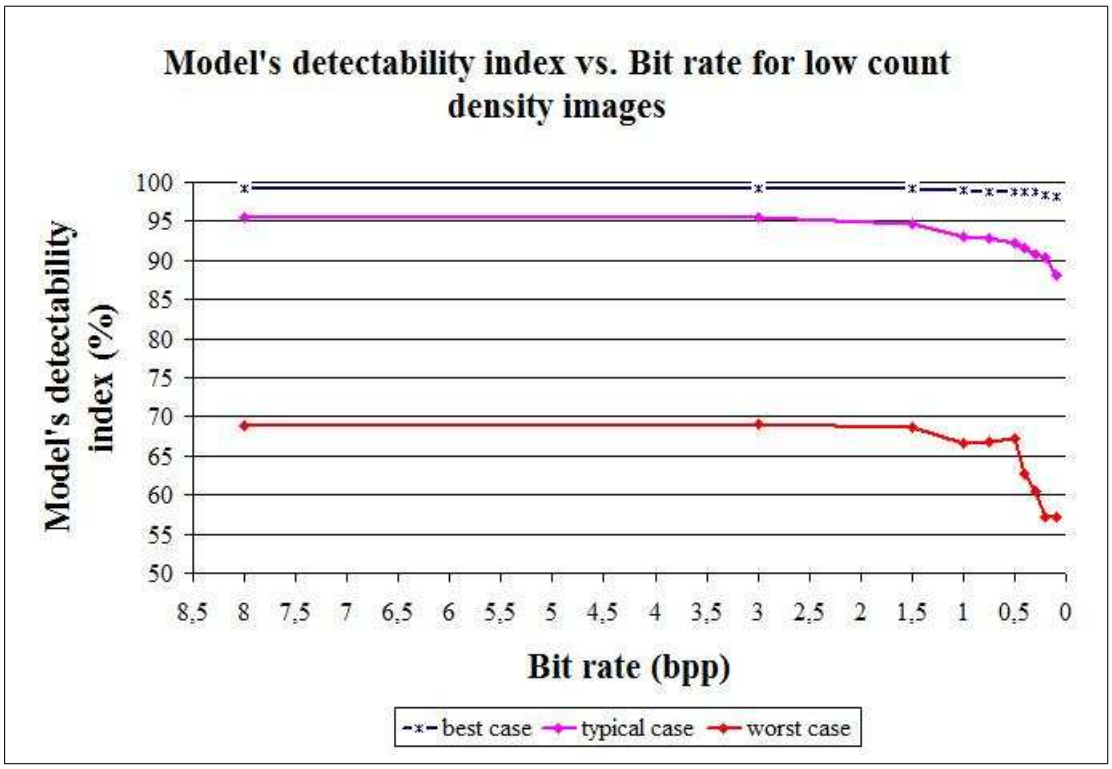

Figure 4.10 The observer model behaviour in the interval of bit rates from 8bpp to 0.1bpp for lowest count size

Another interesting fact observed that for values lower than 0.2bpp (CR=40:1)

the overall image quality begins to be degraded as the bit rate decreases for all typical case conditions and worst case condition on high count density images as shown in Figure 4.12 and 4.13. Below this level the detection capability of the observer model continues to fall as the bit rate decreases so more lesions are going to be misclassified due to quality degradation caused by lossy compression. This fact is not valid for all best case conditions and worst case condition on low count density images since there is no significant degradation on best case images as shown in Figure 4.11 but for bit rate values below 0.5bpp (CR=16:1) higher distortion was observed just for worst case condition on low count density images. All in all in one way it seems to be a 0.2bpp (40:1) is an optimal compression ratio but supremely bit rate value 0.5bpp (16:1) is an ideal one for scintigraphic images.

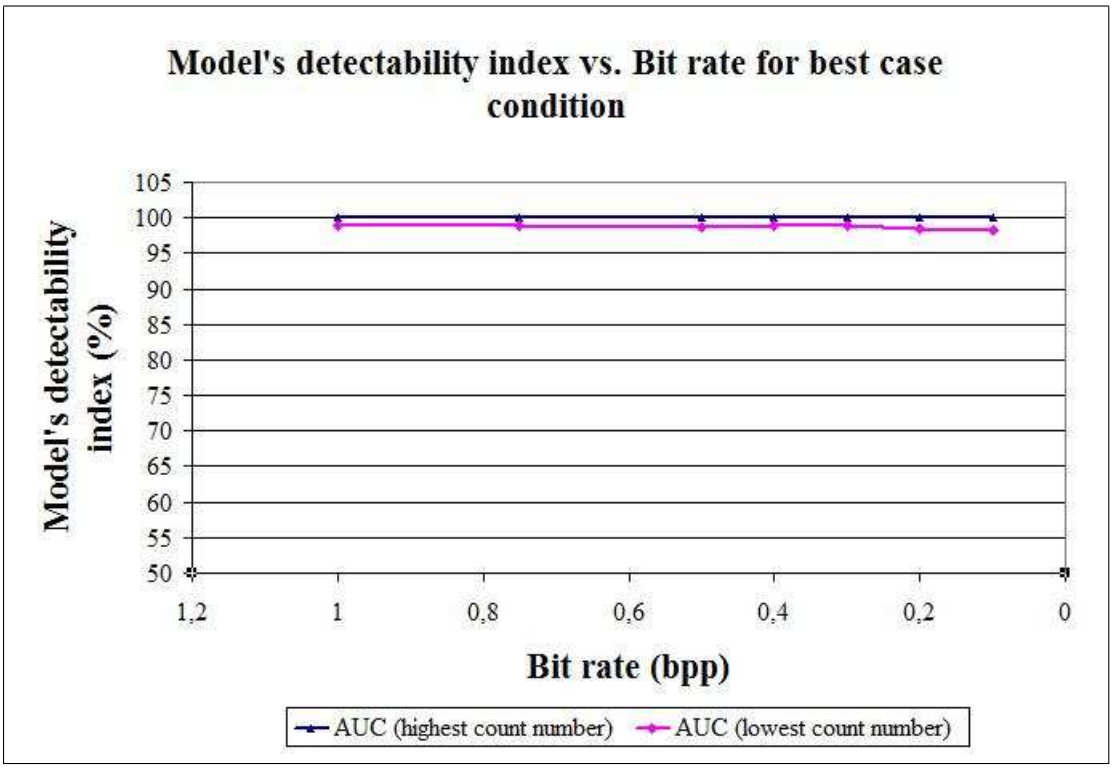

Figure 4.11 The observer model behaviour in the interval of bit rates from 1bpp to 0.1bpp for best case condition

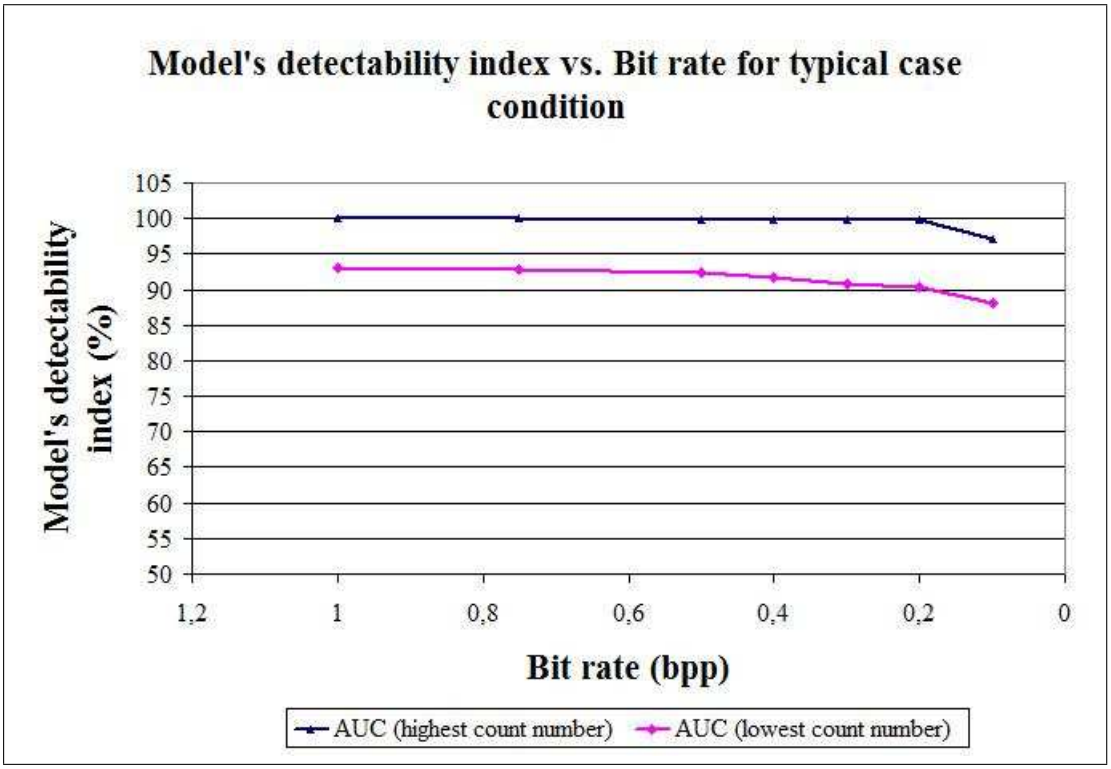

Figure 4.12 The observer model behaviour in the interval of bit rates from 1bpp to 0.1bpp for typical case condition

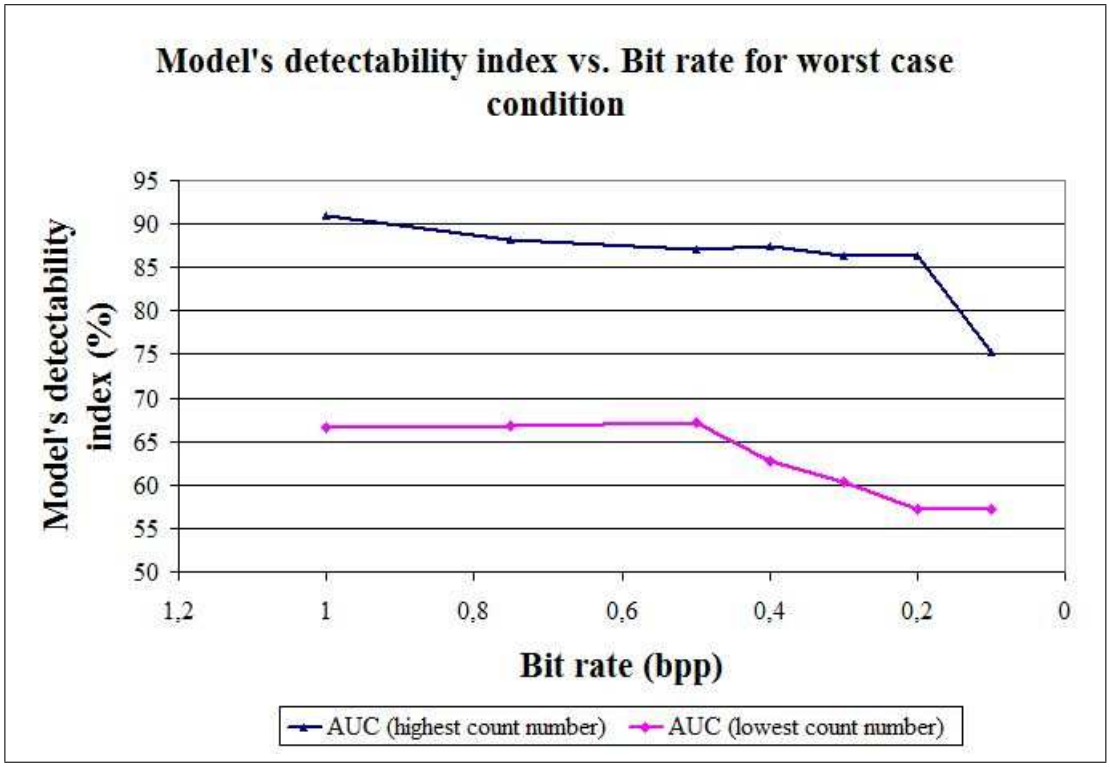

Figure 4.13 The observer model behaviour in the interval of bit rates from 1bpp to 0.1bpp for worst case condition

The one another interesting result was observed that the lesion detectability is minimally increasing after some values of compressed bit rates. These minor changes for some decreased bit rates are removal of noise without degradation of signal structures. The structures important for diagnosis may be more visible and therefore images' diagnostic accuracy is even improved.

The last and straightforward result was observed from Figure **??** that the diagnostic loss due to compression is comparable with the loss due to variations of information density on images. For instance it can be seen that for worst case condition the loss due to compression is approximately 7.22% at 0.2bpp for high count density images however the loss due to variations of count density at the same point is approximately 33.6%. This result is also applicable at other compressed bit rates and different case conditions. Consequently we can say that the loss due to compression is smaller than the loss due to variation of count density on images therefore decreasing time or radiation dose is not better than compression in terms of cost and performance.

5. CONCLUSION

This study uses a computer simulation of the entire imaging chain that includes the organ, the imaging equipment and the human observer so it is perfectly different from the other studies made in this area. we used fully simulation process because the concept of simulation is fundamental. Evaluating diagnostic loss tests require access to data in which the presence or absence of lesions can be independently verified, which is virtually impossible in real clinical studies. Moreover, an extremely large number of images has to be considered in order to establish the results with acceptable statistical significance, and artificial generation of data is more straightforward than the acquisition in a medical setting.

In the first part of this study, we evaluated the ability of image quality metrics to predict the effect of JPEG and JPEG 2000 compression on small lesion size (hardly visible) with simulated scintigraphic images. The results showed that JPEG 2000 compression always outperforms JPEG in terms of image quality at a given compressed bit rates, and the improvement could be dramatic at low compressed bit rate.

In the second part of the study, we observed interesting results. The results showed that the degree of irreversibility acceptable for medical images depends on many important factors and can not be fitted automatically without checking. These factors can be classified as:

1. The modality of imaging (acquisition and digitization of an image, quality of the apparatus)
2. The characteristics of the depicted object (structures to diagnose)
3. The purpose of information (kind of exam, diagnosis technology, diagnosis procedure, way of interpretation)
4. Preferences of the responsible radiologist

The results of observer model on high count density images showed that there is no diagnostic loss at all tried compression rate. Furthermore, for typical and worst case there is a slight loss at all rates up to 0.2bpp. However for low count density images these results a little bit different from high count density images since for best and typical case we observed slight loss at all rates up to 0.2bpp and for worst case this loss observed up to 0.5bpp. As a conclusion we can say that it seems to be a 0.2bpp (40:1) is an optimal compression ratio but supremely bit rate value 0.5bpp (16:1) is an ideal one for scintigraphic images.

Comparing the results of first part of the study and second part of the study showed that model observer showed absolute loss in detectability but other metrics did not. Diagnostic loss due to compression is comparable with other sources of imaging chain (same order or magnitude with variation in equipment / data acquisition protocols). For instance it can be seen that for worst case condition the loss due to compression is approximately 7.22% at 0.2bpp for high count density images however the loss due to variations of count density at the same point is approximately 33.6%. This result is also applicable at other compressed bit rates and different case conditions. Consequently we can say that the loss due to compression is smaller than the loss due to variation of count density on images therefore decreasing time or radiation dose is not better than compression in terms of cost and performance.

The another conclusion was observed that we can use simulation to measure the effect of various compression algorithms on diagnostic loss. Furthermore, diagnostic loss occurs at all compression ratios for subtle lesions however this error is not much different than other variances in the imaging chain. We can therefore see the compression issue a just another engineering tradeoff between cost and performance. For low count density images the diagnostic losses are 1.02%, 7.82%, and 17% and for high count density images they are 0%, 2.96%, and 18.9% respectively for best, typical, and worst case conditions. This means that in all cases we have diagnostic loss especially for typical and worst case conditions because of compression, lesion size, and other sources of variations (counting statistics, radiation dose, or acquisition time). Therefore the loss due to compression is comparable with the characteristics of the depicted object and

the modality of imaging.

We claim that the maximum compression rate can be taken as the one where the resulting diagnostic loss is equivalent to other sources of variation and after which the loss function changes slope.

All in all, this study strictly specified that a standard may be needed to determine the maximum permissible loss for given lesion and contrasts since the ultimate goal is improved quality and efficiency of patient care worldwide through improved exchange of health and image data information and improved access in remote areas.

A limitation of the present work is that model observer performance is evaluated for a task in which the signal is known to the observer and has a fixed size and shape (signal known exactly). However, in clinical practice, the lesions vary in size and shape from patient image to patient image. Furthermore, the background is known to the observer (background known exactly) in this study but the background should also vary. From the clinical point of view, the physician does not know a priori the size and shape of the lesion and the background (signal and background known statistically). It is unknown whether model observer evaluation based on a fixed signal size and shape will generalize to the more clinically realistic signal known statistically tasks. Future work is developing this study for model observers with more complex tasks (i.e. non-homogenous background, varying signal size, shape, and location) and investigating relationship between these two tasks.

APPENDIX A. OUTPUT FILES OF SIMULATION

A.1 OUTPUT FILE OF BREAST SIMULATION

```
---------- SIMIND  Monte Carlo Program v4.4 ----------

INPUT FILE...bestb34.smc  COVER.......al.cr3       SOURCE FILE..smap.fso
OUTPUT FILE..bestb34.res  CRYSTAL.....nai.cr3      SOURCE MAP...
PHANTOM (S)..h2o.cr3      BACK-SCATT...lucite.cr3  DENSITY MAP..
PHANTOM (B)..h2o.cr3                               SCORE FILE...

------------------------------ FLAGS ------------------------------
Photon Energy            140.00   Matrix     Photons/Proj      10000000.
Source  Type        Vert Cylinder  Spectra    Activity             929.44
Phantom Type        Vert Cylinder  si-leap    Detector Radius      20.000
Detector Width           25.000    B-Scatt    Detector Height       0.935
Upper Window Tresh      154.000    Random     Distance to Det       7.000
Lower Window Tresh      126.000    Cover      X-Shift Source        0.000
Pixel Size (I)            0.100    Phantom    Y-Shift Source        0.000
Pixel Size (J)            0.100    Resolut    Z-Shift Source        0.000
S:Half Length             3.960    Forced     P:Half Length         4.000
S:Half  Width             3.960               P:Half Width          4.000
S:Half Height             2.475               P:Half Height         2.500
Energy  Resolution       10.600               Max Scatter Ord           3
-------------------------------------------------------------------
    Batch       Events        Hits      ScattTot   Progress    Project
-------------------------------------------------------------------
GENERAL DATA
keV/channel               2.000            Compiler        Windows LF95
Photons/Bq                0.891            Starting Angle           0.000
Camera Offset X           0.000            Cover Thickness          0.100
Camera Offset Y           0.000            Backscatt Thick          3.000
Matrix Size    (I)          128            Intrinsic Res            0.380
Matrix Size    (J)          128            Acceptance Angle  0.20107E-02
Emission Type             2.000            Initial Weight    0.82813E+02
"NN" Scaling Factor           1            Energy Channels           512
Photon Exit Phantom           1

-------------------------------------------------------------------
COLLIMATOR DATA FOR CODE: New M Ljungberg
Collimator Code          si-leap           Collimator Type      Parallel
X:Hole Size               0.140            X:Distance               0.020
Y:Hole Size               0.162            Y:Distance               0.098
X:Center Shift            0.080            Penetration              1.000
Y:Center Shift            0.139            Hole Length              1.740
Focal Len/SH Angle        0.000            Coll X-section  pb.cr3
Collimator Effic      0.201E-02            Hole Shape           Hexagonal
Movement flag             0.000            X-Ray Flag                   0

-------------------------------------------------------------------
Simulation began 2009:09:14 at 01:07:55
Simulation ended 2009:09:14 at 01:12:46
Elapsed time 0 h 4 min and 51 sec
```

Figure A.1 Part 1 of output file of breast simulation

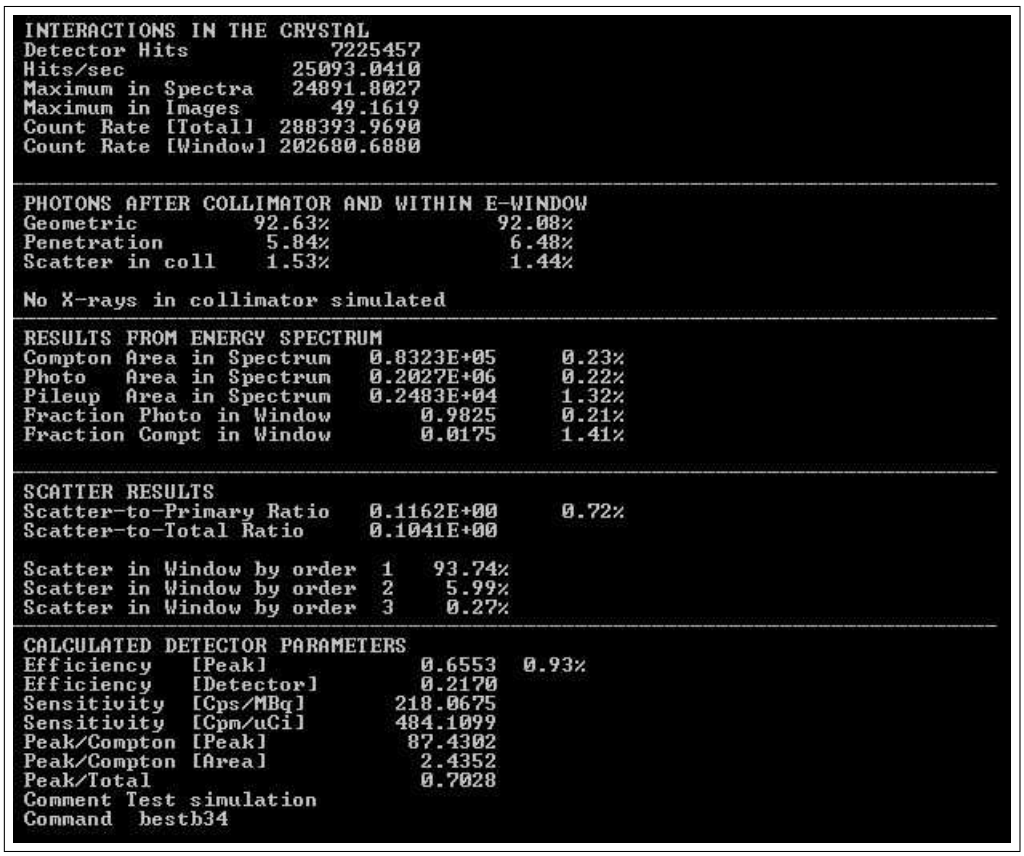

```
INTERACTIONS IN THE CRYSTAL
Detector Hits              7225457
Hits/sec                25093.0410
Maximum in Spectra      24891.8027
Maximum in Images          49.1619
Count Rate [Total]     288393.9690
Count Rate [Window]    202680.6880

-------------------------------------------------------------------------------

PHOTONS AFTER COLLIMATOR AND WITHIN E-WINDOW
Geometric          92.63%              92.08%
Penetration         5.84%               6.48%
Scatter in coll     1.53%               1.44%

No X-rays in collimator simulated
-------------------------------------------------------------------------------
RESULTS FROM ENERGY SPECTRUM
Compton Area in Spectrum    0.8323E+05      0.23%
Photo   Area in Spectrum    0.2027E+06      0.22%
Pileup  Area in Spectrum    0.2483E+04      1.32%
Fraction Photo in Window         0.9825     0.21%
Fraction Compt in Window         0.0175     1.41%

-------------------------------------------------------------------------------
SCATTER RESULTS
Scatter-to-Primary Ratio    0.1162E+00      0.72%
Scatter-to-Total Ratio      0.1041E+00

Scatter in Window by order  1    93.74%
Scatter in Window by order  2     5.99%
Scatter in Window by order  3     0.27%
-------------------------------------------------------------------------------
CALCULATED DETECTOR PARAMETERS
Efficiency   [Peak]              0.6553  0.93%
Efficiency   [Detector]          0.2170
Sensitivity  [Cps/MBq]         218.0675
Sensitivity  [Cpm/uCi]         484.1099
Peak/Compton [Peak]             87.4302
Peak/Compton [Area]              2.4352
Peak/Total                       0.7028
Comment Test simulation
Command  bestb34
```

Figure A.2 Part 2 of output file of breast simulation

A.2 OUTPUT FILE OF LESION SIMULATION

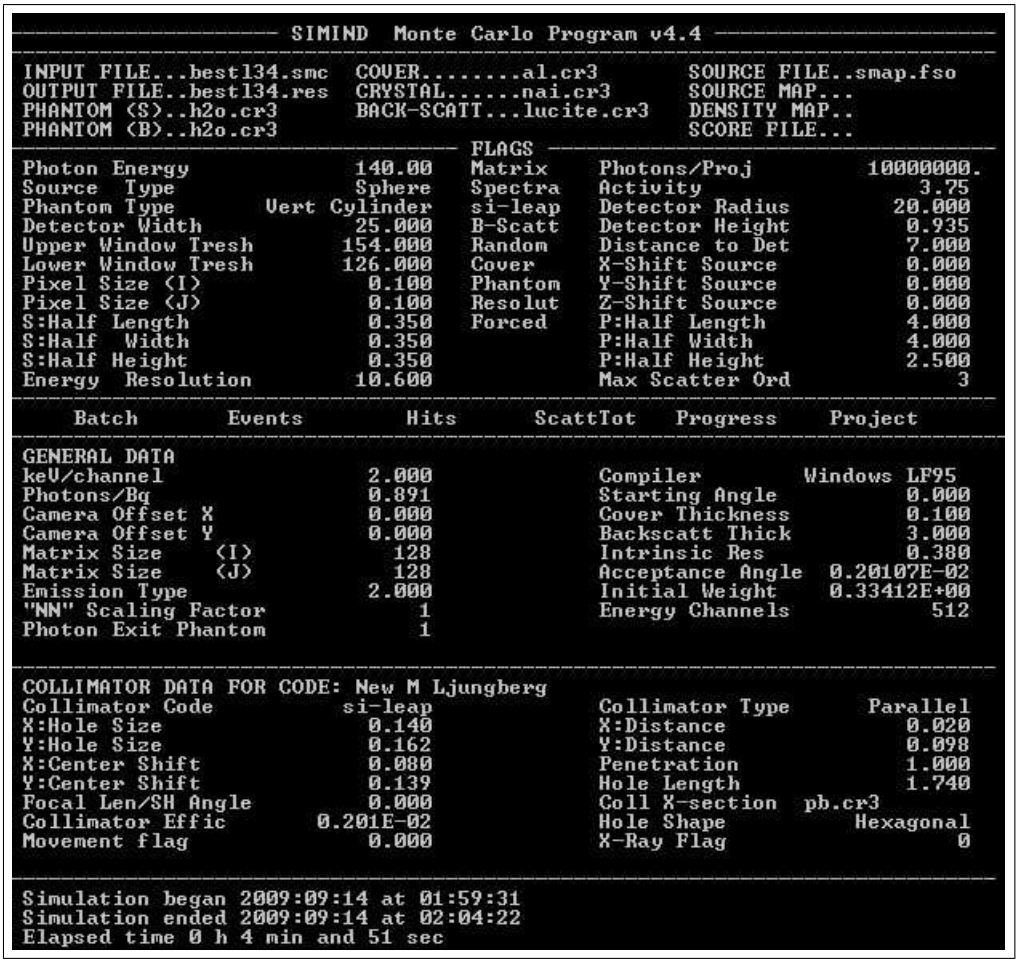

```
---------- SIMIND  Monte Carlo Program v4.4 ----------

INPUT FILE...best134.smc  COVER........al.cr3       SOURCE FILE..smap.fso
OUTPUT FILE..best134.res  CRYSTAL......nai.cr3      SOURCE MAP...
PHANTOM (S)..h2o.cr3      BACK-SCATT...lucite.cr3   DENSITY MAP..
PHANTOM (B)..h2o.cr3                                SCORE FILE...

------------------------- FLAGS -------------------------
Photon Energy             140.00   Matrix     Photons/Proj          10000000.
Source  Type              Sphere   Spectra    Activity                  3.75
Phantom Type         Vert Cylinder si-leap    Detector Radius          20.000
Detector Width            25.000   B-Scatt    Detector Height           0.935
Upper Window Tresh       154.000   Random     Distance to Det           7.000
Lower Window Tresh       126.000   Cover      X-Shift Source            0.000
Pixel Size (I)             0.100   Phantom    Y-Shift Source            0.000
Pixel Size (J)             0.100   Resolut    Z-Shift Source            0.000
S:Half Length              0.350   Forced     P:Half Length             4.000
S:Half  Width              0.350              P:Half Width              4.000
S:Half Height              0.350              P:Half Height             2.500
Energy  Resolution        10.600              Max Scatter Ord               3
-----------------------------------------------------------
    Batch       Events        Hits      ScattTot   Progress    Project
-----------------------------------------------------------
GENERAL DATA
keV/channel                2.000              Compiler        Windows LF95
Photons/Bq                 0.891              Starting Angle           0.000
Camera Offset X            0.000              Cover Thickness          0.100
Camera Offset Y            0.000              Backscatt Thick          3.000
Matrix Size    (I)           128              Intrinsic Res            0.380
Matrix Size    (J)           128              Acceptance Angle  0.20107E-02
Emission Type              2.000              Initial Weight    0.33412E+00
"NN" Scaling Factor            1              Energy Channels          512
Photon Exit Phantom            1

-----------------------------------------------------------
COLLIMATOR DATA FOR CODE: New M Ljungberg
Collimator Code           si-leap             Collimator Type      Parallel
X:Hole Size                0.140              X:Distance               0.020
Y:Hole Size                0.162              Y:Distance               0.098
X:Center Shift             0.080              Penetration              1.000
Y:Center Shift             0.139              Hole Length              1.740
Focal Len/SH Angle         0.000              Coll X-section  pb.cr3
Collimator Effic      0.201E-02               Hole Shape           Hexagonal
Movement flag              0.000              X-Ray Flag                   0

-----------------------------------------------------------
Simulation began 2009:09:14 at 01:59:31
Simulation ended 2009:09:14 at 02:04:22
Elapsed time 0 h 4 min and 51 sec
```

Figure A.3 Part 1 of output file of lesion simulation

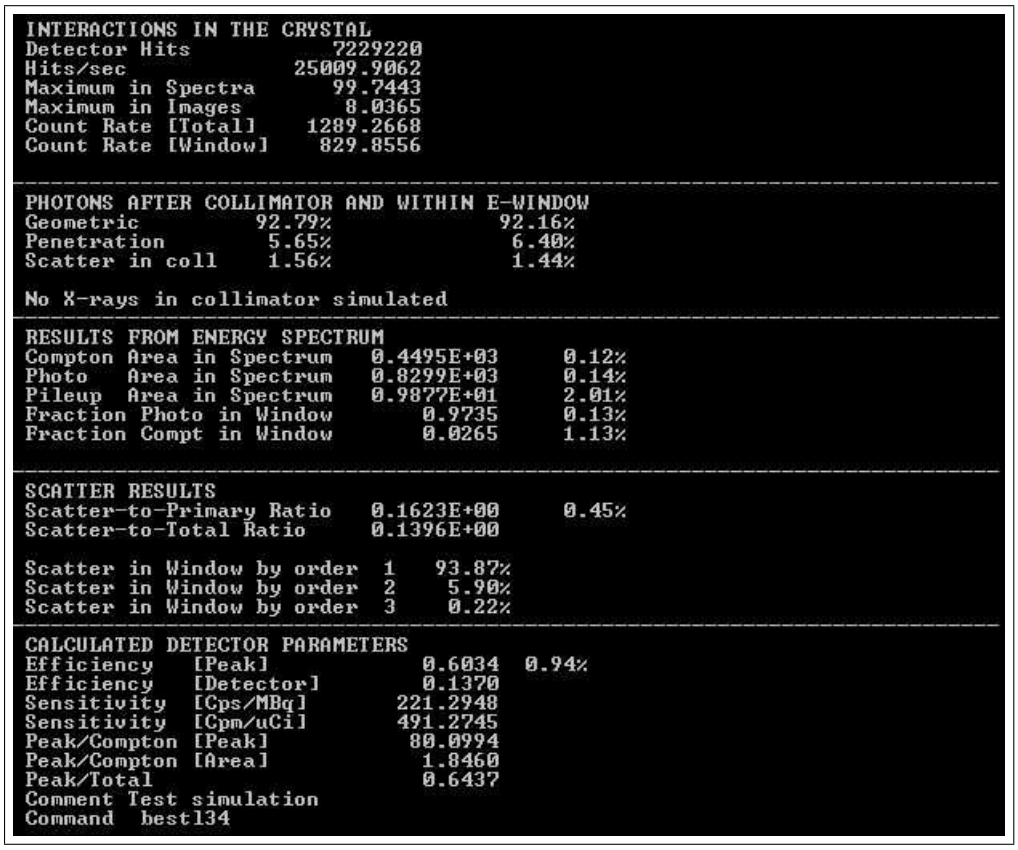

```
INTERACTIONS IN THE CRYSTAL
Detector Hits           7229220
Hits/sec              25009.9062
Maximum in Spectra       99.7443
Maximum in Images         8.0365
Count Rate [Total]     1289.2668
Count Rate [Window]     829.8556

PHOTONS AFTER COLLIMATOR AND WITHIN E-WINDOW
Geometric          92.79%              92.16%
Penetration         5.65%               6.40%
Scatter in coll     1.56%               1.44%

No X-rays in collimator simulated

RESULTS FROM ENERGY SPECTRUM
Compton Area in Spectrum    0.4495E+03      0.12%
Photo   Area in Spectrum    0.8299E+03      0.14%
Pileup  Area in Spectrum    0.9877E+01      2.01%
Fraction Photo in Window         0.9735     0.13%
Fraction Compt in Window         0.0265     1.13%

SCATTER RESULTS
Scatter-to-Primary Ratio    0.1623E+00      0.45%
Scatter-to-Total Ratio      0.1396E+00

Scatter in Window by order  1    93.87%
Scatter in Window by order  2     5.90%
Scatter in Window by order  3     0.22%

CALCULATED DETECTOR PARAMETERS
Efficiency   [Peak]              0.6034  0.94%
Efficiency   [Detector]          0.1370
Sensitivity  [Cps/MBq]         221.2948
Sensitivity  [Cpm/uCi]         491.2745
Peak/Compton [Peak]             80.0994
Peak/Compton [Area]              1.8460
Peak/Total                       0.6437
Comment Test simulation
Command  best134
```

Figure A.4 Part 2 of output file of lesion simulation

APPENDIX B. MATLAB CODES

B.1 IMAGE GENERATION

```
clear;
close all;
% Read the matrices
% Read the breast matrix from .bim file
fid=fopen('C:\simind\worstb34.BIM');
[BB]=fread(fid,[128,128],'single');
status = fclose(fid);
% Read the lesion matrix from .bim file
 fid=fopen('C:\simind\worstl34.BIM');
 [LL]=fread(fid,[128,128],'single');
 status = fclose(fid);

 % Correction constant for 1 sec to 10 min duration scaling
 cons = 600;
 [Bd] = double(cons*BB);
 [Ld] = double(cons*LL);

 % Addition of poisson noise and resultant image creation
 BackgroundwithNoise = imnoise(uint16(Bd),'poisson');
 RRwithNoise = (BackgroundwithNoise+uint16(Ld));
 %change the image with lesion to the TIFF format..
 I2 = mat2gray(RRwithNoise);
 imwrite(I2,'double.tif');
 I3 = im2uint8(I2);
 imwrite(I3,'uint8.tif');
 %change the background image to the TIFF format..
 B2 = mat2gray(BackgroundwithNoise);
 imwrite(B2,'doublebackg.tif');
 B3 = im2uint8(B2);
 imwrite(B3,'uint8backg.tif');
 figure, imshow(RRwithNoise, [])
```

Figure B.1 Matlab codes of image production

B.2 INPUT DATA OF OBSERVER MODEL

```
%%The generated lesion present and lesion absent images are converted to
%200 column vector images.

%%100 column vector images include lesion present images test(i,j,1), and
%the others includes lesion absent images test(i,j,2).

%%The following program is written for 34th original images.
%These written program is repeated for all 100 lesion present and lesion
%absent image pairs for original and various compressed bit rates images
%then the datas, test(i,j,1) is produced for lesion present image groups
%and test(i,j,2) is produced for lesion absent image groups. After that
%CHO model observer is applied to each test datas.

T1=imread('uint8.tif');
T2=T1';
T3=T2(:);
BN1=imread('uint8backg.tif');
BN2=BN1';
BN3=BN2(:);
for i=1:16384;
for j=1;
lesion(i,j+33)=T3(i,j);
end
end
for i=1:16384;
for j=1;
background(i,j+33)=BN3(i,j);
end
end
```

Figure B.2 Matlab codes of producing input data

B.3 LAGUERRE-GAUSS FUNCTION

```
function val = Laguerre2D(dim,j,a,r);
%
%  img = Laguerre2D(dim,j,a,[r]);
%
%  Generate a Laguerre-Gauss function of order j, with width parameter a.
%
%  Laguerre-Gauss functions are used to approximate the  Hotelling observer.
%
%  dim = size of resultant image
%  j   = order of LG functions
%  a   = width parameter of LG functions
%  r   = (optional) matrix defining coordinate system.  This must
%        match the size specified by dim
if (length(dim) == 1)
  dim = [dim dim];
end

if (nargin == 3)
  [X,Y] = meshgrid((1:dim(2))-(dim(2)+1)/2,(1:dim(1))-(dim(1)+1)/2);
  r = sqrt(X.^2 + Y.^2);
end
val = (1/sqrt(2*pi))*2*sqrt(pi)/a * exp(-(pi*r.^2)/(a^2)).*Laguerre1D(j,2*pi*r.^2/(a^2));

function val = Laguerre1D(j,x)
% val = Laguerre1D(j,x)
% Compute the 1-D Laguerre-Gauss function of order j at values defined by x
val = zeros(size(x));
for jp = 0:j,
  val = val + ((-1)^jp) * (prod(1:j)/((prod(1:jp)*prod(1:(j-jp)))))*...
      (x.^jp)/(prod(1:jp));
end
```

Figure B.3 Matlab codes of Laguerre-Gauss Function

B.4 TEMPLATES

```
function v = ApplyTemplates(u,g)
%
% v = ApplyTemplates(u,g)
%
% Apply the templates u to the images g.
%
% Inputs:
%    u  - [NPixels X NTemplates] Contains NTemplates templates that are
%         to be applied to the images g.
%    g  - [NPixels X NImages] The images
%
% Outputs:
%    v  - [NTemplates X NImages] the template outputs for each image.
%

[NP,NT]  = size(u);
[NP1,NI] = size(g);

if (NP1 ~= NP)
  disp('Numbers of pixels do not match.');
  return
end

v = u'*g;
```

Figure B.4 Matlab codes of Templates

B.5 CHANNELIZED HOTELLING OBSERVER

```
function [tS,tN] = CHotelling(IS,IN,Temps)
%
% [tS,tN] = CHotelling(IS,IN,Temps)
%
% Compute the channelized Hotelling observer outputs for
% the lesion present given by IS, the lesion absent images given by
% IN, and the templates given by Temps.
%
% Inputs:
%       IS, IN -- [NPixels X NImages] The images (in vector format)
%       Temps  -- [NPixels X NTemplates] The templates
%
% Outputs: tS,tN -- [NImages X 1] -- the decision variable outputs
%                   can use dprime on this output.

% Compute channel outputs
vS = ApplyTemplates(Temps,IS);
vN = ApplyTemplates(Temps,IN);

% compute mean difference image -- signal
sbar = mean(IS')-mean(IN');

% Intra-class scatter matrix
S = .5*cov(vN') + .5*cov(vS');

% channel template
wCh = inv(S) * Temps' * sbar';

% apply the channel template to produce outputs
tS = ApplyTemplates(wCh,vS);
tN = ApplyTemplates(wCh,vN);
```

Figure B.5 Matlab codes of Channelized Hotelling Observer

B.6 CALCULATION OF AUC

```
function [dp] = dprime(Sout,Nout)
%
% dp = dprime(Sout,Nous)
%
% Compute the d' (SNR) for the decision variable data given by Sout,
% and Nout (the lesion present images and
%lesion absent images outputs, respectively)
%

dp = sqrt( ((mean(Sout) - mean(Nout)).^2) / (.5*var(Sout) + .5*var(Nout)));

function Az = AzFromDP(dp)
%
% Az = AzFromDP(dp)
%
% Compute the Az from the dprime value specified by dp.  This assumes a
% binormal model.
%

Az = .5+.5*erf(dp/2);
```

Figure B.6 Matlab codes of Calculating AUC

B.7 RUNNING EXPERIMENT

```
echo on;

%Run experiment and loading of data
load 'data.mat'
n = test(:,:,2);

% n is the lesion absent images
% display of first four lesion absent images
echo off;
for i = 1:4,
  subplot(2,2,i),imagesc(reshape(n(:,i),128,128));colormap(gray);
end
echo on;

% press <return> to continue
pause;

% s is lesion present images
% loading of data
load 'data.mat'
s = test(:,:,1);

% s = lesion + background
% and display first four lesion present images
echo off;
for i = 1:4,
  subplot(2,2,i),imagesc(reshape(s(:,i),128,128));colormap(gray);
end
echo on;

% press <return> to continue
pause;
```

Figure B.7 Part 1 of Running Experiment

```
% We are going to use the Laguerre-Gauss templates for our observer.

U0 = Laguerre2D(128,0,9);
U1 = Laguerre2D(128,1,9);
U2 = Laguerre2D(128,2,9);
U3 = Laguerre2D(128,3,9);
U4 = Laguerre2D(128,4,9);

% and display the five Laguerre-Gauss templates
echo off;
subplot(2,3,1),imagesc(U0);colormap(gray);
subplot(2,3,2),imagesc(U1);colormap(gray);
subplot(2,3,3),imagesc(U2);colormap(gray);
subplot(2,3,4),imagesc(U3);colormap(gray);
subplot(2,3,5),imagesc(U4);colormap(gray);
echo on;

% press <return> to continue
pause;

% now generate the template matrix
U = [U0(:) U1(:) U2(:) U3(:) U4(:)];

% finally, compute the channelized Hotelling outputs
[tS,tN]=CHotelling(s,n,U);

% The tS, and tN are decision variable outputs which we can
% perform ROC analysis on.
[dp] = dprime(tS,tN)

% Compute the Az from the dprime value specified by dp.
Az = AzFromDP(dp)
```

Figure B.8 Part 2 of Running Experiment

REFERENCES

1. Bombardieri, E., C. F. M. L., and M. Greco, "Nuclear medicine techniques for the study of breast cancer," *Eur J Nucl Med*, Vol. 24, no. 7, pp. 809–824, 1997.

2. Mettler, F. A., and M. J. Guiberteau, *Essentials of Nuclear Medicine Imaging*, 4th ed., 1998.

3. Zaidi, H., "Relevance of accurate monte carlo modeling in nuclear medical imaging," *Med Phys*, Vol. 26, no. 4, pp. 574–608, 1999.

4. Kojima, A., M. M. T. M., and S. Uehara, "Effect of energy resolution on scatter fraction in scintigraphic imaging: Monte carlo study„" *Med Phys*, Vol. 20, no. 4, pp. 1107–1113, 1993.

5. Zaidi, H., *Quantitative Analysis in Nuclear Medicine Imaging*, New York, NY 10013, USA: Springer Science+Business Media, Inc., 2006.

6. "The simind monte carlo program," tech. rep., http://www.radfys.lu.se/simind/.

7. Paul W. Jones, M. R., "Jpeg compression in medical imaging," in *Handbook of Medical Imaging* (Youngmin Kim, S. C. H., ed.), Vol. 3, ch. 5, pp. 221–271, Washington, USA: SPIE Press, 2000.

8. Schomer, D. F., "Introduction to wavelet-based compression of medical images," *RadioGraphics*, Vol. 18, pp. 469–481, 1998.

9. Przelaskowski, A., "Irreversible medical image compression: Conditions of acceptability," *TASK QUARTERLY*, Vol. 8, no. 2, pp. 303–316, 2004.

10. tech. rep., Food and Drug Administration, Center for Devices and Radiological Health, Guidance for the Submission of Premarket Notifications for Medical Image Management Devices„ http://www.fda.gov/cdrh/ode/guidance/416.pdf, 2000.

11. Ciatto, S., T. M. R. D., and P. Bravetti, "Nonpalpable breast lesions: stereotaxic fine-needle aspiration cytology," *Radiology*, Vol. 173, no. 1, pp. 57–59, 1989.

12. Fajardo, L. L., D. J. R. W. J. L., and D. C. Trego, "Mammography-guided stereotactic fine-needle aspiration cytology of nonpalpable breast lesions: prospective comparison with surgical biopsy results," *AJR Am J Roentgenol*, Vol. 155, no. 5, pp. 977–981, 1990.

13. Schreer, I., and J. Frischbier, "Breast cancer screening projects: results," in *Radiological diagnosis of breast diseases* (Friedrich, M., S. E. A., ed.), pp. 333–346, Berlin Heidelberg New York: Springer, 1997.

14. Tulusan, A., "Mammographic-pathological correlations," in *Radiological diagnosis of breast diseases* (Friedrich, M., S. E. A., ed.), pp. 13–32, Berlin Heidelberg New York: Springer, 1997.

15. Teubner, J., "Echomammography: technique and results," in *Radiological diagnosis of breast diseases* (Friedrich, M., S. E. A., ed.), pp. 181–220, Berlin Heidelberg New York: Springer, 1997.

16. Bauer, M., T. P., and R. Schulz-Wendtland, "Fine-needle aspiration and core biopsy," in *Radiological diagnosis of breast diseases* (Friedrich, M., S. E. A., ed.), pp. 291–298, Berlin Heidelberg New York: Springer, 1997.

17. Oestmann, J., "Digital mammography," in *Radiological diagnosis of breast diseases* (Friedrich, M., S. E. A., ed.), pp. 65–74, Berlin Heidelberg New York: Springer, 1997.

18. Heywang-Kobrunner, S. H., and R. Beck, "Clinical application of contrast- enhanced mri," in *Contrast-enhanced MRI of the breast*, pp. 157–204, Berlin Heidelberg New York: Springer, 1996.

19. Fajardo, L. L., "Screening mammography," *Imaging Decisions MRI*, Vol. 9, no. 2, pp. 23–34, 2005.

20. Low-Beer B V A, Bell H G, M. H. J., "Measurement of radioactive phosphorous in breast tumours in situ: a possible diagnostic procedure.," *Radiology*, Vol. 46, pp. 492–493, 1946.

21. Berg J. R., Kalisher L., O. J. D., "Technetium-99m-disphosphonate concentration in primary breast cancer.," *Radiology*, Vol. 109, pp. 393–394, 1973.

22. Hisada K, Tonamin N, M. T., "Clinical evaluation of tumour imaging with thallium-201 chloride," *Radiology*, Vol. 129, pp. 497–500, 1978.

23. Goldenberg D M, DeLand F, K. E., "Use of radiolabeled antibodies to carcinoembryonic antigen for the detection and localization of diverse cancers by external photoscanning.," *N Engl J Med*, Vol. 298, pp. 1384–1388, 1978.

24. Muller S T, Guth-Tougelids B, C. G. H., "Imaging ofmalignant tumours with tc-99m-mibi spect," *Eur J Nucl Med*, Vol. 28, p. 562, 1987.

25. Kubota K, Matsuzwana T, A. A., "Imaging of breast cancer with (f-18) fluorodeoxyglucose and positron emission tomography," *J Comput Assist Tomogr*, Vol. 13, pp. 1097–1098, 1989.

26. Aktolun C, Bayhan H, K. M., "Clinical experienca with tc-99m mibi imaging in patients with malignant tumors: preliminary results and comparison with tl-201," *Clin Nucl Med*, Vol. 14, pp. 333–340, 1989.

27. Rambaldi P F, Mansi L, P. E. D.-G. F. D.-V. E., "Breast cancer detection with tc-99m tetrofosmin," *Clin Nucl Med*, Vol. 20, pp. 703–705, 1995.

28. V.W. Lee, E.J. Sax, D. M., "A complementary role for thallium-201 scintigraphy with mammography in the diagnosis of breast cancer," *Journal of Nuclear Medicine*, Vol. 34, pp. 2095–2100, 1993.

29. I. Khalkhali, I. Mena, E. J., "Prone scintimammography in patients with suspicion of carcinoma of the breast," *Journal of the American College of Surgeons*, Vol. 178, pp. 491–497, 1994.

30. A. Waxman, N. N., and G. Ashok, "Sensitivity and specificity of tc-99m methoxy isobutal isonitrile (mibi) in the evaluation of primary carcinoma of the breast: comparison of palpable and nonpalpable lesions with mammography," *Journal of Nuclear Medicine*, Vol. 35, p. 22, 1994.

31. D. Piwnica-Worms, M.L. Chiu, M. B., "Functional imaging of multidrug-resistant p-glycoprotein with an organotechnetium complex," *Cancer Research*, Vol. 53, pp. 977–984, 1993.

32. J. Villanueva-Meyer, M.H.L. Leonard Jr., E. B., "Mammoscintigraphy with technetium-99m-sestamibi in suspected breast cancer," *Journal of Nuclear Medicine*, Vol. 36, pp. 926–930, 1996.

33. D. Piwnica-Worms, J. K., and M. Chiu, "Uptake and retention of hexakis (2-methoxyisobutyl isonitrile) technetium(i) in cultured chick myocardial cells," *Circulation*, Vol. 82, pp. 1826–1838, 1990.

34. P.A. Carvalho, M.L. Chiu, J. K., "Subcellular distribution and analysis of tc-99m mibi in isolated perfused rat hearts," *Journal of Nuclear Medicine*, Vol. 33, pp. 1516–1521, 1992.

35. I. Khalkhali, J. Cutrone, I. M., "Technetium-99m-sestamibi scintimammography of breast lesions: clinical and pathological follow-up," *Journal of Nuclear Medicine,*, Vol. 36, pp. 1784–1789, 1996.

36. R. Taillefer, I. Khalkhali, A. W., *Radionuclide Imaging of the Breast*, New York: Marcel Dekker, 1998.

37. R. Taillefer, A. Robidoux, S. T., "Detection of axillary lymph node involvement with tc-99m-sestamibi imaging in breast cancer detection," *Journal of Nuclear Medicine,*, Vol. 37, p. 75, 1996.

38. I. Khalkhali, J. Villanueva-Meyer, S. E., "Impact of breast density on the diagnostic accuracy of tc-99m sestamibi breast imaging in the detection of breast cancer," *Journal of Nuclear Medicine,*, Vol. 37, p. 74, 1996.

39. H. Palmedo, A. Schomburg, F. G., "Technetium-99m scintimammography for suspicious breast lesions," *Journal of Nuclear Medicine,*, Vol. 37, pp. 626–630, 1996.

40. I. Khalkhali, J. Villanueva-Meyer, S. E., "Diagnostic accuracy of tc-99m sestamibi breast imaging in breast cancer detection," *Journal of Nuclear Medicine*, Vol. 36, pp. 718–724, 1995.

41. B. Fisher, M. Bauer, D. W., "Relation of number of positive axillary nodes to the prognosis of patients with primary breast cancer," *Cancer*, Vol. 52, pp. 1551–1557, 1983.

42. Bombardieri, E., C. A. B. P. R. A. B.-D. J. B. J. F. C. L. M. R. M. L. M. S. N. R., "Breast scintigraphy: procedure guidelines for tumour imaging," *Eur J Nucl Med Mol Imaging*, Vol. 23, pp. 609–611, 2003.

43. Jonasson, T., "Revival of a gamma camera," Master's thesis, Nuclear Physics Group Physics Department Royal Institute of Technology, 2003.

44. Sprawls, P., *Physical Principles of Medical Imaging*, Rockville: Aspen Publications, 1987.

45. "Introduction to monte carlo methods, by the computational science education project (csep)," tech. rep., http://www.cse.psu.edu/ raghavan/cse557/MC.pdf.

46. Zaidi, H., "Monte carlo techniques in diagnostic and therapeutic nuclear medicine," *Standards and Codes of Practice in Medical Radiation Dosimetry, ISBN 92-0-111403-6*, Vol. 2, pp. 29–44, 2002.

47. Ljungberg, M., S. S., and M. A. King, "Monte carlo calculation in nuclear medicine: Applications in diagnostic imaging," *IOP Publishing*, pp. 145–163, 1998.

48. Dewaraja, Y. K., L. M., and K. F. Koral, "Characterization of scatter and penetration using monte carlo simulation in 131-i imaging," *J.Nucl.Med*, Vol. 41, pp. 123–130, 2000.

49. Hahn, L. J., J. R. J. G. G. T.-F. C. E. M. S. H. G. K. L., and R. E. Coleman, "Noise characteristics for cone beam collimators: a comparison with parallel hole collimator," *Phys. Med. Biol.*, Vol. 33, pp. 541–555, 1988.

50. Dye, R. E. A., "Simulation of clinical scitingrams for nuclear medicine imaging devices," *Phys. Med. Biol.*, Vol. 33, pp. 1329–1334, 1988.

51. Gantet, P., E. J. P. D. B., and R. Guiraud, "A simulation method for studying scintillation camera collimators," *Phys. Med. Biol.*, Vol. 35, no. 5, pp. 659–669, 1990.

52. Rosenthal, M. S., C. J. H. W. M. S. C. T. B. M., and M. Yester, "Quantitative spect imaging: a review and recommendations by the focus committee of the society of nuclear medicine computer and instrumentation council," *J Nucl Med.*, Vol. 36, no. 8, pp. 1489–1513, 1995.

53. Zaidi, H., "Quantitative spect: Recent developments in detector response, attenuation and scatter correction techniques," *Phys. Medica*, Vol. 12, pp. 101–117, 1996.

54. Floyd, C. E., J. R. J., and R. E. Coleman, "Scatter detection in spect imaging: dependence on source depth, energy, and energy window," *Phys Med Biol*, Vol. 33, no. 9, pp. 1075–1081, 1998.

55. Lowry, C. A., and M. J. Cooper, "The problem of compton scattering in emission tomography: a measurement of its spatial distribution," *Phys Med Biol,*, Vol. 32, no. 9, pp. 1181–1191, 1987.

56. Andreo, P., "Monte carlo techniques in medical radiation physics," *Phys Med Biol*, Vol. 36, no. 7, pp. 861–920, 1991.

57. Berger, M. J., "Mird pamphlet 2: energy deposition in water by photons from point isotropic sources," *J. Nucl. Med.*, Vol. 9, pp. 15–25, 1968.

58. Berger, M. J., "Mird pamphlet 7: distribution of absorbed doses around point sources of electrons and beta particles in water and other media," *J. Nucl. Med.*, Vol. 12, pp. 5–23, 1971.

59. Wang, H., J. R. J., and R. E. Coleman, "Solid geometry-based object model for monte carlo simulated emission and transmission tomographic imaging systems," *IEEE Trans. Med. Imaging*, Vol. 11, pp. 361–372, 1992.

60. Wang, H., J. R. J., and R. E. Coleman, "A new composite model of objects for monte carlo simulation of radiological imaging," *Phys Med Biol*, Vol. 38, no. 9, pp. 1235–1262, 1993.

61. Nelson W. R., Hirayama, H., and D. W. O. Rogers, "The egs4 code system," report slac-256, Stanford Linear Accelerator Center, 1985.

62. Kawrakow I., Mainegra-Hing, E., and D. W. O. Rogers, "The egsnrc code system: Monte carlo simulation of electron and photon transport ionizing radiation standards," tech. rep., National Research Council of Canada, 2003.

63. Halbleib J. A., Kensek, R. P. V. G. D., "Its: The integrated tiger series of electron/photon transport codes - version 3.0.," *IEEE Trans Nucl Sci*, Vol. 39, pp. 1025–1030, 1992.

64. F., B. J., "Mcnp - a general monte carlo n-particle transport code. version 4c," nm; report la-13709-m, Los Alamos National Laboratory, 2000.

65. Hendricks J. S., McKinney, G. W. W. L. S., "Mcnpx, version 2.5.e.," nm; report la-ur-04-0569, Los Alamos National Laboratory, 2004.

66. Brun R., Bruyant, F. M. M., "Geant detector description and simulation tool," report dd/ee/84-1, CERN, 1994.

67. Sempau J., Acosta, E. B. J., "An algorithm for monte carlo simulation of the coupled electron-photon transport," *Nucl Instr Meth B*, Vol. 132, pp. 377–390, 1997.

68. Fasso A., Ferrari, A., and P. R. Sala, "Electron-photon transport in fluka: status," in *Proceedings of the Monte Carlo 2000 Conference* (A Kling, Barao, F. N. M. T. L. V. P., ed.), pp. 159–164, Berlin: Springer-Verlag, 2001.

69. M., D. M., and G. F. Knoll, "Results of scattering in radioisotope imaging.," *IEEE Trans Nucl Sci*, Vol. 20, pp. 266–272, 1973.

70. Beck J. W., Jaszczak, R. J. C. R. E., "Analyzing spect including scatter and attenuation using sophisticated monte carlo modeling methods.," *IEEE Trans Nucl Sci*, Vol. 29, 1982.

71. Floyd C. E., Jaszczak, R. J. G. K. L., "Inverse monte carlo as a unified reconstruction algorithm for ect," *J Nucl Med*, Vol. 27, pp. 1577–1585, 1986.

72. A., K. N., and J. R. Lupton, "Pet detector ring aperture function calculations using monte carlo techniques," *IEEE Trans Nucl Sci*, Vol. 30, pp. 676–680, 1983.

73. R., L. L., and N. A. Keller, "Performance study of single-slice positron emission tomography scanners by monte carlo techniques," *IEEE Trans Med Imaging*, Vol. 2, pp. 154–168, 1983.

74. Lewellen T., Harrison, R. L., and S. Vannoy, "The simset program," in *Monte Carlo calculations in nuclear medicine: Applications in diagnostic imaging* (M Ljungberg, S.-E. S., and M. A. King, eds.), pp. 77–92, Bristol: Institute of Physics Publishing, 1998.

75. M., L., "The simind monte carlo program," in *Monte Carlo calculations in nuclear medicine: Applications in diagnostic imaging* (M Ljungberg, S.-E. S., and M. A. King, eds.), pp. 145–163, Bristol: Institute of Physics Publishing, 1998.

76. F., S. M., "Vectorized monte carlo code for modelling photon transport in nuclear medicine," in *Monte Carlo calculations in nuclear medicine: Applications in diagnostic imaging* (M Ljungberg, S.-E. S., and M. A. King, eds.), pp. 93–109, Bristol: Institute of Physics Publishing, 1998.

77. C., T., and Y. Picard, "Petsim: Monte carlo simulation of positron imaging systems," in *Monte Carlo calculations in nuclear medicine: Applications in diagnostic imaging* (M Ljungberg, S.-E. S., and M. A. King, eds.), pp. 233–248, Bristol: Institute of Physics Publishing, 1998.

78. Zaidi H., Scheurer, A. H., and C. Morel, "An object-oriented monte carlo simulator for 3d cylindrical positron tomographs," *Comput Methods Programs Biomed*, Vol. 58, pp. 133–145, 1999.

79. Reilhac A., Lartizien, C. C. N., "Pet-sorteo: a monte carlo-based simulator with high count rate capabilities," *IEEE Trans Nucl Sci*, Vol. 51, pp. 46–52, 2004.

80. Edward Oczeretko, Waldemar Rakowski, D. J., "Wavelet compression of nuclear medicine," *Nuclear Medicine Review 2000*, Vol. 3, no. 2, pp. 153–156, 2000.

81. Urban, S. J., "Review of standards for electronic imaging for facsimile systems," *J. Elec. Imag.*, Vol. 1, no. 1, pp. 5–21, 1992.

82. Lux, P., "Redundancy reduction in radiographic pictures," *Opt. Acta*, Vol. 24, no. 4, pp. 349–365, 1977.

83. Lo, S. C., and H. K. Huang, "Radiologic image compression: Full-frame bit allocation technique," *Radiology*, Vol. 155, pp. 811–817, 1985.

84. David H. Foes, Edward Mukab, R. M. S. B. J. E. M. J. F. D. A. C. L. H. K. K., and S. Younga, "Jpeg 2000 compression of medical imagery," *SPIE*, Vol. 3980, pp. 85–96, 2000.

85. M. Antonini, M. Barlaud, P. M., and I. Daubechies, "Image coding using wavelet transform," *IEEE Trans. Image Proc.*, Vol. 1-2, pp. 205–219, 1992.

86. "Vcdemo compression modules," tech. rep., http://ict.ewi.tudelft.nl/.

87. H Santalla, G. M., and V. Ballarin, "Effects on mr images compression in tissue classification quality," *Journal of Physics: Conference Series 90*, pp. 1–7, 2007.

88. Kanukolanu, U., "Image compression using the wavelet transforms in matlab," Master's thesis, Texas A&M University-Kingsville, 2004.

89. Saffor, R., and Ng, "A comparative study of image compression between jpeg and wavelet," *Malaysian Journal of Computer Science*, Vol. 14, pp. 39–45, june 2001.

90. Tan, C. L., "Still image compression using wavelet transform," Master's thesis, School of Information Technology and Electrical Engineering The University of Queensland, 2001.

91. Ullman, G., "Quantifying image quality in diagnostic radiology using simulation of the imaging system and model observers," Master's thesis, Linköping University, Sweden, 2008.

92. Smith W, B. H., "Hotelling trace criterion as a figure of merit for the optimization of imaging systems," *J Opt Soc Am A.*, Vol. 3, pp. 717–725, 1986.

93. Fiete R, Barrett H, S. W. M. K., "The hotelling trace criterion and its correlation with human observer performance," *J Opt Soc Am A.*, Vol. 4, pp. 945–953, 1987.

94. Myers K, Rolland J, B. H. W. R., "Aperture optimization for emission imaging: effect of a spatially varying background.," *J Opt Soc Am A.*, Vol. 7, pp. 1279–1293, 1990.

95. Barrett H, Abbey C, G. B. E. M., "Stabilized estimates of hotelling observer detection performance in patient-structured noise.," *Proc SPIE.*, Vol. 3340, pp. 27–43, 1998.

96. B., G., *Signal Detection in Lumpy Backgrounds*. PhD thesis, University of Arizona, Tucson, AZ, 2001.

97. ho Hua, C., *Compton Imaging System Development and Performance Assessment*. PhD thesis, The University of Michigan, 2000.

98. John D. Sain, P., and P. Harrison H. Barrett, "Performance evaluation of a modular gamma camera using a detectability index," *THE JOURNAL OF NUCLEAR MEDICINE*, Vol. 44, no. 1, pp. 58–66, 2003.

99. Balta, S., "Robust design of a breast scintigraphy collimator using monte carlo simulations and response surface methodology," Master's thesis, Boğaziçi University, 2007.

100. Maublant, J., d. L. M. M. D. C. A. C. S. F. V. B. G. L. K. P. D. J., and A. Veyre, "Technetium-99m-sestamibi uptake in breast tumor and associated lymph nodes," *THE JOURNAL OF NUCLEAR MEDICINE*, Vol. 37, no. 6, pp. 922–925, 1996.